DISSERTATION

submitted to the

Combined Faculties of the Natural Sciences and Mathematics

of the Ruperto-Carola-University of Heidelberg, Germany

for the degree of

Doctor fo Natural Sciences

Put forward by

M.Sc. Qingzhi An

Born in Dalian, China

Oral examination: 10.12.2020

Physics of Interfaces in $MAPbI_3$ Perovskite Solar Cells

Referees:
Prof. Dr. Yana Vaynzof
Prof. Dr. Karl Leo

Physics of Interfaces in $MAPbI_3$ Perovskite Solar Cells

Interfaces in perovskite solar cells, such as interfaces between adjacent layers or at grain boundaries, play an important role in determining the performance of photovoltaic devices. This thesis describes investigations of the physical properties of several such interfaces in order to elucidate their influence on the photovoltaic devices and further utilize this knowledge to improve the device performance. First, we investigate the interface between a perovskite active layer and a ZnO electron transport layer. We demonstrate that this interface strongly influences the microstructure of polycrystalline perovskite. Using a combination of doping and modification by a self-assembled monolayer, we optimize both the bulk and surface properties of the ZnO layer, leading to a superior perovskite layer microstructure and a doubling of the photovoltaic performance. Next, we investigate the interface between an organic electron transport layer and the metal cathode. We modify this interface by inserting a series of newly synthesized π-extended phosphoniumfluorene electrolytes and demonstrate that such modification significantly increases the built-in potential of the device by compensating for the non-ideal energetic alignment caused by the other device layers. Consequently, the modified devices exhibit an increase in the open-circuit voltage by up to 120 mV. Finally, we systematically investigate the effects of grain boundaries on the performance of perovskite solar cells by combining the experimental characterizations and the theoretical device simulations. We show that grain boundaries contribute to the non-radiative recombination losses in perovskite solar cells and the small grains serve as recombination 'hot spots' that limit the open circuit voltage, as well as the performance of the devices.

Physik von der Grenzschichten in $MAPbI_3$ Perowskit-Solarzellen

Grenzschichten in Perowskit-Solarzellen, wie zum Beispiel an aneinander anschließenden Schichten oder an Kristallitgrenzen, sind ein wichtiger, bestimmender Faktor für die Effizienz photovoltaischer Bauteile. Diese Doktorarbeit enthält Untersuchungen der physikalischen Eigenschaften mehrerer solcher Grenzschichten, um deren Einfluss auf die Leistung von Bauteilen aufzuklären und weitergehend dieses Wissen zu nutzen, um die photovoltaische Leistung zu verbessern. Zuerst untersuchen wir die Grenzschicht zwischen einer Perowskit-Aktivschicht und einer Elektronentransportschicht aus Zinkoxid. Wir zeigen, dass diese Grenzschicht stark die Mikrostruktur des polykristallinen Perowskit beeinflusst. Durch eine Kombination aus Dotierung und Modifikation mit einer sich selbstordnenden Monomolekularenschicht, optimieren wir sowohl die Kristall- wie auch die Oberflächeneigenschaften der Zinkoxidschicht, was zu einer verbesserten Mikrostruktur der Perowskitschicht führt und die photovoltaische Effizienz verdoppelt. Als Nächstes untersuchen wir die Grenzfläche zwischen einer organischen Elektronentransportschicht und einer Metall-Kathode. Wir modifizieren diese Grenzschicht durch das Einbringen einer Reihe von neu-synthetisierten π-erweiterten Phosphoniumfluorene-Elektrolyten und demonstrieren, dass solch eine Modifikation die Diffusionsspannung der Bau-teile maßgeblich erhöht, indem die nicht ideale energetische Anpassungen von anderen Schichten im Bauteil ausgegli-chen werden. Folglich zeigen die modifizierten Bauteile einen Anstieg der Leerlaufspannung um bis zu 120mV. Zuletzt untersuchen wir systematisch den Effekt von Grenzflächen auf die Leistung von Perowskit-Solarzellen, indem wir experimentelle Charakterisierungsmethoden mit theoretischen Bauteilsimulationen kombinieren. Wir zeigen, dass Grenzschichten zu nicht-strahlenden Rekombinationsverlusten in Perowskit-Solarzellen beitragen, und dass kleine Kristallite als Rekombinations 'Hot Spots' dienen, die die Leer-laufspannung und die Effizienz der Bauteile limitiert.

Contents

Chapter 1

Introduction

With the rapid growth of global economy and population, the world energy consumption steadily rises year by year. In 2019, the world energy consumption has reached 583.9 EJ (~ 162,000 TWh) which is 1.3% higher than 2018.[1] Over 80% of the energy is supplied by fossil fuels[1] which are finite supply and are accompanied by the greenhouse gas emission. The increase in the concentration of greenhouse gases in the atmosphere leads to an ascent of global temperature causing severe global challenges, such as the melting of on-shore ice shields and the rising of sea level. These problems not only break the balance of the ecosystem, but also threaten the living conditions of human beings. Therefore, it is essential to develop clean and renewable energy sources to gradually reduce the usage of fossil fuels.

Photovoltaic devices or solar cells, which can directly generate electricity from sun light via the photovoltaic effect, represent one of the most widely used renewable energy sources. The photovoltaic industry has been in development for more than 60 years. With recent advances in the nano-material and nanotechnology fields, remarkable improvements in boosting the light to electricity power conversion efficiency of photovoltaics have been achieved. Nowadays, due to a further need of large scale, low cost, flexible and light-weight solar modules, researchers have focused on the solution based photovoltaic cells, such as dye-sensitized solar cells, organic solar cells, perovskite solar cells and quantum dot solar cells. Among these, perovskite solar cells have reached 25.5% power conversion efficiency in less than a decade (Figure 1.1), showing their great potential to compete with the commercially available silicon solar cells.

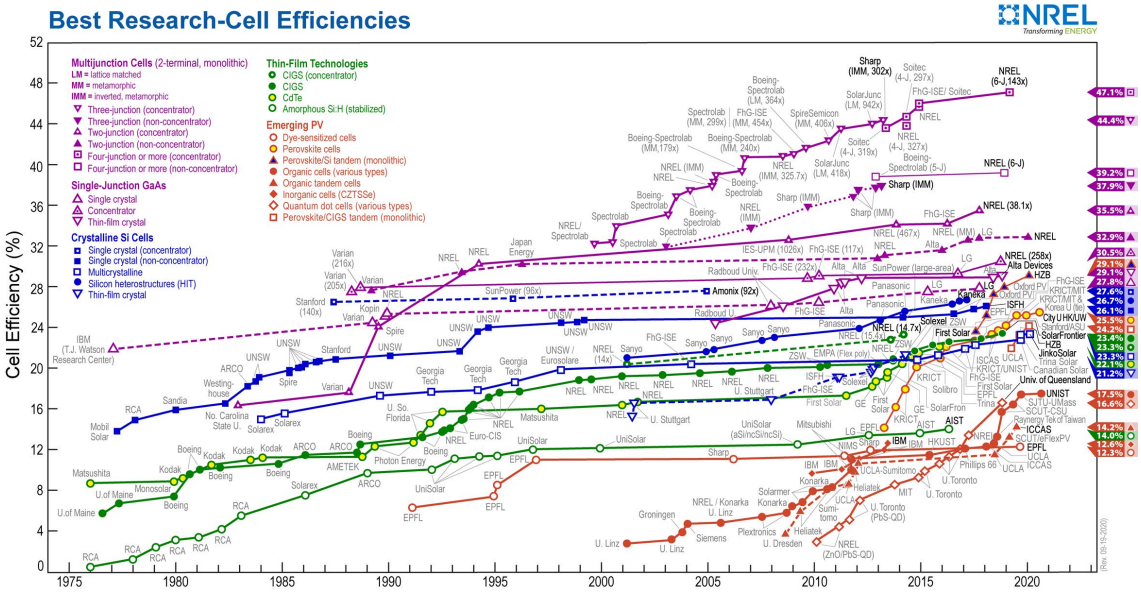

Figure 1.1: The best confirmed efficiency for research cells including all the photovoltaic technologies. Adapted from [2]

At the early stages of the perovskite solar cell research, the scientific efforts focused on the mesoporous structure, where a perovskite layer was deposited onto a mesoporous inorganic scaffold.[3, 4] Recently, due to a simpler fabrication process and a lower fabrication temperature, planar perovskite solar cells attract more research interests.[5] Together with the development of perovskite device structure, the composition of the absorber materials (perovskites) have also evolved from the simple organic-inorganic halide composition (e.g. $MAPbI_3$) to multi cation with mixed halide perovskite (e.g. $MA_{0.17}FA_{0.83}Pb(I_{0.83}Br_{0.17})_3$), pure inorganic perovskite (e.g. $CsPbI_3$) and lead free perovskite (e.g. $FASnI_3$). However, regardless of which structure or material is chosen, all perovskite solar cells exhibit interfaces such as between two adjacent layers or at the perovskite grain boundaries. These interfaces are important in determining the electronic properties, the performance and the degradation of solar cells.[6–8] In this thesis, we use the basic perovskite material $MAPbI_3$ to explore two major concepts: 1. modification of the interfaces to improve the photovoltaic performance and 2. elucidate the function of grain boundaries in perovskite solar cells. The interface between electron transport layer and

perovskite, the interface between electron transport layer and electrode as well as the 'bulk interface' (grain boundaries) are investigated. We focus on studying their influences on the photovoltaic performance of devices and utilizing a range of spectroscopic measurements to reveal the fundamental reasons for the improvements. We aim to offer an advanced understanding of the physics of interfaces in perovskite solar cells.
This thesis is organized as follows:

- In Chapter 2, a brief introduction of perovskite materials and perovskite solar cells as well as the loss mechanisms of the open-circuit voltage are discussed.
- In Chapter 3, all the experimental methods used in this thesis are described in detail, including sample and device fabrication and characterization by a broad range of spectroscopic and microscopic methods.
- In Chapter 4, we investigate the interface of electron transport layer (ZnO) and perovskite in planar standard architecture of perovskite solar cells.
- In Chapter 5, newly synthesized π-extended phosphoniumfluorene electrolytes are used as hole blocking layers to modify the interface of electron transport layer and perovskite in inverted perovskite solar cells.
- In Chapter 6, after developing a facile way to control grain size, we apply this method to fabricate devices with different grain size to investigate the role of grain boundaries in perovskite photovoltaic performance.
- In Chapter 7, the obtained results are summarized and an outlook of future work is presented.

Chapter 2

Theoretical Background

As this thesis is dedicated to investigate the effects of interfaces between two adjacent layers and 'bulk interfaces' grain boundaries in perovskite solar cells, in this chapter we present an overview of fundamental concepts in perovskite semiconductor and perovskite solar cells to offer the theoretical supports for the rest of the thesis. In the first part, we briefly introduce what is perovskite, and why metal halide perovskite can be used in photovoltaic systems, including the advantages and disadvantages of this material. Secondly, some basic descriptions about perovskite solar cells are discussed, such as device working principle, device architecture, device characterization and hysteresis. In the last part, we review the recombination processes that happen in the photovoltaic devices, especially the influence of non-radiative recombination on device performance.

2.1 Organic-Inorganic Halide Perovskites

2.1.1 Structures of Perovskites

A class of compounds which have the same type of crystal structure as $CaTiO_3$ with chemical formula as ABX_3 is named perovskite.(Figure 2.1) The select rule for the elements on A, B and X site is based on the Goldschmidt rule, where the Goldschmidt tolerance factor t should be in the range of 0.71-1 to maintain the perovskite structure. ($t = \frac{r_A+r_X}{\sqrt{2}(r_B+r_X)}$, r_i is the radius of relevant atoms)[9] Interestingly, depending on the tilting and rotation of the BX_3 polyhedra in the lattice, perovskites adapt phase transitions with accessible to different crystal structure such as cubic, tetragonal, orthorhombic, trigonal and monoclinic polymorphs.[10] Moreover,

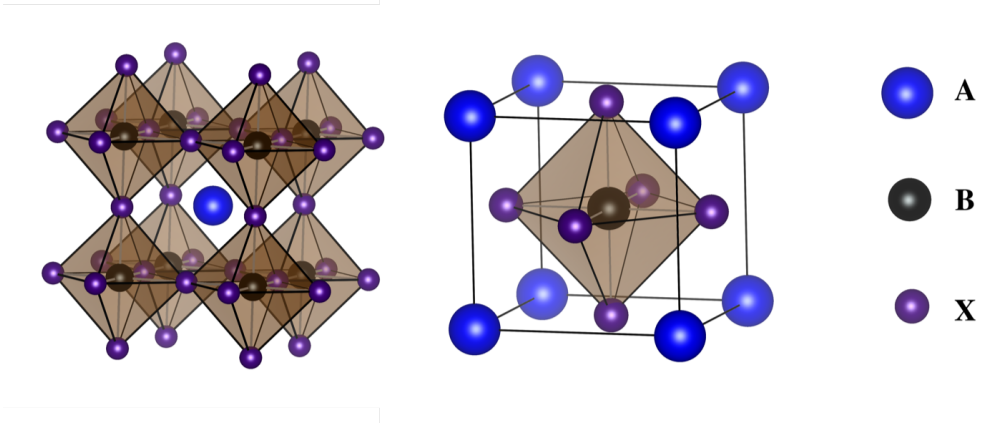

Figure 2.1: A ball-stick model for ABX_3 perovskite structure with A atom in the interstice and at the corner position.

perovskite materials can be insulators, superconductors and semiconductors.

Since 2009, organic-inorganic hybrid perovskite becomes the most breakthroughs semiconductor for optoelectronics. In this hybrid perovskite, generally A cation is cesium (Cs), methylammonium (CH_3NH_3, MA) or formamidinium ($CH(NH_2)_2$, FA), B cation is lead (Pb) or tin (Sn) and X anion is iodide (I), bromide (Br) or chloride (Cl). This kind of perovskite is ionic crystal and tends to form an orthorhombic structure ($t < 0.8$), cubic structure ($0.8 < t < 1$), and non-perovskite hexagonal structure (t > 1) However, usually more than one structure is found in one organic-inorganic hybrid perovksite, depending on the temperature and preparation methods.[11]

For example, the commonly used perovskite which is also studied in this work $MAPbI_3$ presents orthorhombic to tetragonal phase transition at 162 K and tetragonal to cubic phase transition at 327 K.[12] Although, there is a blueshift of the bandgap across tetragonal to cubic phase transition, the photovoltaic performance does not change dramatically. However, due to incomplete exciton dissociation in disordered domains, a strong decrease of performance happens when $MAPbI_3$ perovskites approach the orthorhombic phase.[13–15] On the contrary, another generally used perovskite $FAPbI_3$, only exists a yellow hexagonal non-perovskite phase with bad photovoltaic performance at room temperature due to a large radius of FA atoms. $FAPbI_3$ forms a cubic phase after annealing over 150 °C, however, the yellow phase reappears with progressing time. To stabilize the

cubic phase of $FAPbI_3$, composition engineering via cooperating smaller atoms such as Cs and MA to squeeze the tolerance factor, and additive engineering via adding additives such as $MACl$ into perovskite precursor solution have been successfully approved.[16–18]
Moreover, besides the phase transition, when A sites are occupied by too large groups such as the long-chain alkyl amine cations, a special kind of perovskite is formed with the general formula $(RNH_3)_2MA_{n-1}B_nX_{3n-1}$, where n is the number of inorganic BX_6 sheets. These perovskite exhibits similar van der Waals layered crystal structure as the conventional 2D material, and they are known as 2D (n=1) or quasi-2D (n>2) perovskite. Owning to environmental stabilities, large exciton binding energies, high quantum yields and other rich photophysics properties, 2D or quasi-2D perovskites have also received more research interests.[19–22]

2.1.2 Physical Properties of Perovskites

Unlike other semiconductors, organic-inorganic halide perovskites are easy synthesized materials with flexible component formation. For example, the substance at A, B or X site can be a single element to form perovskites like $MAPbI_3$ or mixed elements to form perovskites like $Cs_{0.05}(FA_{0.83}MA_{0.17})_{0.95}Pb(I_{0.83}Br_{0.17})_3$, which is able to greatly enrich the available candidates for applications. Moreover, this kind of perovskites can be processed by a myriad of technologies, including inexpensive solution process, thermal evaporation and epitaxy growth. The organic-inorganic halide perovskites also have attractive physical properties. For instance, the bandgap of organic-inorganic halide perovskites can be predominantly determined by the interaction of the halide p-orbitals and the s- or p-orbitals of the metal, as well as the size of A site cation. As a result, the bandgap of perovskite can be freely tuned by interchanging the cations, metals or anions in the range of 1.15 to 3.06 eV,[25] as shown in Figure 2.2. The tunable bandgap allows organic-inorganic halide perovskites to be applied in photovoltaic, light emitting diode, photodetector, laser and sensor. [26]
One of the organic-inorganic halide perovskite $MAPbI_3$ is widely used in photovoltaic devices because of its excellent optical and electrical properties. Firstly, its bandgap is around 1.55 eV which is nearly ideal for the

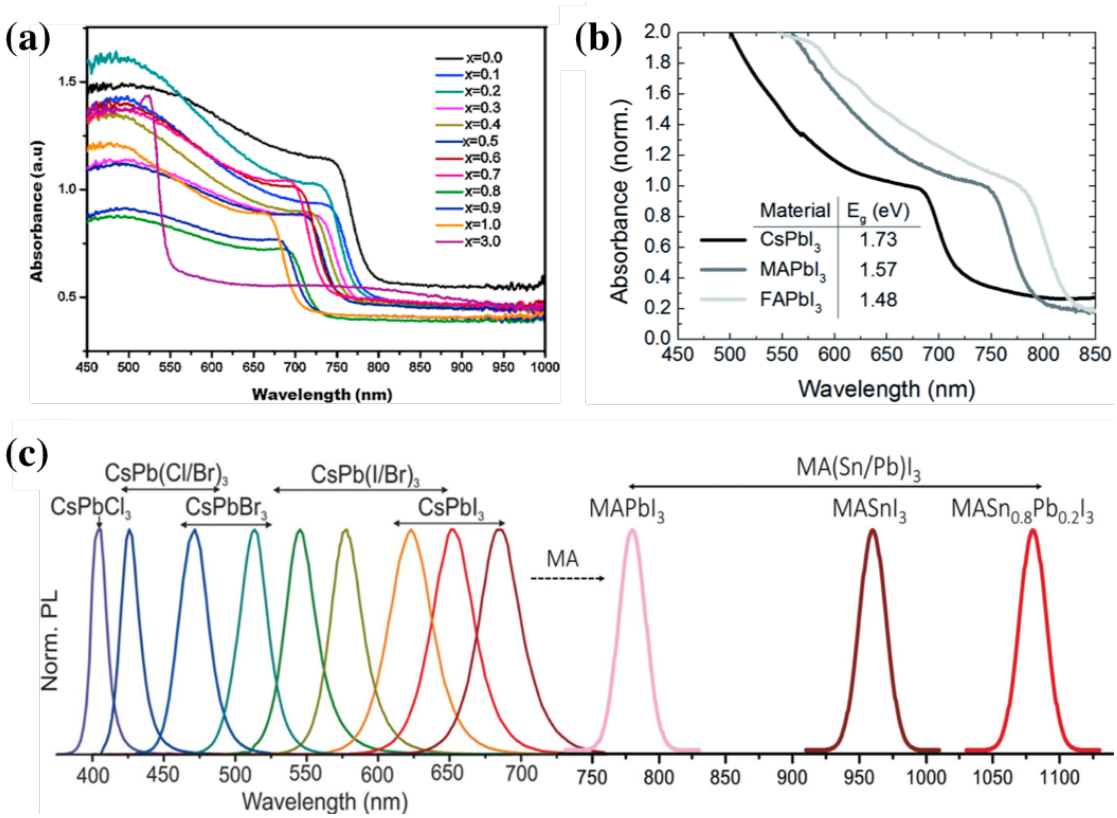

Figure 2.2: (a) Absorption spectra of $MAPbI_(3-x)Br_x$, adapted from [23] with Copyright 2016 Elsevier. (b) Absorption spectra of $APbI_3$ perovskite. Reproduced from [24] with permission from The Royal Society of Chemistry. (c) Representative photoluminescene spectra of $CsPbX_3$ extended towards $MA(Sn/Pb)I_3$ perovskites, adapted from [25] with Copyright 2018 John Wiley & Sons,Ltd.

single junction photovoltaic application.[27] The long pair *Pb* s-orbitals enable the high symmetry of p-p orbitals' electrons transition from conduction band to valence band resulting in a direct bandgap, which contributes to high optical absorption coefficients (10^5 cm^{-1}).[28] Secondly, the binding energy of $MAPbI_3$ has been experimentally determined to be 16 meV in orthorhombic phase and 12 meV in tetragonal phase from high field magneto absorption measurements, which indicates that in $MAPbI_3$ the photogenerated carriers behave as free carriers.[29] Thirdly, taking the spin-orbital coupling into consideration, the effective mass of electron and holes exhibit similar calculated results 0.23 and 0.29, implying an ambipolar characteristics of $MAPbI_3$. This ambipolar characteristics is further demonstrated by experimentally measured a balanced diffusion coefficient

of electron (0.036 cm^2/s) and hole (0.022 cm^2/s).[30, 31] Additionally, a large long carrier diffusion length in $MAPbI_3$ has been approved in the range from 1 μm (polycrystalline film) to over 100 μm (single crystal) with high charge carrier mobilities, strongly suggesting that charge carriers have a long lifetime with defect-tolerance and suppressed recombinations in $MAPbI_3$.[32–34]

2.1.3 Defects in $MAPbI_3$ Perovskites

Though organic-inorganic halide perovskite $MAPbI_3$ shows outstanding optical and electrical properties for applying in optoelectronic devices, still there are intrinsic point defects (e.g. vacancies, interstitials and antisites) and array configuration defects (e.g. Frenkel defects and Schottly defects) in $MAPbI_3$ to scatter and trap free charges as in other semiconductors.

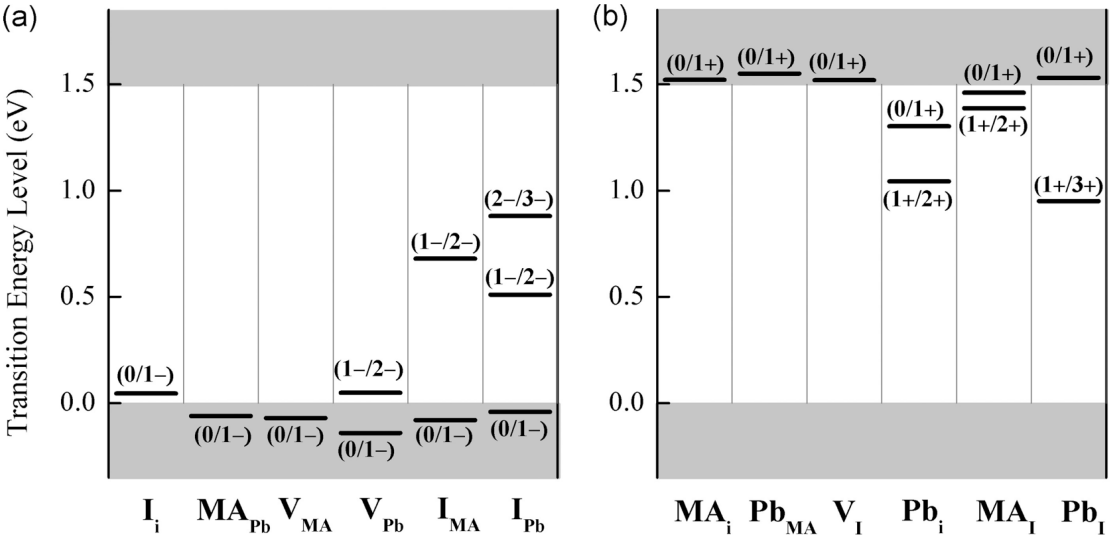

Figure 2.3: The calculated transition level of (a) intrinsic acceptors and (b) intrinsic donors in $MAPbI_3$. Reproduced from [35] with permission from American Physical Society, copyright 2014.

In principle, there are twelve possible intrinsic point defects in $MAPbI_3$, such as vacancies (V_{MA}, V_{Pb}, V_I), interstitials (MA_i, Pb_i, I_i) and substitutions (MA_{Pb}, Pb_{MA}, MA_I, Pb_I, I_{MA}, I_{Pb}).[35] The formation energy of

these defects creates a transition level which locates near the edge of conduction band/valence band or within the bandgap (shown in Figure 2.3) and acts as charge recombination centers to trap free charge carriers. The trapped charges can be released into the conduction/valence band if the transition levels are near the conduction/valence band edge as shallow trap states. Since the charge diffusion length in $MAPbI_3$ is long enough and the emitted photons from the shallow trap states that assist the radiative recombination can be reabsorbed, these shallow trap states are not a severe problem.[36] However, if the transition level locates within the bandgap as deep-level trap states (also known as Shockley-Read-Hall recombination centers), the trapped charges are doomed to be recombined via a non-radiative recombination process which annihilates the trapped charges to phonons, as a consequence the density and lifetime of charges are greatly reduced.[37, 38] Beyond point defects, higher dimensional defects such as grain boundaries, surface traps and microstructure imperfection are also existed in perovskites. The presents of defects not only lead to a damage of optoelectronic properties by affecting the charge recombination and transportation, but also influence the material stability and assist ion moving from one lattice site to the adjacent site.[39–42]
The formation of defects in $MAPbI_3$ is largely determined by the fabrication condition. For example, lower precursor concentration forms smaller grain size resulting in higher density of defects.[43, 44] Energetic disorder increases with the iodide to lead ratio, suggesting a demand of precise control on the precursor stoichiometry.[45] To minimize the defects in the perovskites, several noteworthy strategies have been investigated to produce high quality films, including doping the perovskite materials,[46–48] additive engineering[49, 50] and optimizing the deposition procedure[51, 52]. Beyond the treatment for bulk perovskite defects, the surface defects can also be greatly reduced by passivation layer.[53, 54]

2.2 Perovskite Solar Cells

2.2.1 Device Working Principle and Characterization

Perovskite solar cells are electrical devices which use perovskite as the main photovoltaic source to convert solar energy into electricity. Gener-

ally, a perovskite absorber is sandwiched by a n-type semiconductor and a p-type semiconductor to form a perovskite solar cell. It operates in an analogous manner to a thin film heterojunction solar cell.[55] In detail, when photons are absorbed by the perovskite, photon-generated excitons (bound electron-hole pairs) are created and dissociated into free electrons and holes due to a low binding energy. [56] Driving by the built-in potential which originates from the difference of work function between the two electrodes, these free charge carriers then diffuse throughout the film, extract by the respective charge transport layer to the electrode, and contribute to the current within an external circuit.

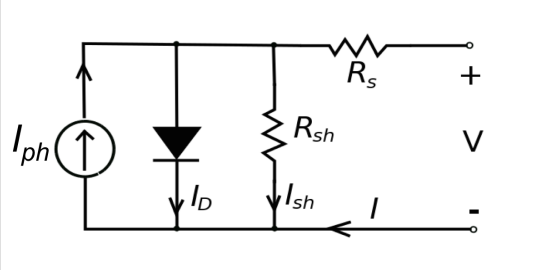

Figure 2.4: Equivalent circuit of a solar cell. V is the applied forward bias. For accounting the loss mechanisms, R_s and R_{sh} are the serial and shunt resistance, respectively.

As the solar cells are electrical devices, the equivalent circuit of a solar cell upon illumination is shown in Figure 2.4. A shunt resistance R_{sh} and a series resistance R_s are presented due to manufacturing defects and intrinsic resistance through the whole solar cell, respectively. Typically, the current of a solar cell can be divided into three parts, a dark current (I_D) that is determined by the diode properties of the solar cell, a photo-generated current (I_{ph}) and a shunt current (I_{sh}) that originates from the device imperfections. Generally, the current is converted to the current density by dividing the illuminated active area for a solar cell ($J = I/A$, where A is the illuminated area), the total current density of a solar cell is written in Equation 2.1. The dark current density is described by the Shockley p-n junction theory as Equation 2.2, where J_0 is the reverse saturation current density and n is the ideality factor. Both the J_0 and n describe the diode properties of the device and are determined by the device recombination mechanisms. [27] Based on Ohm's law the shunt current density is shown in Equation 2.3, and the final total current density can be written as Equation 2.4.

$$J = J_{ph} - J_D - J_{sh} \tag{2.1}$$

$$J_D = J_0 \exp[\frac{q(V + JR_s)}{nk_BT} - 1] \tag{2.2}$$

$$J_{sh} = \frac{V + JR_s}{R_{sh}} \tag{2.3}$$

$$J = J_{ph} - J_0 \exp[\frac{q(V + JR_s)}{nk_BT} - 1] - \frac{V + JR_s}{R_{sh}} \tag{2.4}$$

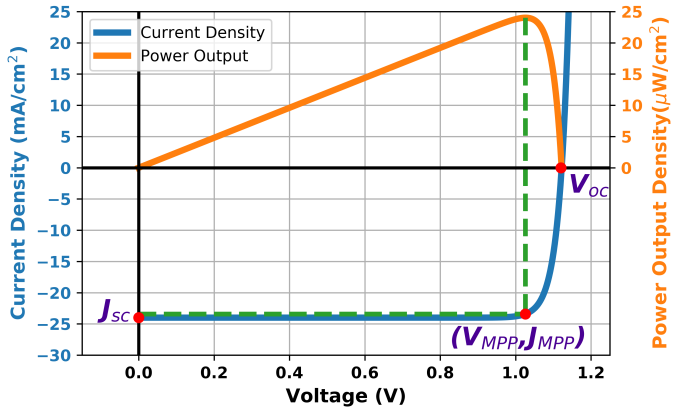

Figure 2.5: A simulated $J-V$ curve based on Equation 2.4 and the corresponding electrical power output density, with the assumption of $R_s \to 0$ and $R_{sh} \to \infty$. Annotations are the short-circuit current (J_{sc}), the open-circuit voltage (V_{oc}) and the maximum power output at (V_{MPP},J_{MPP}).

A simulated $J-V$ curve based on Equation 2.4 ($R_s \to 0$ and $R_{sh} \to \infty$) with the generated power output is plotted in Figure 2.5. When the output voltage is zero, the device shows its maximum generated current which is the short circuit current J_{sc}, and when no current flowing through the device, the device reaches the maximum voltage load which is the open-circuit voltage V_{oc}. As shown in Equation 2.6, the V_{oc} is related to n and J_0, which means that the device recombination process plays an important role on determining the V_{oc}. The fill factor (FF) is a dimensionless parameter which is determined by the maximum power of a solar cell at the maximum power output point. (Equation 2.7) It is noticeable that the voltage at maximum power output V_{mpp} can be obtained by $\frac{dJV}{dV} = 0$, thus FF is a function related to V_{oc}. The power conversion efficiency (PCE) of a solar cell is defined as the ratio of maximum generated power to the incident

power. (Equation 2.8, where $\Phi_E^{AM1.5G}$ is the sun power density on the Earth surface and A is the effective area for the device.)

$$J_{sc} = J(V = 0) = J_{ph} \tag{2.5}$$

$$V_{oc} = V(J = 0) \approx \frac{nk_BT}{q} \ln(\frac{J_{ph}}{J_0} + 1),\ R_s \to 0\ and\ R_{sh} \to \infty \tag{2.6}$$

$$FF = \frac{V_{MPP} \cdot J_{MPP}}{V_{oc} \cdot J_{sc}} = \frac{\frac{qV_{oc}}{nk_BT} - \ln(1 + \frac{qV_{oc}}{nk_BT})}{\frac{qV_{oc}}{nk_BT} + 1} \tag{2.7}$$

$$PCE = \frac{P_{MPP}}{P_{incident}} = \frac{FF \cdot V_{oc} \cdot J_{sc}}{\Phi_E^{AM1.5G} \cdot A} \tag{2.8}$$

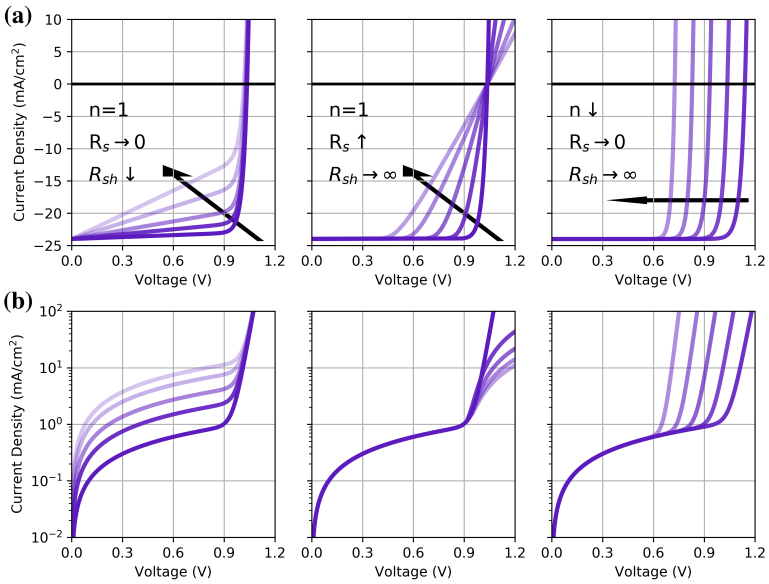

Figure 2.6: Simulated $J-V$ curves of a solar cell with different values of R_s, R_{sh} and n, (a) under illumination and (b) in the dark corresponding to the light J_V curves in (a). R_{sh} decreases from dark to light color curves in the left pattern, R_s increases from dark to light color curves in the middle and n reduces from dark to light color curves in the right pattern.

The $J-V$ curves of device tested under illumination and in the dark are mainly reshaped by the R_s, R_{sh} and ideality factor n, as shown in Figure 2.6. Generally, R_{sh} is regarded as infinity, while a low R_{sh} produces an alternate current path for losing photocurrent and reduces the FF in light $J-V$ and leakage current ($V=0$) in dark $J-V$. R_s exists in every solar cell, it can be enlarged by a bad contact of each adjacent layers. A high R_s will also reduce the FF in light $J-V$ and flatten curve tail in the dark J_V. While the ideality factor greatly affects the device V_{oc} and dark J_V 'knee' position. As shown in Figure 2.6 right pattern, it can be concluded that a shift of the 'knee' position in dark J_V corresponds to a shift in the V_{oc}.

2.2.2 Hysteresis in Perovskite Solar Cells

When scan the $J-V$ curve of perovskite solar cells in two directions, from J_{sc} to V_{oc} (forward scan) and from V_{oc} to J_{sc} (reverse scan), an anomalous hysteresis appears, which means the two curves do not overlap with each other and was first reported by Snaith et al. in 2014.[57] The mostly acceptable origin of hysteresis is the ion migration in the perovskite absorber, which is related to the defects in perovskite as discussed in Section 2.1.3. Due to the extensive ionic disorder, a significance of ionic conductivity consisting with mobile ions and interstitials, exists in organic-inorganic halide perovskite.[58] Direct observations of iodide and interstitials migration under electric field were reported by measuring the real-time PL measurement with specially designed PL system that is equipped with a charge-coupled device (CCD) camera in MAPbI_3 perovskite.[59, 60] Driven by an external electrical bias, the migration of ions and vacancies shift the effective work function of the respective electrodes, as a result the V_{oc} is enhanced and the $J-V$ curve hysteresis appears.[61] In reality, hysteresis is detrimental for the photovoltaic devices, as severe hysteresis causes poor stability and bad performance in solar cells.[62] Thus, strategies for reducing defects in perovskite bulk and surface have been investigated to reduce the hysteresis.[63]

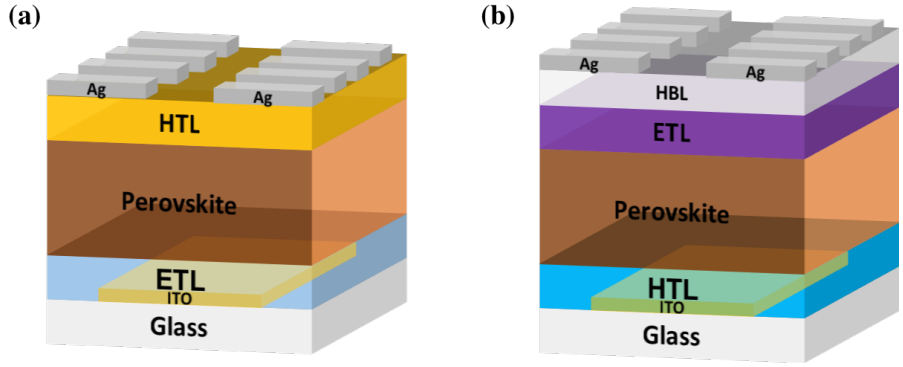

Figure 2.7: Schematic illustration of the perovskite solar cells architectures (a) standard architecture and (b) inverted architecture.

2.2.3 Device Architecture

Based on the order of charge transport layers, there are two architectures referred as 'standard' (n-i-p structure) and 'inverted' (p-i-n structure) in perovskite solar cells. (Figure 2.7)

Standard architecture (n-i-p structure)

In a standard architecture, typically a mesoporous or planar n-type metal oxide as an electron transport layer (ETL) is deposited first on the indium doped tin oxide (ITO) or fluorine doped tin oxide (FTO) substrates followed by the perovskite and hole transport layer (HTL) such as organic materials 2,2',7,7'-Tetrakis[N,N-di(4-methoxyphenyl)amino]-9,9'-spirobifluorene (Spiro-OMeTAD) and poly[bis(4-phenyl)(2,4,6- trimethylphenyl)amine] (PTAA).
In this structure, the n-type metal oxides have been focused on TiO_2, ZnO and SnO_2 as ETLs. Adapting from dye-sensitized solar cells, TiO_2 is the most commonly used ETL in n-i-p structure by far, however, it has several disadvantages. The electron mobility of TiO_2 is 0.1-10 $cm^2V^-1s^-1$ [64] which is several order of magnitude lower than that of ZnO (200-300 $cm^2V^-1s^-1$)[65] and SnO_2 (100-200 $cm^2V^-1s^-1$)[66]. The low electron mobility of TiO_2 increases the probability of charge recombination. Moreover, it requires a high temperature sintering step for preparing TiO_2 layer, rendering an unsuitable deposition on ITO or flexible plastic substrates.[67] Unlike TiO_2, ZnO and SnO_2 do not need a high fabrication

temperature. In addition to the high mobility, ZnO and SnO_2 has a broad bandgap and a deeper conduction band which is closer to electrodes than TiO_2, facilitating more efficient electron transfer in principle.[68, 69] Beyond these, ZnO offers higher transmittance in the visible to IR regions with lower resistivity and effective electron mass than TiO_2, and it is facile to prepare ZnO films via nanoparticles or sol-gel methods with low cost.[70, 71]

Inverted architecture (p-i-n structure)

In the inverted architecture, the HTL is deposited first, followed by the perovskite and fullerene based ETL such as [6,6]-phenyl-C61-butyric acid methyl ester (PCBM) or C_{60}. As the ETL may have relatively low ionization potential resulting in poor hole blocking and significant charge recombination, a high ionization potential material such as bathocuproine (BCP) is incorporated between ETL and metal cathode to reduce the leakage current and improve the device FF.[72, 73]
In the p-i-n structure, the most commonly used hole conducting polymer poly(3,4-ethylenedioxythiophene):poly(styr-enesulfonate) (PEDOT:PSS) is a well established HTL with high conductivity and low absorption in the visible range. [74] However, due to the energy level mismatch between PEDOT:PSS and perovskite absorber, significant energy losses appear at PEDOT:PSS/perovskite interface resulting in a lower V_{oc} and thus a lower PCE.[75] In order to resolve this issue and improve the V_{oc}, various strategies have been developed, such as changing the fabrication method of the perovskite layer for enhancing its quality,[76] doping the PEDOT:PSS layer to deepen its work function and enhance its conductivity[77, 78] or directly replacing it with other high work function HTLs, including polymeric materials such as poly(4-butylphenyl-diphenyl-amine) (PolyTPD) and PTAA, or inorganic hole transporters such as CuSCN and NiO.[79–82].
Among the deep work function hole transport materials, recently PTAA becomes the widely used HTL. Owning to its deep highest occupied molecular orbital (HOMO) energy level, PTAA is first introduced into n-i-p structure aiming to achieve higher V_{oc}.[83] Since PTAA is sustainability to DMF wash, it has been applied in p-i-n structure and also shown great capability

to increase the V_{oc}.[84]
In this work, the standard architecture with ZnO as an ETL is used in Chapter 4, the inverted architecture with doped PEDOT:PSS (m-PEDOT:PSS) and PTAA as a HTL is used in Chapter 5 and 6, respectively.

2.2.4 Efficiency Limit

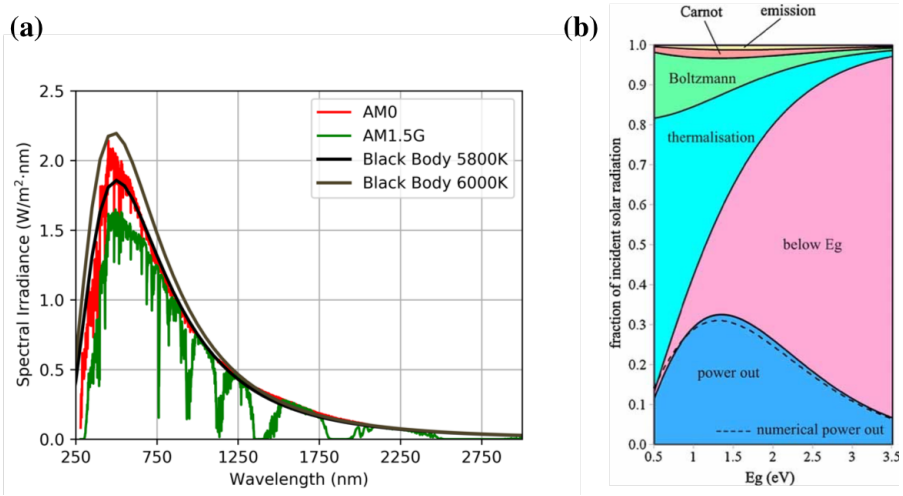

Figure 2.8: (a) Spectral irradiance of the sun illustrated as a function of the wavelength. AM0 and AM1.5G data adapted and replotted with permission from [85]. (b) Intrinsic losses in solar cells, power out is shown to be independent on E_g. Adapt from [86] with permission. Copyright 2010 John Wiley & Sons,Ltd.

As described in Equation 2.8, the PCE is determined by V_{oc}, J_{sc}, FF and $P_{incident}$. The solar irradiation defines the $P_{incident}$, however only photons with energy greater than the bandgap (E_g) of perovskite will contribute to the solar cell output power, a fraction of these photons will eventually be dissipated as heat. The spectral irradiance of the sun outside the atmosphere of the earth is plotted in Figure2.8(a) referred as the air mass 0 (AM0), which can also be approximated as black body radiation at temperature of 5800K. After crossing the earth atmosphere, the light spectrum is slightly changed with an angle α to the vertical at the earth atmosphere, a new AM number defined as $\frac{1}{\cos\alpha}$ is used to refer the new spectrum. The standard spectrum for solar cell characterization is AM1.5G with an integrated power density of 100 mW/cm^2, which is measured at $\alpha = 48.2°$ including diffuse component. Therefore, the $P_{incident}$ is a known constant for

the perovskite photovoltaic devices. Now, the purpose of achieving higher *PCE* can be addressed to how to minimize the energy losses in a solar cell. Figure 2.8(b) shows the fundamental losses of a single junction solar cell, which results from treating a solar cell as a heat engine working between the hot Sun and the cold atmosphere. As the photon with energy below the perovskite bandgap will not be absorbed, the non-absorption loss together with emission loss (based on Kirchoff's law, absorbers are also emitters) limit the maximum generated charge carriers and current of a solar cell. While the Carnot, Boltzmann and the thermalization loss (such as photo-generated charge carriers relaxing to the band gap edge) cause the reduction of the maximum voltage.[86] The latter three losses are also known as non-radiative recombination.

The theoretical maximum PCE of a solar cell which is also known as Shockley-Queisser limit (SQ limit), was based on detailed balance with assuming that a solar cell is an absorber with optically sharp bandgap E_g, and the solar cell has a direct absorption of solar irradiance with no non-radiative recombination.[27] Figure 2.9 shows the photovoltaic parameters limit under AM1.5G irradiance. Apparently, comparing to J_{sc} and FF, V_{oc} is the main factor to limit the photovoltaic efficiency for solar cells with different E_g. It is widely known that a fraction of the electron and hole recombination result in radiation and it is this radiative recombination that contributes to the V_{oc} of solar cell, $V_{oc} = V_{oc,rad} - \Delta V_{oc,non-rad}$.[38] Therefore, if radiative recombination is just a part of all the recombination, the efficiency is substantially lower than SQ limit. Hence, for reaching SQ limit in experiment, it is necessary to understand the recombination process in perovskite solar cells for minimizing the V_{oc} loss.

2.3 V_{oc} Loss Mechanisms in Perovskite Solar Cells

2.3.1 Non-radiative recombination

In photovoltaic devices, there are three main recombination processes, which are radiative recombination, trap assisted recombination (SRH recombination) and Auger recombination.(Figure 2.10) In perovskite solar cells, the Augur recombination can be eliminated as it has a negligible influence on the performance of device, while SRH is the main recombi-

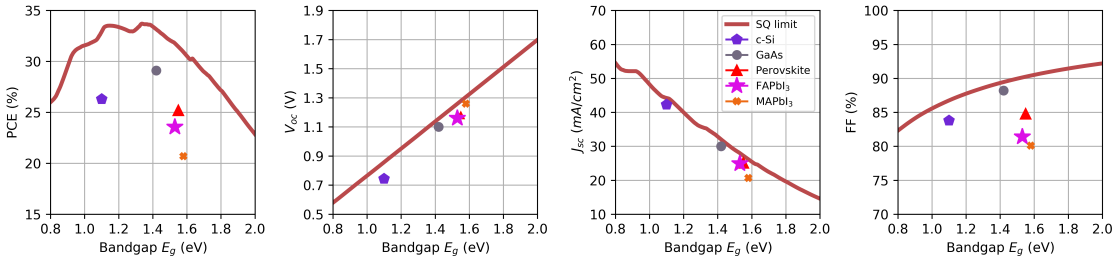

Figure 2.9: Photovoltaic parameters in SQ limits for a single junction solar cell as a function of the given bandgaps under AM1.5G irradiance. For $c-Si$, $GaAs$ and $Perovskite$ materials, the points indicate the values of the record cell. Points of $FAPbI_3$ and $MAPbI_3$ are reported values adapted from [53, 84].

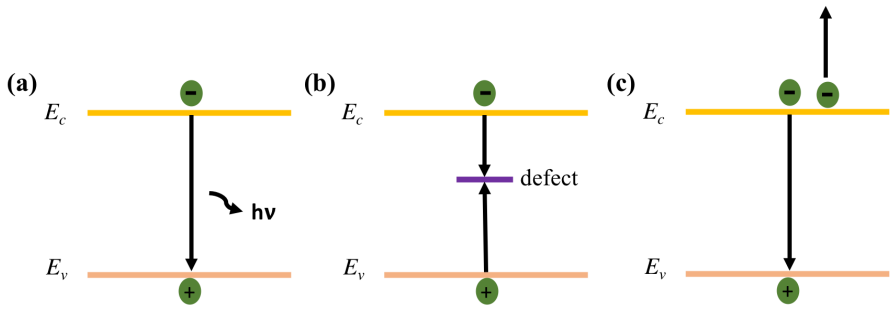

Figure 2.10: Three recombination processes in photovoltaic devices (a) radiative recombination which generates photons, (b) trap-assisted recombination which generates phonons and (c) Augur recombination which involves a third charge carrier.

nation loss mechanism.[87, 88]
SRH recombination occurs at in-gap trap states. In theory, a simple SRH recombination can be described into two steps[37]: a trap state captures an electron/hole from conduction/valence band and the electron/hole is emitted from the trap state back to conduction/valence band. Both steps can be presented as a product of capture coefficient (i.e., the thermal velocity times the cross section) and trap density. The final SRH recombination rate is the net rate of capture (i.e., capture minus emission). In steady state condition, after a long derivation the SRH recombination rate (R_{SRH}) that includes the net rate of both electrons and holes is found to be[37]:

$$R_{SRH} = \frac{np - {n_i}^2}{\frac{n+n_1}{C_p} + \frac{p+p_1}{C_n}} \tag{2.9}$$

where n is the electrons density in conduction band, p is the holes density in valence band, n_i is the density of electron in an intrinsic specimen, C_i is the capture coefficient of electron (n) or hole (p), $n_1 = N_c \exp\frac{E_t - E_c}{k_B T}$ (E_c is the energy of conduction band and N_c is the effective density of levels for conduction band) is the density of electrons at the trap state energy of E_t and $p_1 = N_v \exp\frac{E_v - E_t}{k_B T}$ (E_v is the energy of valence band and N_v is the effective density of levels for valence band) is the density of holes at the trap state energy of E_t. Notably, the R_{SRH} can also simply treat as a product of capture coefficient (C) and trap density (N_t). As the capture coefficient for a certain material is a constant, the target to suppress the R_{SRH} is associated to reduce the trap density (either via reducing the number of trap states or minority carriers). The distribution of traps in perovskite layer can be summarized into two parts: at the perovskite surface and in the perovskite bulk.
To minimize the bulk defects, various strategies have been discovered to improve the morphology and crystallization of perovskite films. For example, different fabrication procedures have been investigated such as sequential deposition,[89] vacuum deposition,[90] hot casting[76] and solvent engineering (antisolvent treatment)[91, 92]. Besides the deposition process, the precursor materials (different recipes)[84, 93] and stoichiometry[45] also play a role in determining the perovskite bulk defects. Previ-

ous works have demonstrated that a higher V_{oc} can be found in PbI_2 deficient or MAI rich films, as the extra organic specimens heal the defects at grain boundaries and enhance the crystal quality.[94, 95] Recently, additive engineer[96] and perovskite composition optimization (multication or multihalide)[47, 97] are two widely adapted way to achieve stable and less defects perovskite.
Other strategies have been targeted at passivating the traps at perovskite surface both on top and bottom. Inserting a thin insulator such as polystyrene (PS),[98, 99] poly(methy methacrylate) (PMMA)[100, 101] as interlayers between perovskite and the adjacent charge transport layer has been demonstrated not only passivates the perovskite surface defects but also improves the stability of device. High bandgap interlayers such as phenethylammonium iodide (PEAI)[53], choline chloride[102] are also employed as passivation layer. Both insulators and high bandgap materials suppress the recombination of minority carrier by blocking the minority carrier transferring from perovskite to transport layer.[98] Moreover, by incorporating secondary phases of perovskite such as 2D perovskite also improves the V_{oc} by reducing the trap sates and at the same time enhancing the moisture tolerance.[103, 104] Recently, absolute photoluminescence together with transient photoluminescence reveal that interface recombination at perovskite/charge transport layers dominates the non-radiative recombination leading to a lower quasi-Fermi level splitting that causes lower V_{oc}.[105, 106]

2.3.2 Energetic Misalignment

Another important factor to determine the V_{oc} is the energetic misalignment between the perovskite absorber layer and the charge extraction layers, which reduces the built-in potential leading to a decrease of V_{oc}. In an ideal case, the lowest unoccupied molecular orbital (LUMO) level (or conduction band edge) of the electron transport layer, the LUMO of perovskite and the fermi level of cathode perfectly align, as well as the highest occupied molecular orbital (HOMO) level (or valence band edge) of the hole transport layer (HTL), the HOMO of perovskite and the fermi level of anode perfectly align.(Figure 2.11(a)) However, in reality the fermi level of each electrodes is pinned in the bandgap of transport layers, and an energy

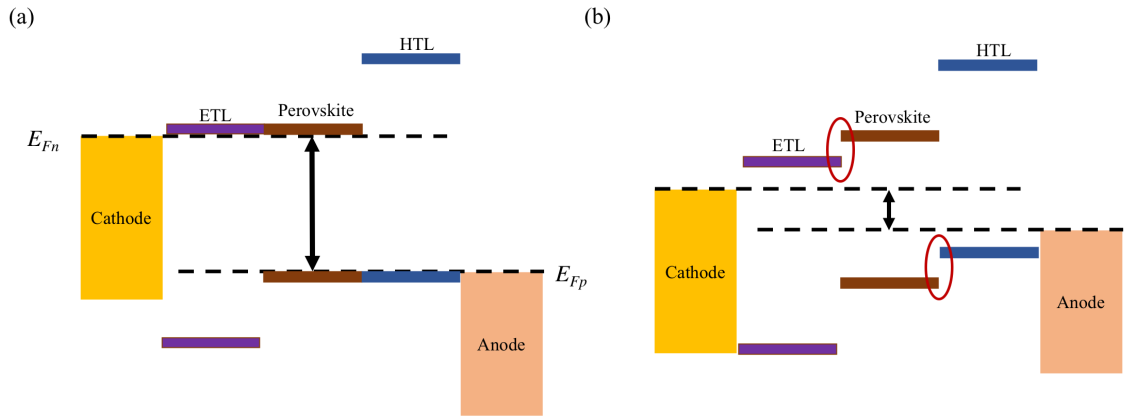

Figure 2.11: Energy schemes of (a) an ideal case and (b) a normal case with energy misalignment (point by red circle).

offsite is at the perovskite and the transport layers. These energetic misalignments will further reduce the build-in potential in the whole device, as well as the quasi-Fermi level splitting within perovskite and its transport layers.[107, 108]

To compensate the energetic misalignment and achieve higher V_{oc}, several strategies have been investigated. For example high work function materials such as PTAA, Poly-TPD and TFB are used to replace the commonly used low work function HTL PEDOT:PSS to reduce the energetic misalignment and push up the V_{oc}.[79, 109, 110] Doping the transport layers in order to deepen its work function also leads to a higher V_{oc}.[77, 78, 111] Enhancing the built-in potential via interface dipole or modify the cathode work function has been demonstrated to improve the V_{oc} and FF at the same time.[112–114] Moreover, the energetic disorder of transport layer affects the density of low energy states, resulting in an enhanced quasi-Fermi level splitting and a higher V_{oc}.[115]

Chapter 3

Experimental Methods

In this chapter, the fabrication processes of films and devices are described in detail. Starting from substrates cleaning, precursor solution preparation, film deposition to the electrode thermal evaporation as final step, a comprehensive overview of the fabrication processes is given. The techniques used in this work for characterizing physical and electrical properties of perovskite films and photovoltaic devices are also introduced.

3.1 Film and Device Fabrication

Thin films and planar perovskite solar cells were fabricated by the spin-coating method in this thesis. In detail, a small amount of precursor solution with target materials dissolved in suitable solvents was deposited on a rotated substrate. The solution was spread evenly by the rotation centrifugal force, forming a neat thin film with a thickness $d \backsim c/\sqrt{\omega}$, where c is the concentration of the precursor solution and ω is the rotation speed. The spin-coating was carried out statically (substrates covered with solution before rotation) or dynamically (solution spread on rotating substrates). After spin-coating, the residual solvent was eliminated and the materials were crystallized through a thermal annealing on a hotplate. Based on the properties of the materials used, the fabrication process took place either in ambient air, in a self-built drybox (filled with dry air, RH < 1%) or in a glovebox (filled with nitrogen, O_2 < 5ppm and H_2O < 2ppm). To complete photovoltaic devices, finally 80 nm of silver as electrode was thermally evaporated on top of the films in glovebox under high vacuum (base pressure 1^{-6} mbar).

3.1.1 Substrates

Depending on the purpose, pre-cut 12x12 mm^2 glass substrates (microscope slides, Thermo Scientific), pre-cut 10x10 mm^2 indium tin oxide (ITO) coated glass substrates and 12 mm diameter circular spectrosils that are made from high purity and fused silica glass (UQG Optics) were used to study films. Photovoltaic devices were prepared on 12x12 mm^2 sodal-ime glass substrates with a centrally positioned pre-pattered 7x12 mm^2 ITO stripes (PsiOTec Ltd). All ITO substrates exhibited a sheet resistance of 15 Ω/sq.
All substrates were successively cleaned in an ultrasonication bath with 2% Hellmanex III detergent, deionized water, acetone and isopropanol for 10 min and dried with compressed nitrogen. Before the deposition of the first layer, the cleaned substrates were treated for 10 min (100W) with an oxygen plasma.

3.1.2 Materials and Film Preparation Procedures

1. Hole Transport Layers:
m-PEDOT:PSS stands for doped PEDOT:PSS, It was pre-pared based on the previous report.[77] In detail, 15 mg/ml Poly(sodium 4-styrenesulfonate) (PSS-Na, Mw~70000, Sigma-Aldrich) was dissolved in de-ionized water and mixed with poly(3,4-ethylenedioxythiophene):poly(styr- enesulfonate) (PEDOT:PSS, Heraeus Clevios P VP Al 4083) in a 4:1 (v:v) ratio. The mixed solution was filtered by a 0.45 μm PVDF membranes filter before use. m-PEDOT:PSS was statically spin-coated on the substrates at 4000 rpm for 30 s following by a 10 min thermal annealing at 150 °C on a hotplate in ambient air. The resulting thickness was ~20 nm.
P3HT/PFN-P_2, Poly(3-hexylthiophene-2,5-diyl) (P3HT, Mw ~78000, 1-Material) was dissolved in anhydrous dichlorobenzene (99.8%, Sigma-Aldrich) with a concentration of 3mg/ml concentration and filtered through a 0.25 μm PTFE membrane filter prior to use. Film formation was carried out by spinning the solution statically in a glovebox at 3000 rpm for 30 s followed by 10 min annealing at 100 °C annealing. 0.5

mg/ml poly(9,9-bis(3'-(N,N-dimethyl)-N-ethylammoinium-propyl-2,7-fluorene)-alt-2,7-(9,9-dioctylflu-orene))-dibromide (PFN-P_2, 1-Material) in anhydrous methanol (99.8%, Sigma-Aldrich) as a surface compatibility was deposited on top of P3HT by 5000 rpm 30 s in the drybox.

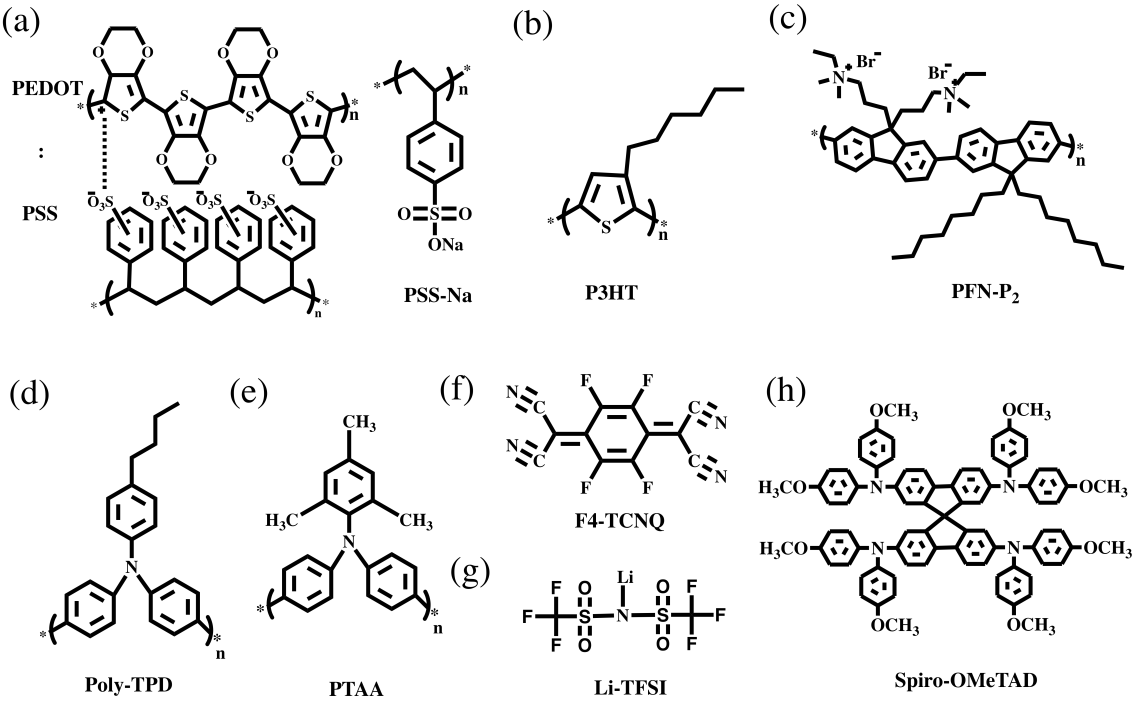

Figure 3.1: The chemical structure of the materials used to prepare the hole transport layers.

PolyTPD/PFN-P_2, a solution (2 mg/ml) of poly(4-butylphenyl-diphenyl-amine) (PolyTPD, 1-Material) in anhydrous chlorobenzene (99.8%, Sigma-Aldrich) was spin-coated on the substrates at 6000 rpm/30 s followed by a thermal annealing for 10 min at 120 °C annealing. PFN-P_2 was deposited on top as described above. Both layers were deposited in the drybox.

Poly[bis(4-phenyl)(2,4,6-trimethylphenyl)amine] (**PTAA**, Mn 7000-10000, Sigma-Aldrich) was dissolved in anhydrous toluene (99.8%, Sigma-Aldrich) with a concentration of 1.5 mg/ml. A roughly 8 nm thick PTAA layer was formed by spin-coating of the solution at 4000 rpm for 30s followed by a 10 min 100 °C annealing in the drybox.

m-PTAA represents doped PTAA. It was prepared based on the previous report.[80] 1%wt 2,3,5,6-Tetrafluoro-7,7,8,8-tetracyanoquinodimethane

(F4-TCNQ, 97%, Sigma-Aldrich) doped PTAA solution (1.5 mg/ml in anhydrous toluene) was spin-coated at 4000 rpm 30s and annealed at 100 °C 10 min in the drybox.

Spiro-OMeTAD is short for 2,2',7,7'-Tetrakis[N,N-di(4-methoxyphenyl) amino]-9,9'-spirobifluorene. Spiro-OMeTAD (80 mg/ml in anhydrous chlorobenzene, purchased from Borun Chemicals) with 17.3 µl lithium bis(trifluoromethanesulfonyl)imide (Li-TFSI, Sigma-Aldrich) that was dissolved in anhydrous acetonitrile (99.8%, Sigma-Aldrich)) at a concentration of 520 mg/ml and 28.5 µl 4-tert-butylpyridine (98%, Sigma-Aldrich) was spin-coated at 2000 rpm for 45s in the drybox. The deposited layers were left overnight in the drybox to oxidise before further use. Figure 3.1 illustrates the molecular structure of all above mentioned materials

NiO_x was prepared based on previous work.[116] Briefly, 0.1 mmol nickel acetate tetrahydrate was dissolved in 1 ml anhydrous isopropanol with 0.05 mmol ethanolamine. The solution was stirred in a sealed vial at 70 °C overnight, forming a homogeneous green solution. The NiO_x films were deposited by spin-coating at 1500 rpm 30 s and annealing at 275 °C for 1 hour in ambient air.

2. Perovskite Layer:

$MAPbI_3$ perovskite used in this thesis was based on lead acetate trihydrate ($Pb(OAc)_2 \cdot 3H_2O$) recipe.[117] In detail, $Pb(OAc)_2 \cdot 3H_2O$ (99.999%, Sigma-Aldrich) and methylammonium iodide (MAI, Greatcell Solar) were mixed in a 1:3 molar ratio and dissolved in anhydrous dimethylformamide (DMF, 99.8%, Sigma-Aldrich) to form a 40%wt solution. Before using, hypophosphorous acid 50% aqueous solution (HPA, Sigma-Aldrich) was added based on the amount of 1.7 µl per 100 mg MAI into the solution. Perovskite layers were prepared in a drybox by spin-coating at 2000 rpm for 60 s, followed by an immediate 25 s gentle blowing of dry air and a 5 min drying at room temperature. The final polycrystalline perovskite film was crystallized by thermal annealing at 100 °C for 5 min. In chapter 6 the weight ratio of the perovskite solution and HPA amount adding in the perovskite solution were varied.

3. Electron Transport Layers:
ZnO,ZnCsO and ZnLiO were prepared based on previous research.[118] Zinc acetate dihydrate (99.999%, Sigma-Aldrich) and ethanolamine (≥99%, Sigma-Aldrich) in equal mole of 0.46 were dissolved in 1 L anhydrous 2-nethoxyethanol (99.8%, Sigma-Aldrich) by heating and stirring at 70 ° for 2 hours in a sealed vial. Cs (ZnCsO) or Li (ZnLiO) dopants was accomplished by adding either cesium carbonate (99.995%, Sigma-Aldrich) or lithium acetate (99.95%, Sigma-Aldrich) to the ZnO solution in 2% or 3% molar ratio to Zn^{2+}, respectively. ZnO sol-gel solution (with or without dopants) was spin-coated at 2000 rpm for 45 s and annealed at 300 °C for 30 min in ambient air.
Self assembled monolayers of [6,6]-phenyl-C61-butyric acid (PCBA) modified ZnO, ZnCsO and ZnLiO were prepared following a previously reported procedure.[119] Briefly, 0.1 mg PCBA (Solenne BV) was dissolved in 5 ml anhydrous chlorobenzene and heated at 70 °C until fully dissolved. The ZnO, ZnCsO and ZnLiO substrates were immersed into the PCBA solution for 30 min. Subsequently, the samples were rinsed with anhydrous chlorobenzene (99.8%, Sigma-Aldrich) for 3 times to remove the excess PCBA and dried by a nitrogen gas gun in ambient air.
PCBM is short for [6,6]-phenyl-C61-butyric acid methyl ester. PCBM solution was prepared and used in glove box. In detail, PCBM was dissolved in anhydrous chlorobenzene with a concentration of 20 mg/ml. The formed solution was heated at 70 °C with stirring overnight. The solution was filtered through a 0.25 μm PTFE membrane filter before using. 25 μl PCBM solution was dynamically spin-coated on the samples at 2000 rpm for 30 s with a 10 min at 100 °C annealing. The chemical structures of PCBM and PCBA are shown in Figure 3.2.
SnO_2/PCBM, 0.05 M tin chloride dihydrate in methanol was spin-coated at 3000 rpm for 30 s and annealed at 195 °C for 1 hour with petri dish covering in ambient air. The as prepared substrates were transferred into the drybox, PCBM (7.5 mg/ml in anhydrous chlorobenzene) was spin-coated on top at 4000 rpm for 30s and 100 °C for 1 min as surface modifier.

4. Hole Blocking Layers:
2,9-Dimethyl-4,7-diphenyl-1,10-phenanthroline (bathocuproine, **BCP**,

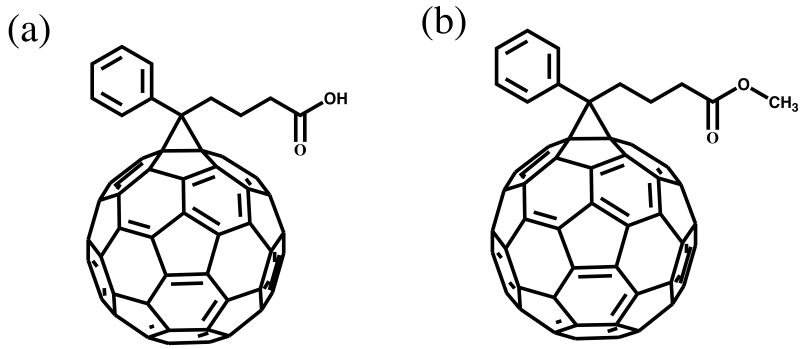

Figure 3.2: The chemical structure of (a) PCBA and (b) PCBM

99.99%, Sigma-Aldrich) was dissolved in anhydrous 2-propanol (99.5%, Sigma-Aldrich) at a concentration of 0.5 mg/ml. 35 µl BCP solution was dynamically spin-coated on the PCBM layers in the glovebox.

π-Extended Phosphoniumfluorene Electrolytes were synthesized by a cooperator Dr. Sebastian Arndt (Group of Prof. Hashmi, Institute for Organic Chemistry Heidelberg) and used as received.[120] The anion in all eight derivatives was bis(trifluoromethane)sulfonimide (TFSI). To apply the material as hole blocking layers in perovskite solar cells, π-extended phosphoniumfluorene electrolytes (0.5 mg/ml dissolved in anhydrous methanol (99.8%, Sigma-Aldrich)) were spin-coated on top of the PCBM at 4000 rpm for 30 s in the glovebox. The chemical structure of these electrolytes is displayed in Figure 3.3.

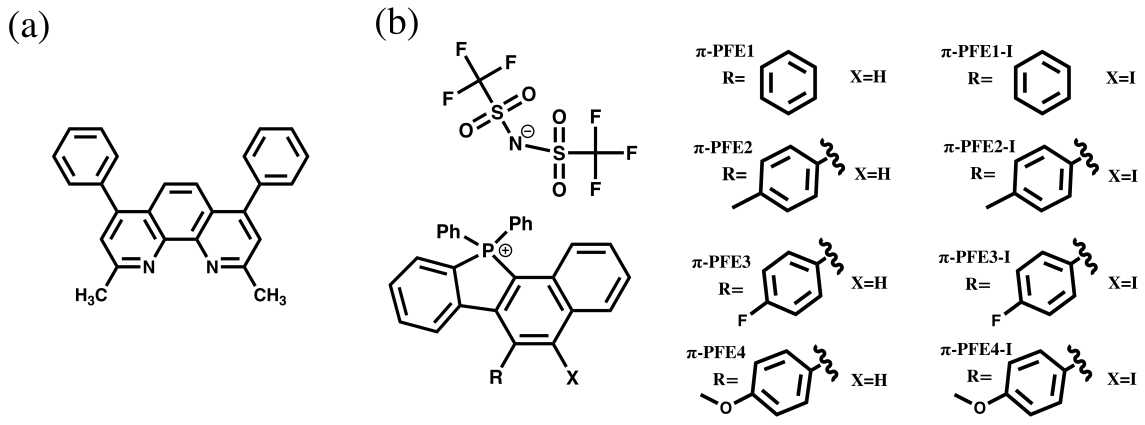

Figure 3.3: The chemical structure of hole blocking layers (a) BCP and (b) eight different π-extended phosphoniumfluorene electrolytes.

3.2 Material Characterization

3.2.1 Profilometry

A Bruker DektakXT Profilometer was used to measure the layer thickness of the fabricated films. Prior to the measurement that the films were scratched with a sharp tool on the surface without damaging the substrates. A stylus in contact to the sample's surface with a specified contact force was pulled slowly (10 μm/s) perpendicular to the scratch over the sample. The resulting hill-valley-hill profile was smoothed and leveled. The height difference between the hill and valley was the layer thickness. Several scans at different positions were conducted and averaged to obtain meaningful results.

3.2.2 Goniometer

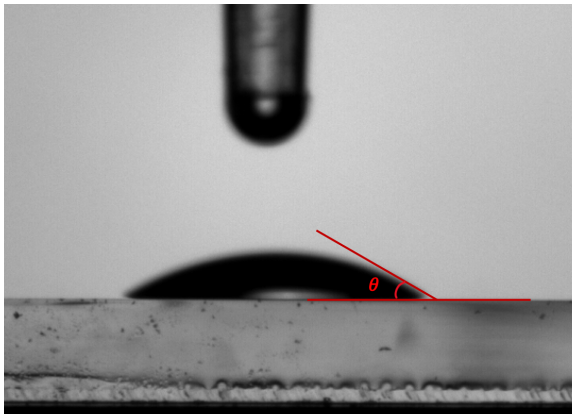

Figure 3.4: Illustration of the contact angle between a water droplet and a surface

The surface energy of substrates plays an important role on determining the coverage of the following layer. An easy way to compare the surface energy of different samples is by measuring the contact angle θ between a droplet and the surface, as shown in Figure 3.4. Based on Young's equation $\cos(\theta) = \frac{\gamma_{sv}-\gamma_{sl}}{\gamma_{lv}}$, where γ_{sv}, γ_{lv} and γ_{sl} are the surface tension between the solid-vapor, liquid-vapor and solid-liquid, γ_{sl} is proportion to $\frac{1}{\cos(\theta)}$. Therefore $\theta < 90°$ means a hydrophilic surface with low surface tension and $\theta > 90°$ means a hydrophobic surface with high surface tension. In

this thesis the contact angle measurements were conducted on a Rame-Hart 260 goniometer with an automated dispensing water system, imaged and analyzed by the Rame-Hart DROPimage Advanced software.

3.2.3 Absorption Spectroscopy

The optical absorption spectra were recorded on a Jasco UV-660 spectrophotometer in single beam mode. The monochromatic light with an intensity I_0 passes through the sample, and the light was partly absorbed, reflected, scattered and transmitted . The transmitted light intensity I was then detected by a photodiode. The background correction (empty substrate) was performed prior to the measurement to subtract the substrate absorption. The absorbance A is defined as $\mathrm{A}=\log\frac{I_0}{I}=-\log T=\alpha(\lambda)d$, where T is the transmittance, α is the absorption coefficient, λ is the wavelength and d is the layer thickness. If a sample strongly reflected or scattered too much light, an integrating sphere is used to measure the absorption spectrum. Since the ground state electrons are excited to the excited state by absorbing photons, the onset of the optical absorption spectrum also offers information about the film's optical bandgap.

3.2.4 Surface Morphology Measurements

Optical Microscope was performed on a Zeiss Axio Imager Z1and images were used to visualize the large area surface morphology of the thin films, especially to check for pinholes in a film. Three operation modes were routinely used. In bright-field mode (top illumination), sample contrast stems from the attenuation of the transmitted light in the dense areas of the sample. In dark-field mode (side illumination from the top), scattered light from the sample surface is detected, resulting in a visualization of rough areas of the sample with a high contrast. In transmission mode, light is illuminated from the bottom side through the sample and the substrate, and the light transmitted from the sample is detected to create the image. Thus, bright white parts in such images represent pinholes. Lateral resolution is limited by the diffraction limit and strctures below ca. 1 μm could not be reliably visualized. Therefore advanced methods were used.
Atomic Force Microscope (AFM) can visualize the surface topography

with a resolution smaller than hundreds nanometers. It is based on tracking the atomic force between a cantilever with a small radius tip and the sample surface to visualize the surface topography. (Figure 3.5) The tip is first attracted by Van-der-Waals forces and then repelled due to the Pauli principle. The tip is driven to oscillate at a fixed frequency (its resonance frequency in tapping mode and lower than resonance frequency in peak force mode) by a piezo element. When approaching the surface, the force interactions acting on the cantilever cause a modulation of the amplitude and phase of the tip oscillation. This modulation is revealed by the deflection of the laser that is pointed on the cantilever, and it is measured by a four-point-probe diode. In this work, all the AFM figures were measured on a Brucker Multimode AFM. The surface roughness and the perovskite grain size were determined using the software Gwyddion and MIPAR, respectively.

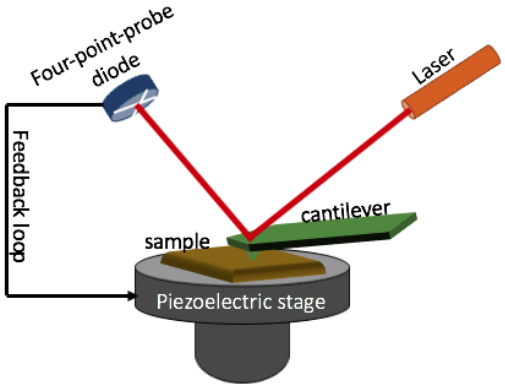

Figure 3.5: A Simple illustration of AFM working principle.

Scanning Electron Microscope (SEM) produces images of a sample by using a focused beam of electrons to scan the surface. The electron beam interacts with atoms at various depths within the sample, resulting in the emission of low-energy secondary electrons (SEs), reflected and backscattered high-energy electrons (BSE), characteristic X-rays, light from cathodoluminescence (CL), specimen absorbed current and transmitted electrons. All the signals can be detected by specified detectors. The top view SEM images in this work were taken by collecting the SEs which originate from the inelastic scattering of electrons in low energy levels such

as conduction or valence band by the interactions with the incident electron beam. Due to their low energy, the SEs can only be generated from the top few nanometers of the specimen and represent the topography of the samples. Some cross-section images were recorded in the Jeol SEI mode that combines the collection of SEs and BSEs to gain a better material contrast. Acceleration voltages were chosen depending on the working distance and sample properties and were in the range of 1.0-5.0 kV. The SEM imaging was performed on a Ultra FE-SEM Gemini Ultra 55 (Zeiss) and JSM-7610F FEG-SEM (Jeol). The SEM experiments were conducted by Dr. Paul Fassl and Dr. Fabian Paulus in Chapter 4 and Chapter 6, respectively.

3.2.5 X-ray Diffraction (XRD)

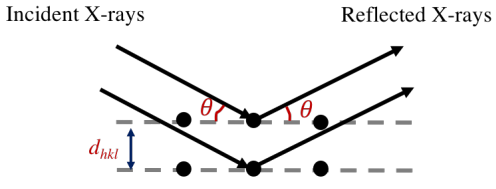

Figure 3.6: Schematic illustration the working principle of XRD

XRD is a nondestructive technique to identify crystalline phases, orientation and structural properties such as lattice parameters and strain. Figure 3.6 schematically illustrates the working principle of XRD. Incident X-rays with an incident angle θ will be either transmitted or scattered by the crystallographic planes in the specimen. The scattered X-rays are collected by a counting detector typically at an detector angle θ equal to the incident angle. Structural information of the sample (e.g. spacing of crystallographic planes) can be obtained whenX-ray waves with phase separated by an integer number of wavelengths interfere to create a new wave with a larger amplitude. This is represented by Bragg's law $n\lambda = 2d_{hkl}\sin\theta$, where n is an integer number, d is the distance between the crystallographic Miller planes with the Miller indicies (h,k,l), θ is the angle of incident X-ray and λ is the wavelength of the X-ray radiation. The full width half maximum (FWHM) of the diffraction peak is larger for smaller crystallite sizes or a non-uniform lattice strain. Changes is relative intensity between reflections of different Miller planes indicate changes in grain orientation

in the films. The XRD diffractogramms were acquired on a Rigaku Smart Lab X-Ray Diffractometer equipped with a 2D HyPix3000 detector and monochromated rotating copper anode (9kW, Kα λ = 1.5406 Å). 2D-XRD diffraction maps were recorded in a coupled θ-2θ scan, θ<45° using a 0.2 mmφ collimator and a knife edge to lower background scatterning. 1D-diffractorgramms were obtained from integrating a central wedge of the 2D dataset. Data was processed using the Rigaku Guidance and Rigaku SmartLab II software for background removal, integration, peak fitting with pseudo-Voigt functions and was carried out by Dr. Fabian Paulus.

3.2.6 Photoemission Spectroscopy (PES)

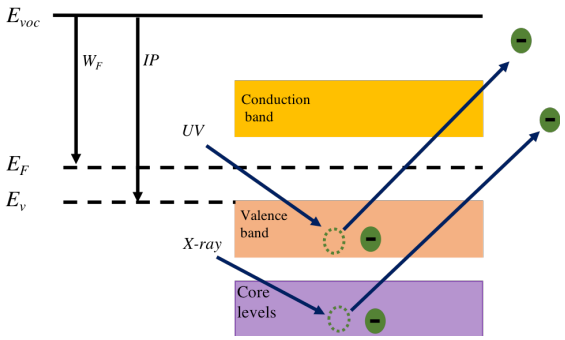

Figure 3.7: Working principle of PES and band energy diagram where W_F is the work function, IP is the ionization potential, E_{voc} is the vacuum level and E_v is the valence band.

Generally, there are two light sources in a PES system (Thermo Fisher Scientific ESCALAB 250 Xi), a XR6 monochromatic Al Kα source which generates X-ray photons ($h\nu$ = 1486.6 eV) with a passing energy of 20 eV and a differentially pumped He discharge lamp which generates ultra-violate photons ($h\nu$ = 21.22 eV) with a passing energy of 2 eV. The specimen core level electrons are emitted by absorbing the X-ray photons with kinetic energy E_k and detected by a detector, resulting in the X-ray photoemission Spectroscopy (XPS), while the valence band electrons absorb UV photons and emit with a kinetic energy E_k to form the Ultra-violet Photoemission Spectrum (UPS). (Figure 3.7) These measurements are measured under ultrahigh vacuum-typically 5x10^{-10} mbar for XPS and 5x10^{-8} mbar for UPS.

X-ray Photoemission Spectroscopy (XPS) is a surface sensitive technique (probing depth of only 10 nm). Since only electrons from the core levels can be detected, it is possible based on the binding energy (E_b)

to derive the elemental composition, elemental quantity and chemical state of the specimen. As the E_k of emitted electrons is detected, E_b can be calculated based on $E_b = h\nu - E_k - W_F$, where W_F is the work function (energy difference between the vacuum level and the fermi level). Moreover, to gain information about the bulk, an Ar cluster source with cluster energy of 4000 eV was used in this work to gently etch the specimen for further XPS measurement below the original surface.

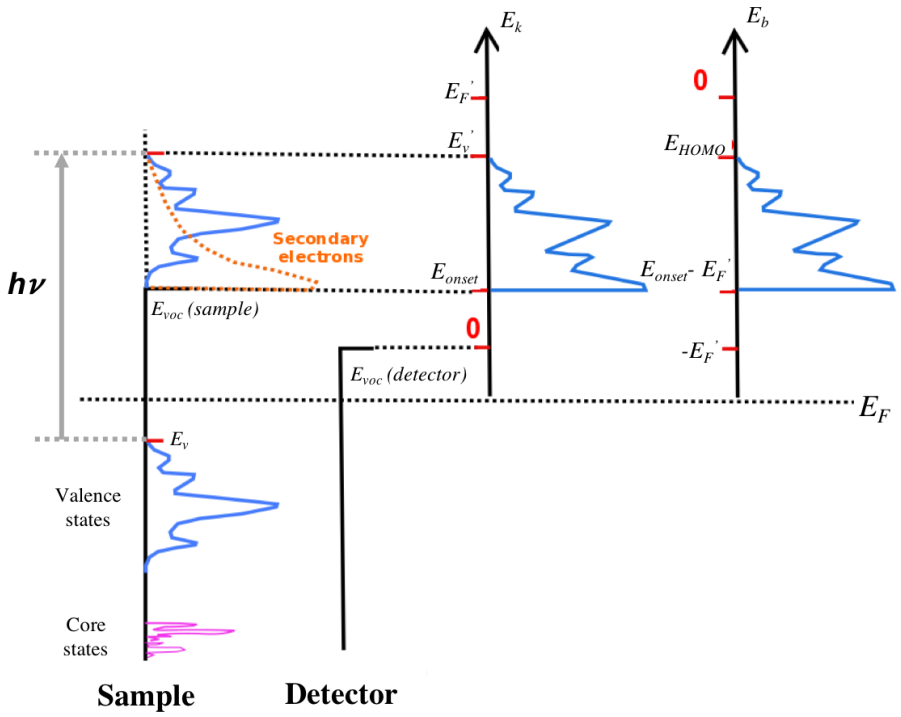

Figure 3.8: Working principle of UPS.

Ultra-violet Photoemission Spectroscopy (UPS) is also a surface sensitive technique and used to determine the electronic properties of materials. Figure 3.8 shows the working principle of UPS. The UPS spectrum consists of photoemitted electrons, which present the density of filled states in the valence band and the secondary electrons which are inelastically scattered. Electrons that have just enough energy to leave the sample, own the lowest kinetic energy E_{onset}. In order to include these electrons in the spectrometer response, generally a negative bias (ΔV) such as $-10V$ is applied.

Therefore the work function of the specimen $W_F = E_{voc}(sample) - E_F$ can be determined as

$$\begin{aligned} W_F &= E_{onset} - (E_{voc}(detector) - E_F) + e\Delta V \\ &= E_{onset} - (E_F{}' - hv) + e\Delta V \end{aligned}$$

where E_F is the detector's fermi level and $E_F{}'$ is the measured E_F from a clean metal sample such as gold. Furthermore, the ionization potential (IP) which is the energy difference between vacuum level and valence band, can be calculated based on $IP = W_F + E_{HOMO}$ in the binding energy regime. The PES measurements were carried out by Yvonne Jasmin Hofstetter in Chapter 4 and Dr. Qing Sun in Chapter 5 and 6.

3.2.7 Photothermal Deflection Spectroscopy (PDS)

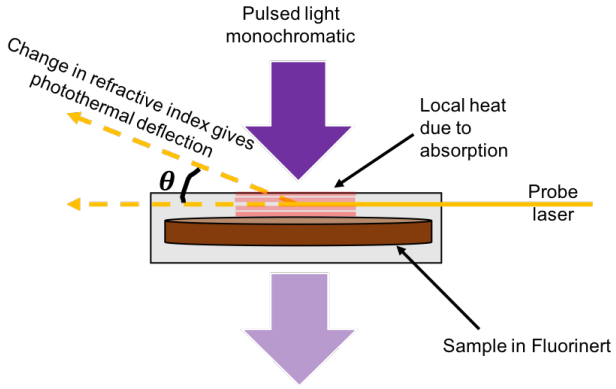

Figure 3.9: Simple illustration of the PDS measurement working principle.

PDS can be used to optically determine the sub-bandgap states of a semiconductor and the absorption of thin films with high sensitivity and allows to quantify even very weak absorption or to characterize very thin films. It is based on illuminating a sample with monochromatic light in an insert liquid that has a heat sensitive refraction index. A probe beam (typically laser light) is guided parallel and close to the sample surface. In case of an absorption of the monochromatic light, the heat of the sample changes the refractive index of the surrounding liquid, causing a deflection of the probe light with an angle θ due to the change of refraction index of the liquid(see Figure 3.9). This angle θ is proportional to the amount of absorbed light, namely the absorbance of the sample. In detail, samples for

PDS characterization were prepared on spectrosil in an identical way to those for photovoltaic devices. The samples were mounted in a sample holder filled with Fluorinert®FC-770 (IoLiTec) in a nitrogen filled glovebox. The samples were excited using a tunable, chopped, monochromatic light source (150W xenon short arc lamp with a Cornerstone monochromator) and probed using a laser beam (He-Ne laser from REO) propagating parallel to the surface of the sample. The heat generated through the absorption of light changed the reflective index of Fluorinert®, resulting in a deflection of the laser beam. This deflection was measured using a position sensitive-detector (Thorlabs, PDP90A). The magnitude of the deflection was determined by a lock-in amplifier (Amatec SR7230) and directly correlated to the absorption of the film.
In addition, the Urbach Energy E_u can be estimated by fitting the onset of the exponential PDS spectrum near the bandgap edge to determine the energetic disorder of the films, based on $A(E) = C \cdot exp\frac{E}{E_u}$, where A is the absorbance and C is a factor. Therefore, the PDS can also be used to characterize the energetic disorder of a material. All the data for PDS in this work were measured by David Becker-Koch.

3.2.8 Time Correlated Single Photon Counting (TCSPC)

TCSPC measures the time between the excitation pulse and the arrival of the emitted photon at the detector, resulting in a recessionary fluorescence curve. By fitting the fluorescence curve, the charge carrier lifetime can be calculated. In detail, a pulsed light from a 475 nm light emitting diode (LED) was used as the excitation source (pulse width ≈750 ps) with a repetition rate of 200 kHz and a fluency of 0.38 mJ/cm^2. The central wavelength of 775 nm was detected with a bandwidth of 25 nm. A triple-exponential function was fitted to the data $I(t)=A+B_1 \cdot e^{-\frac{t}{\tau_1}}+B_2 \cdot e^{-\frac{t}{\tau_2}}+B_3 \cdot e^{-\frac{t}{\tau_3}}$, where τ_i is the lifetime. The τ_i from the largest B_i is the extracted charges lifetime. The TCSPC data in this thesis were measured by Dr. Andreas Weu on a LifeSpec II TCSPC instrument (Edingburgh Instruments).

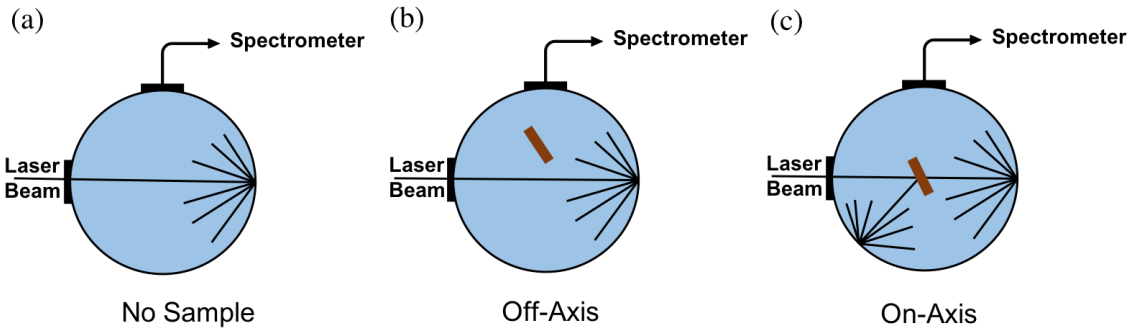

Figure 3.10: Three measurements need for determine the PLQE based on the method introduced by [121] (a) no sample, (b) sample off-axis and (c) sample on-axis.

3.2.9 Photoluminescence Quantum Efficiency (PLQE)

The PLQE is defined as $\eta = \frac{numberofemittedphotons}{numberofabsorbedphotons}$. To calculate the PLQE, the films prepared on glass were measured in an integrating sphere (also known as Ulbricht sphere) from Labsphere Inc. in three consecutive measurements, as shown in Figure 3.10. The interior side of the integrating sphere was covered with a white diffuse coating. This coating can scatter multiple times and redistributed light isotropically (regardless of the original directions of the beam), as a consequence the whole scattered light contributes equally to the measured spectrum. In the first step (Figure 3.10a), the laser intensity in the empty sphere was determined. In the off-axis step (Figure 3.10b), the sample was placed off-set to the laser path and only absorbed the scattered laser light. For the last step (Figure 3.10c), the sample was placed directly in the laser path (on-axis). In this configuration the light from direct illumination, reflection and scattering can be absorbed by the sample. The PLQE then can be calculated by $\eta = \frac{P_{on}-(1-A)\cdot P_{off}}{L_{empty}\cdot A}$ and $A = 1 - \frac{L_{on}}{L_{off}}$, where A is the fraction of the incident light absorbed by the sample in the on-axis step; L_{empty}, L_{off} and L_{on} are the area under the laser peaks in no sample, off-axis and on-axis steps, respectively; P_{off} and P_{on} are the area under the photoluminescence emission peaks in off-axis and on-axis steps.

In this work, 532 nm continuous wave laser was used as the light source with a spot size of 2 mm. The optical system (integrating sphere, spectrometer, and coupling optical fiber) were calibrated using a calibrated light source (Ocean Optics HL-2000-CAL). The PLQE can be used to quantify

the radiative recombination and the quenching properties of the transport layers.

3.2.10 Electroluminescence Quantum Efficiency (ELQE)

Electroluminescence occurs when charges are injected from the electrodes and recombine in the active layer to emit light. Therefore, devices with high ELQE suggest a low non-radiative recombination compared to devices with low ELQE. The ELQE was determined in an integrating sphere (the same as PLQE). The injected current and voltage were measured by a source meter unit (Keithley 2450). The emitted light spectrum was recorded using a scientific grade spectrometer (Ocean Optics QE65PRO) and converted to luminance immediately.

3.3 Device Characterization

3.3.1 Transient Photovoltage/Photocurrent (TPV/C)

TPV and TPC measurements are used to study the charge recombination and extraction through the whole device. For TPV/C measurements, the light of an inorganic LED (Thorlabs TO-1 $\frac{3}{4}$, λ = 465 nm) was pulsed by a function generator (Agilent/Keysight 33510B) and focused on the solar cell. TPV measurements were measured under open circuit conditions that a white light bias (100 mW/cm^2 irradiation) was illuminated on the solar cell, while TPC measurements were conducted under short circuit conditions that no light bias was applied. An oscilloscope (Picoscope 5443A) with and without a 50 Ω terminator was used to measure the transient photocurrent and transient photovoltage, respectively.

3.3.2 Charge extraction measurement (CE)

Charge extraction measurement is used to determine the steady state carrier concentration (n) at open circuit condition by a procedure known as 'differential charging'.[122] In principle, CE is based on TPV and TPC measurements (above mentioned). In detail, the voltage decay measured from TPV is given by $\Delta V = V_{oc} + \Delta V_0 e^{-t/\tau}$, where V_{oc} is the open circuit voltage under each intensity of the white light bias and τ is the recombina-

tion time that can be derived from a single exponential decay fitting from the TPV curves. While loading a resistant (a 50 Ω terminator in our set-up) to let the devices work under short circuit condition (TPC), the current decay is given by $\Delta I = \Delta I_0 e^{-t/\tau}$. By integrating the current, the total charges that are generated by the light pulse can be calculated as $\Delta Q = \int Idt$ under the assumption that the generated charge pairs are independent of the electric field and the recombination losses at short circuit are negligible.[123] When a small charge ΔQ is added to the device, the differential capacitance C is defined as $C = \Delta Q / \Delta V_0$. Thus, the carrier concentration n at each measured V_{oc} from the relative TPV measurement can be obtained by integrating the differential capacitance over the voltage as $n = \frac{1}{Aqd} \int_0^{V_{oc}} CdV$, where A is the device area, q is the electron charge and d is the device thickness.

3.3.3 External Quantum Efficiency (EQE)

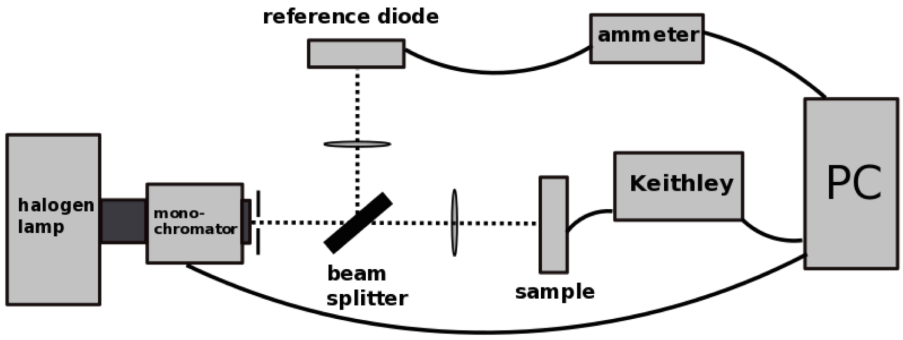

Figure 3.11: Schematic illustration of the EQE setup.

The setup of EQE used in this work is schematically illustrated in Figure 3.11. EQE at a certain wavelength is the ratio of photo-generated electrons from the device under short circuit conditions to the number of incident photons. The EQE spectrum of measured solar cells contain information about the bandgap of the active layer (the onset of EQE spectrum), the properties of charge extraction and the thickness of the active layer (bad charge extractions and thin active layers cause low EQE value), as well as about the predicted short circuit current J_{sc} ($J_{sc,pre} = \int_{\lambda 1}^{\lambda 2} \mathrm{e} \cdot \mathrm{EQE}(\lambda) \mathrm{I}_{AM1.5}(\lambda) \mathrm{d}\lambda$, where e is the electron charge and $I_{AM1.5}$ is the

photon flux of the AM 1.5 solar spectrum). Moreover, the spectral mismatch (M) between the solar spectrum from the solar simulator, which is used to measure the photovoltaic devices and the AM 1.5 solar spectrum can be calculated by integrating the EQE spectrum of the reference diode over the solar simulator spectrum and the AM 1.5 real solar spectrum following $M=\frac{J_{ref}^{SIM}}{J_{ref}^{AM1.5}} \cdot \frac{J_{device}^{SIM}}{J_{device}^{AM1.5}}$.

3.3.4 Photovoltaic Performance Measurement

The current density-voltage ($J-V$) curves were measured by a Keithley 2450 Source Measure Unit under the illumination of AM 1.5 sunlight with a 100 mW/cm^2 irradiation from an Abet Sun 3000 Class AAA solar simulator. The light intensity was corrected by a silicone reference cell with the spectral mismatch factor (M) obtained by the EQE measurement prior to testing. The $J-V$ curves were conducted in air without encapsulating the devices and scanned in both forward (from J_{sc} to V_{oc}) and reverse (from V_{oc} to J_{sc}) direction with a rate of 0.25 V/s. No pre-biasing was performed.

3.3.5 Light Intensity Dependent V_{oc} Measurement

Light intensity dependent V_{oc} measurement provides information about the recombination losses under open circuit condition in a device. Experiments were conducted by measuring the photovoltaic performance under different illumination intensities. The solar simulator was kept constant with an AM 1.5 sunlight, 100 mW/cm^2 irradiation output, and the light intensity was changed by inserting neutral density filter (ND) with different optical density above the photovoltaic cells. The relation of ND number and light intensity is summarized in Table B.1.
In principle, when bimolecular (Langevin) recombination is the dominant recombination mechanism in the solar cell, the differential of V_{oc} can be described as $\delta V_{oc} = \frac{k_B T}{q} lnI + constant$, where k_B is the Boltzmann constant, T is the absolute temperature, q is the electric charge and I is the incident light intensity. Thus the slope of V_{oc} versus the natural logarithm of the light intensity is given by $\frac{k_B T}{q}$, while for the monomolecular recombination, the slope turns to be $2\frac{k_B T}{q}$.[124, 125] As the dominant recombination in the

perovskite solar cells is mainly trap-assisted recombination (bimolecular), the slope is normally determined to be below $2\frac{k_B T}{q}$.[126–128] A slope close to unity indicates minimal recombination losses in the device.

Chapter 4

ZnO/Perovskite Interface Engineering in Standard Architecture Devices

This chapter is based on our publication in *"High performance planar perovskite solar cells by ZnO electron transport layer engineering"* Q. An, P. Fassl, Y. J. Hofstetter, D. Becker-Koch, A. Bausch, P. E. Hopkinson, Y. Vaynzof, Nano Energy 39, 400-408 (2017). Briefly, we investigate the interface between Zinc Oxide (ZnO) and the $MAPbI_3$ perovskite, aiming to achieve high performance perovskite solar cells by using ZnO as an electron transport layer (ETL) in standard architecture perovskite solar cells. We demonstrate that a complete solution process low temperature engineering of ZnO ETL by doping and surface modification with a self-assembled monolayer, allows us to push the perovskite $MAPbI_3$ photovoltaic efficiencies up to 18%, which is comparable to devices made on other metal oxide such as TiO_2 and SnO_2. After a thorough characterization of the engineered ZnO ETL and devices, we discuss on the origins of the improvements in device performance.

4.1 Introduction

The low fabrication temperature and high electron mobility of ZnO suggest that it is an attractive ETL in perovskite solar cells (Section 2.2.3), however, ZnO has received comparatively little attention due to severe instability of ZnO/perovskite interface and lower device performance. After Liu et al. reported a promising highly efficient perovskite solar cells based on ZnO ETL [129], subsequent investigations have revealed that under thermal annealing, perovskite films suffer from a decomposition on ZnO surface. This unwanted effect stems from the presence of hydroxyl groups or the residual acetate ligands from the ZnO precursor solution at the surface.[130, 131] Even in the absence of these groups, the proton transfer reactions take place at the perovskite/ZnO interface, which causes the methylammonium (MA^+) cations to release methylamine and results in the decomposition of perovskite.[132] Beyond the negative influence on the perovskite, the bulk and surface defects of ZnO act as recombination centers that adversely affect the photovoltaic performances.[133]
To reduce the defects in the ZnO layer, part of the researches have been focused on improving the quality of ZnO layer through doping or by using alternative deposition methods such as sol-gel, chemical bath deposition (CBD), radio frequency (RF) sputtering or atomic layer deposition.[134–138] However, though these treatments improve the quality of ZnO layer, the photovoltaic performance is still significantly lower on devices utilizing ZnO as an ETL than those using TiO_2 or SnO_2. Others have addressed the ZnO/perovskite interface stability concerns by modifying the ZnO surface with a passivation layer such as 3-aminopropanioc acid, magnesium oxide, ethanolamine, graphene and ZnS to push the performance of ZnO based solar cells to over 20% and achieve stable devices.[64, 139–141] Recently, MA-free perovskite has been demonstrated to overcome the ZnO/perovskite interface instability by offering greater thermal stability and superior UV stability.[142]
In this chapter, we incorporate Cs or Li dopants in the ZnO bulk and modify the ZnO surface with a PCBA self-assembled monolayer. We completely engineer both the bulk and surface properties of a solution-processed ZnO ETL at relatively low temperatures. When applying the engineered ZnO

layer as an ETL in planar $MAPbI_3$ perovskite solar cells, the engineered ZnO ETLs result in significant improvements in the photovoltaic performance with a maximum power conversion efficiency of 18%, accompanied by a reduction in hysteresis and an enhancement of the device stability.

4.2 Electron Transport Layer Modification

ZnO electron transport layers were processed from a sol-gel solution using a zinc acetate precursor. Lithium acetate or cesium carbonate were added into the ZnO solution as dopants, forming $ZnLiO$ and $ZnCsO$ ETLs. To modify the surface of the ETLs, a self-assembled monolayer (SAM) of PCBA (Figure 3.2(a)) was applied.

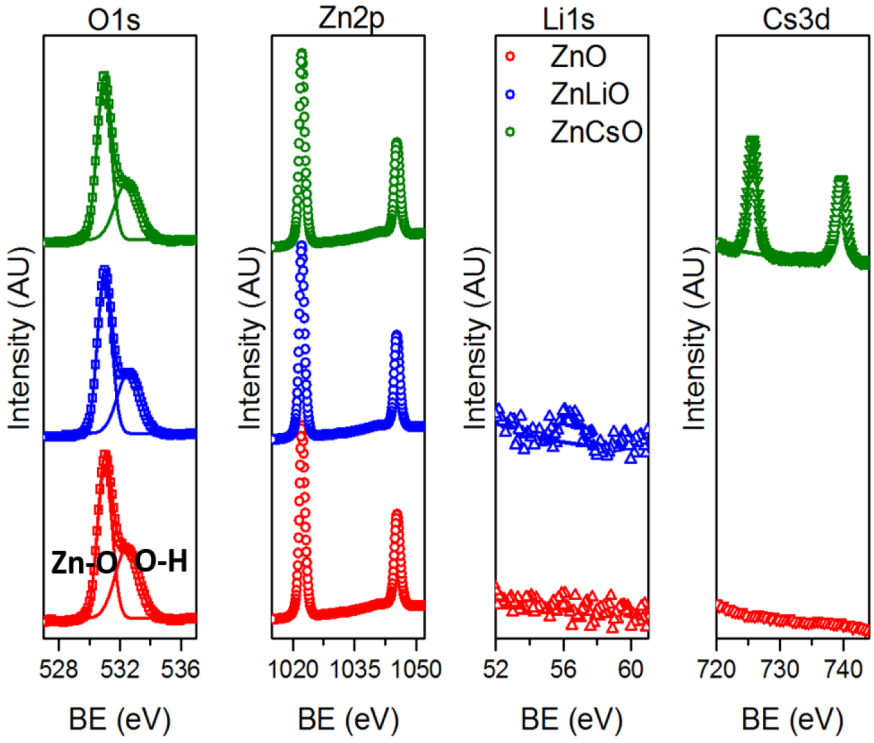

Figure 4.1: $O1s$, $Zn2p$, $Li1s$ and $Cs3d$ XPS spectra measured on ZnO, $ZnLiO$, $ZnCsO$ layers.

In terms of characterization, we first used the X-ray photoemission spectroscopy (XPS) to examine both the incorporation of the dopants into the inorganic layers and the coat of PCBA SAM on the inorganic

layers. Figure 4.1 shows the $O1s$, $Zn2p$, $Li1s$ and $Cs3d$ spectra obtained on ZnO, $ZnLiO$ and $ZnCsO$ films. In the $O1s$ spectra, there are two peaks of oxygen bonds for all three types of films. One peak is $Zn-O$ bond appearing at low binding energy (531 eV) and the other one is $O-H$ bond at high binding energy (532.5 eV).[143] Two peaks in $Zn2p$ spectra represent electrons emitted from the $Zn2p_{3/2}$ orbital (1021 eV peak) and the $Zn2p_{1/2}$ orbital (1044 eV peak). As expected the $Li1s$ peak was only detected in $ZnLiO$, and the $Cs3d$ peak was only in $ZnCsO$, indicating a successful doping of Li or Cs into ZnO. The atomic percentage of Li and Cs are 3% and 2% respectively, which is consistent with the stoichiometry of the precursor solution. Figure A.1 shows the XPS spectra of $C1s$, $O1s$ and $Zn2p$ of ETLs with and without PCBA coating. In addition to the appearance of strong $C1s$ peak, a large drop in the peak intensities for $Zn2p$ and $O1s$ can be seen for samples with PCBA, confirming a PCBA shield on the ETLs with suppressed surface hydroxyl bonds. Moreover, a similar thickness of the PCBA (~10-11Å) was estimated from the attenuation of the $Zn2p$ peak, which is in agreement with the reported thickness for a fullerene monolayer.[144]

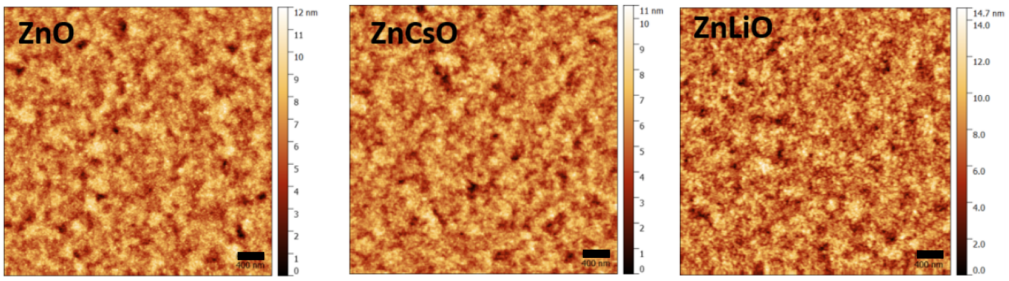

Figure 4.2: AFM graphs of ZnO (left), $ZnCsO$ (middle) and $ZnLiO$ (right). The scale bar is 400 nm.

Secondly, the microstructure of ETLs was characterized by the atomic force microscopy (AFM) and shown in Figure 4.2. All the films exhibit smooth and homogeneous with a similar roughness of 1.3 nm in ZnO, 1.16 nm in $ZnCsO$ and 1.78 nm in $ZnLiO$. This similarity illustrates that Cs and Li dopants have nearly no effect on ZnO surface structure. However, previous report has shown that the surface properties of doped ZnO may influ-

ence the formation of the PCBA monolayer.[145] Since the PCBA monolayer is such a thin layer that traditional UV-vis can not probe its weak absorption, we employed a more sensitive method, photothermal deflection spectroscopy (PDS) to measure the absorption of PCBA monolayer. As shown in Figure 4.3(a), both doped and undoped *ZnO* have a nearly identical absorption with the PCBA monolayer, indicating that the coverage of PCBA on all three surfaces is very similar.

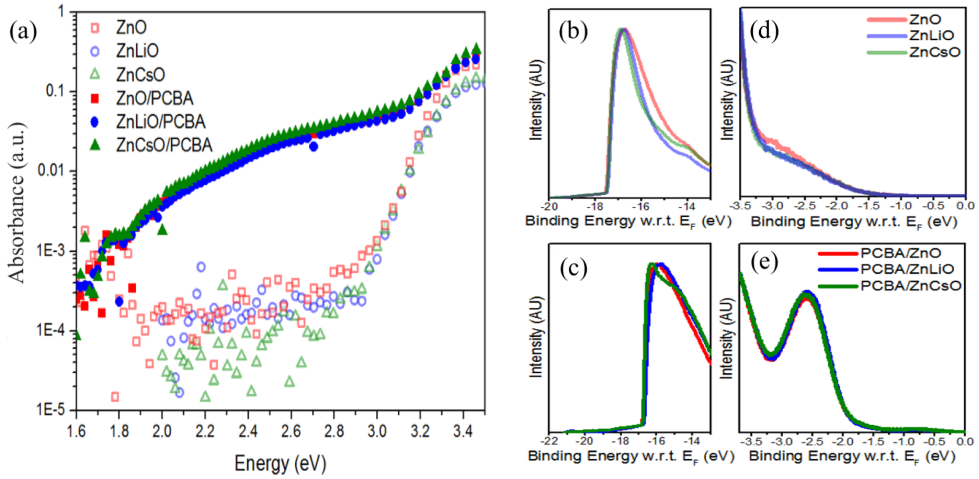

Figure 4.3: (a) PDS of bare and PCBA modified *ZnO*, *ZnCsO* and *ZnLiO*. (b) and (c): UPS of the secondary emission onset of *ZnO*, *ZnCsO* and *ZnLiO* with (b) and without (c) a PCBA monolayer. (d) and (e): UPS of the valence band region of *ZnO*, *ZnCsO* and *ZnLiO* with (d) and without (e) a PCBA monolayer

Finally, the ultraviolet photoemission spectroscopy (UPS) was used to characterize the electronic structure of engineered *ZnO* ETLs. With doping only (without the SAM), both the secondary emission onset (Figure 4.3(b)) and the valence band onset (Figure 4.3(d)) of ETLs remain unchanged, leading to a work function (WF) of 3.6 eV and an ionization potential (IP) of 6.8 eV, which are similar with previous reports.[146, 147] The same WF and IP strongly suggest that doping alone does not alter the energy levels of *ZnO*. However, PCBA modified ETLs show a 0.65 eV shift of the secondary emission onset, deepening the work function to 4.25 eV. The new valence band onset is found to be 1.9 eV below the Fermi level, and as a result the ionization potential is shifted up to 6.15 eV. A

summary of energy diagram of ETLs before and after PCBA modification is in Figure A.2.

4.3 Perovskite on Engineered ZnO ETLs

So far, we have demonstrated a successful engineering on ZnO bulk with Cs or Li and on the surface with a PCBA SAM at the same time. For depositing perovskite on solution processed ZnO, most previous reports employed a two step inter-diffusion method by depositing MAI on top of the PbI_2 film, and to limit the decomposition of perovskite caused by elevated annealing temperature, a minimized heat treatment for the final perovskite film was applied.[148, 149] In this work, we use the lead acetate trihydrate perovskite recipe that offers a simple one-step perovskite deposition method, producing ordered crystalline perovskite with superior electronic quality and highly efficient devices on either n-type or p-type transport layers.[93, 150] Since, a precise control of the processing parameters is essential to attain high quality $MAPbI_3$, we optimize the annealing procedure by employing a low temperature of 80 °C for 30 min. This procedure lead to a complete conversion of perovskite, and at the same time minimize the heat-induced degradation.

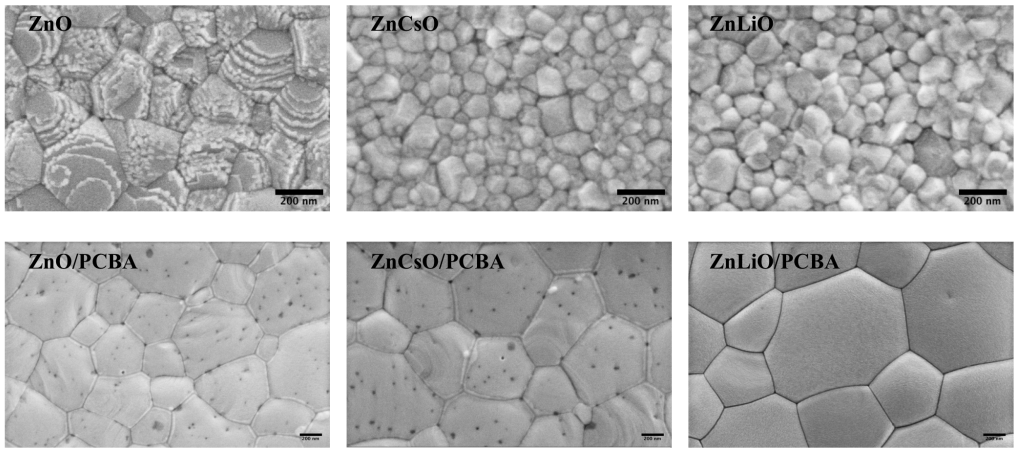

Figure 4.4: SEM top view images of perovskite films on bare and PCBA modified ZnO, $ZnCsO$ and $ZnLiO$. The scale bar is 200 nm.

The formation of perovskite films on doped and undoped ZnO layers with and without PCBA SAM were characterized by the SEM with top view

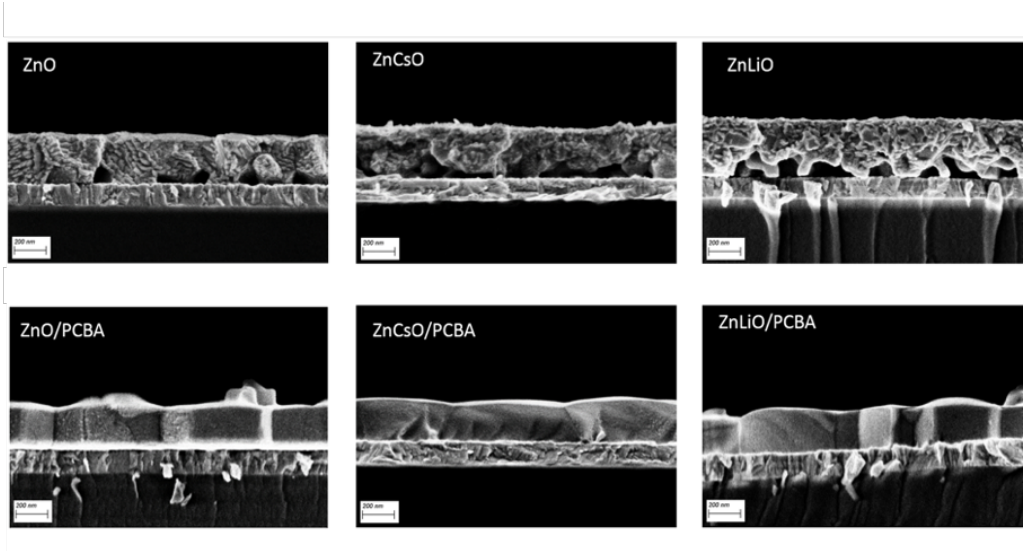

Figure 4.5: SEM cross section images of perovskite films on bare and PCBA modified *ZnO*, *ZnCsO* and *ZnLiO*.

pictured in Figure 4.4 and side view pictured in Figure 4.5. In Figure 4.4, the perovskite on plain *ZnO* exhibits polycrystalline grains with rough surface and multilayer protuberances, while the perovskite films display a smaller grain with a smoother surface on the plain *ZnCsO* and *ZnLiO*. Interestingly, though a pin hole free perovskite film can be seen on bare *ZnO*, *ZnCsO* and *ZnLiO* from SEM top view, the cross-section figures (Figure 4.5) show that the perovskite layer consists of irregular small grains with large gaps near the interface in both doped and undoped *ZnO* cases. The appearance of large gaps emphasize that a severe perovskite decomposition happens at the *ZnO* surface, and dopants such as *Cs* or *Li* do not prohibit this process.

However, by modifying the metal oxide surface with a PCBA SAM, a pronounced effect on the perovskite layer structure occurs with both doped and undoped *ZnO*. The perovskite grains become uniform with a size of approximately 500 nm, and even protrude throughout the entire film for a highly improved interfacial contact. This guarantees that the charge carriers can be transported through an entire single grain, which is especially beneficial for the photovoltaic devices.[151, 152] Additionally, in previous reports, a fullerene-deviation PCBM modification layer (about 10nm to 50nm) was used on top of the ZnO layer to minimize the perovskite

layer decomposition and improve the film formation. [135, 153] However, as DMF which is the most commonly used solvent for perovskite fabrication can partly wash away the PCBM, the applicability of this approach is unfortunately limited.[154, 155] On the contrary, PCBA is not soluble in DMF showing a sustainable ability towards DMF.[156] Our results illustrate that introducing a single monolayer of fullerene via a simple one-step deposition routine, it is sufficient to overcome the perovskite decomposition and achieve an enhanced perovskite crystallinity on ZnO surface.

4.4 Photovoltaic Performance

After characterizing the perovskite microstructure on ZnO, $ZnLiO$, $ZnCsO$ with and without PCBA modification layers, the performance of photovoltaic devices made from these ETLs was investigated on n-i-p structure solar cells. The devices were completed by depositing Spiro-OMeTAD on perovskite films, followed by thermal evaporation of an 80 nm thick silver anode. Figure 4.6 shows the histograms of the photovoltaic performance parameters obtained from a total 414 different solar cells, where each type of ETLs has 60-80 representative solar cells.

Figure 4.6(a) shows that the open circuit voltage (V_{oc}) has no change with the introduction of dopants. This is in agreement with the UPS measurements presented in Figure 4.3, which shows that doping does not alter the energetic structure of the metal oxide. While, the V_{oc} also shows only a slight increase upon modification with PCBA. This small increase is in consistent with results reported for PCBA modified TiO_2 ETLs, and can be explained by a suppression of non-radiative recombination. This suppression is due to either a PCBA-induced enhancement of the electron quasi-Fermi level or PCBA serving as a blocking layer to block minority charges. [156, 157]

Unlike the V_{oc}, the short circuit current (J_{sc}) of $ZnCsO$ and $ZnLiO$ show a 20%-30% increase comparing to that of ZnO. The J_{sc} arises from an average of 10.4 mA/cm^2 in ZnO to 11.8 mA/cm^2 in $ZnCsO$, and to 12.6 mA/cm^2 in $ZnLiO$. Accompanied by a slight enhancement of the average fill factor (FF), the overall power conversion efficiency (PCE) improves from 4.7% of undoped devices to 5.6%-5.7% of doped devices, which is comparable to previous reports that also employ ZnO as ETL.[129] Con-

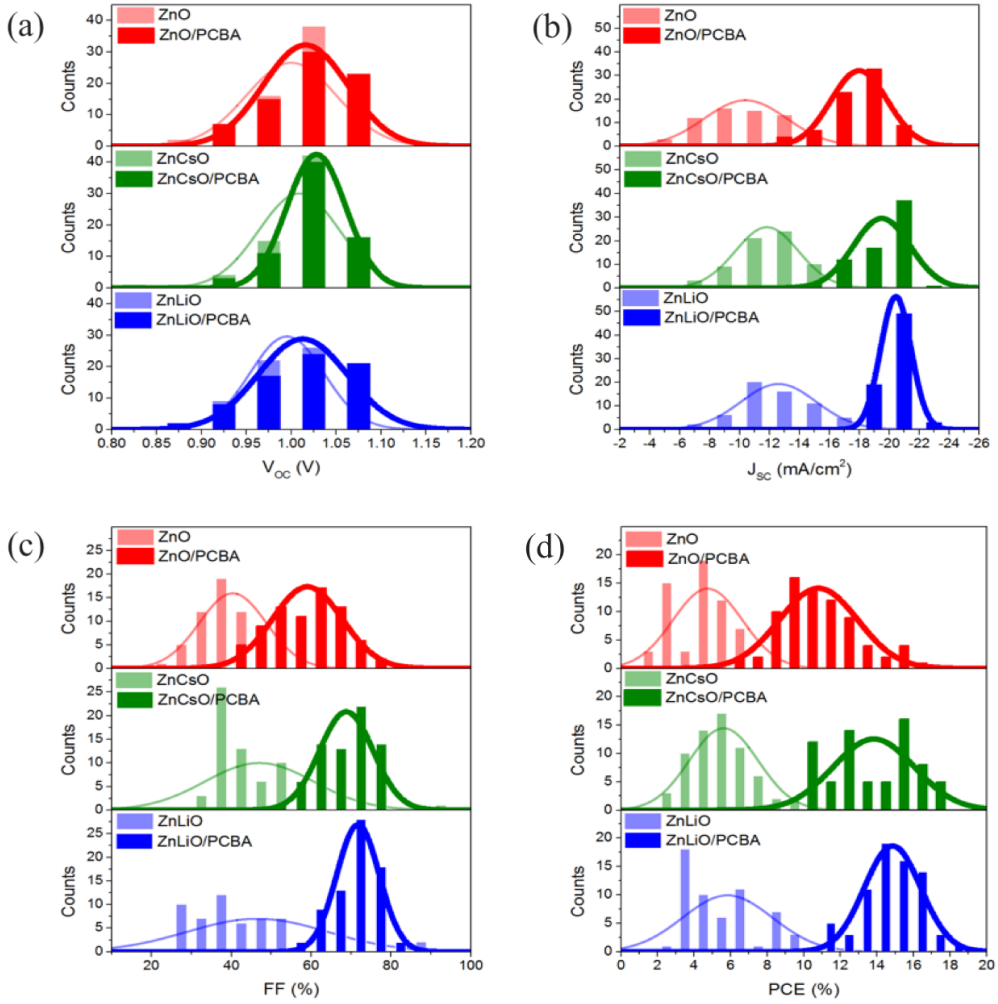

Figure 4.6: Histograms of photovoltaic performance parameters: (a) V_{oc}, (b) J_{sc}, (c) FF and (d) PCE for a total of 414 bare and PCBA modified photovoltaic devices.

sidering the perovskite structure imaged by SEM (Figure 4.5), this poor performance of cells without a PCBA monolayer is heavily associates with the gaps at the perovskite/metal oxide interface, which causes inefficient charge extraction that lowers both the J_{sc} and FF. Moreover, the spread of J_{sc}, FF and PCE is quite large, which can be explained by the different degrees of perovskite bad interfacial contact on different areas of the metal oxide.[158, 159]

When a PCBA SAM is introduced on top of the metal oxide surface, the photovoltaic performance improves drastically. For example, in the case of ZnO, a nearly 75% increase in the average J_{sc} and an improvement in FF

from 40.3% to 56.8% raise an enhancement of the average PCE to 10.2% which is 220% higher than that of unmodified ZnO. The improvements of the device performance are even more evident on PCBA modified Cs or Li doped ZnO. Similarly to the unmodified devices, an approximate 20% increase of the average J_{sc} and FF result in a nearly 40% enhancement of the average PCE to 13.82% and 14.85% for modified $ZnCsO$ and $ZnLiO$,respectively. The best PCE of 18.02% was achieved by PCBA modified $ZnLiO$ devices, which is over double the maximum PCE in bare ZnO. Additionally, the statistical distribution of photovoltaic performance parameters narrows with the addition of PCBA, suggesting a more reproducible formation of perovskite film on PCBA modified metal oxide layers.

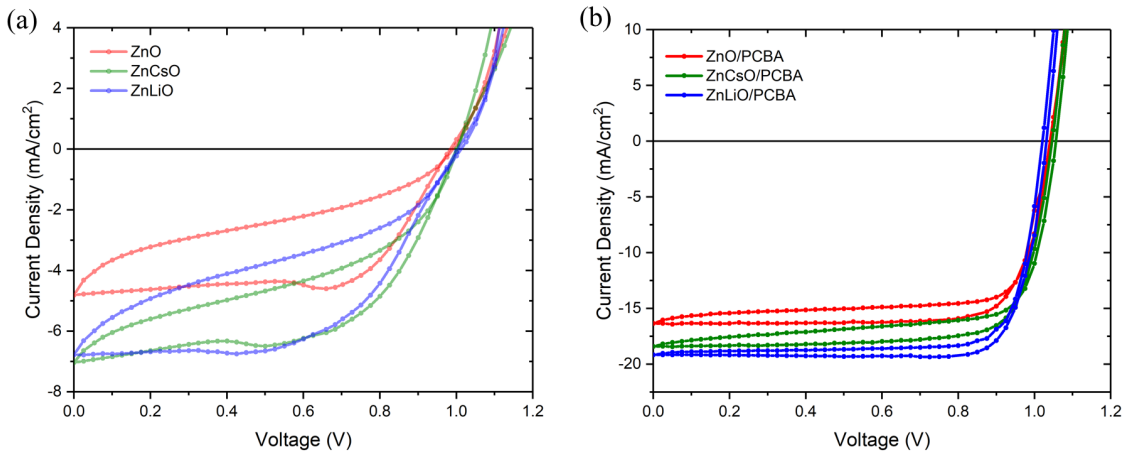

Figure 4.7: $J-V$ curves in reverse (V_{oc} to J_{sc}) and forward (J_{sc} to V_{oc}) scans of representative devices with (a) bare and (b) PCBA modified doped and undoped ZnO layers. The scan rate for all curves was 25 mV/s.

The $J-V$ curves of devices with and without PCBA are presented in Figure 4.7, with both the reverse and forward scans depicted. The photovoltaic parameters are shown in Table B.2 and a hysteresis index defined as $\frac{PCE_{reversescan}}{PCE_{forwardscan}}$ is also compared in Figure A.3. In addition to the improvement of photovoltaic parameters, PCBA modified devices also show a significant suppression of hysteresis, in agreement with the previous observations of devices using fullerene derivatives.[160, 161] Although device hysteresis seems unaffected by the incorporation of dopants, the series resistance of devices is markedly reduced upon the addition of either dopants

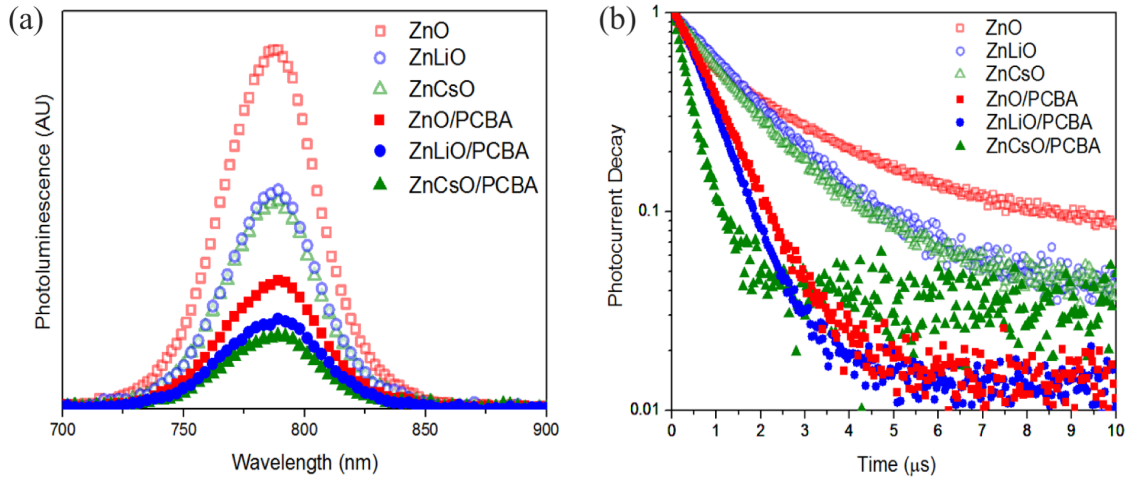

Figure 4.8: (a) Photoluminescence of perovskite and (b) transient photocurrent measurements on bare and PCBA modified ZnO, $ZnCsO$, $ZnLiO$.

or PCBA.(Table B.2) The stability of these devices, on the other hand, seems to be improved upon modification with a PCBA monolayer.
To investigate the effect of PCBA on device stability, unencapsulated Li doped devices with and without PCBA SAM were studied. Between measurements, the devices were stored in the dark at room temperature in air at ~30% relative humidity. As time passes, the PCE of unmodified devices show a gradual decrease to ~60% of its initial value after two weeks, while PCBA modified devices have stable performance with only minor variations. (Figure A.4) Since the PCBA SAM eliminates gaps in the interface of perovskite/ETL and blocks the ingress of water molecules from the ETL side, we conclude that the improved perovskite structure on PCBA modified metal oxide induces an improved performance with enhanced stability, even in a humid environment.

4.5 Discussions

In previous sections we have characterized the influence of the engineered ZnO on the properties of the perovskite microstructure and the resulting changes in photovoltaic performance. In this section we will discuss the origins of the device performance improvement.
As shown in Figure 4.6, the most improved parameter in terms of photovoltaic performance is the J_{sc}. Since the J_{sc} is dependent on the charge

extraction ability of the transport layers, we examined the charge extraction efficiency of the engineered ZnO via the photoluminescence measurements. The effects of different electron extraction layers on the photoluminescence of the perovskite layer are compared in Figure 4.8(a). The photoluminescence quantum efficiency (PLQE) for each case is summarized in Table B.3. Notably, the peak intensity of PL and the value of PLQE are reduced by incorporating dopants in ZnO, and they are further suppressed by a PCBA modification. These indicate that the electron extraction is improved by engineered ZnO, especially when doping is combined with an interfacial treatment. Transient photocurrent measurements can also be used to characterize the charge extraction. (Figure 4.8(b)) The transient photocurrent as well as the transit time is dramatically reduced for PCBA modified devices and even a shorter transit time (Table B.3) appears in PCBA modified $ZnCsO$ and $ZnLiO$ layers, in agreement with improved electron extraction. Both PL and transient photocurrent results suggest that not only the surface properties of the ETL (affected by PCBA) but also the bulk properties (affected by doping) impact on the extraction efficiency within the device.

In Section 4.2, we have shown that Cs and Li dopants do not influence on the absorption, film microstructure and the energy levels of ZnO. In Section 4.3, it has been demonstrated that the surface properties of both doped and undoped PCBA modified metal oxide layers are very similar. Therefore, we hypothesize that the improvement of charge extraction and the enhancement of overall device performance in PCBA modified $ZnLiO$ and $ZnCsO$ cases are related to changes in the bulk properties of ZnO.

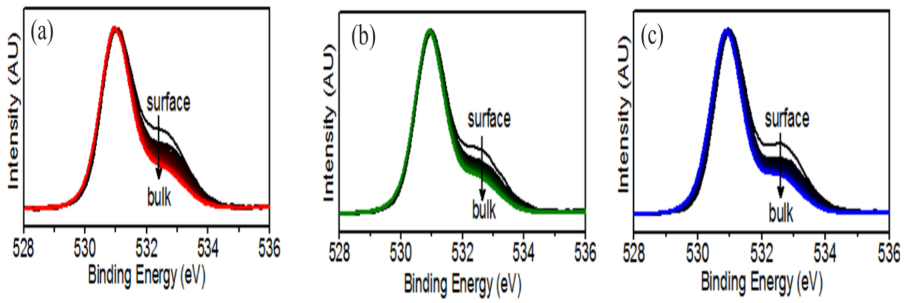

Figure 4.9: XPS $O1s$ spectra of (a) ZnO (b) $ZnCsO$ and (c) $ZnLiO$ with etching from surface to the bulk.

To investigate the bulk properties of the metal oxide ETLs, we performed the XPS depth profiling on doped and undoped ZnO to track the changes in the $Zn2p$ and $O1s$ spectra. Consist with previous measurements, there are two species in $Zn2p$ and $O1s$ spectra. The evolution of $O1s$ spectra in ZnO, $ZnCsO$ and $ZnLiO$ are illustrated in Figure 4.9(a), 4.9(b) and 4.9(c), respectively. The decrease in peak intensity with etching time of the $O-H$ species suggests that more hydroxyl groups are present at the surface than in the bulk, which is a result of the hydrophilic nature of ZnO. Since the presence of $O-H$ groups has been previously related to the trapping of electrons,[145, 162] the lower $O-H$ species percentage in doped ZnO both at the surface and in the bulk (Figure 4.10(a)) would suggest a decreased trap density at both the surface and within the bulk of the $ZnCsO$ and $ZnLiO$ compared to ZnO.

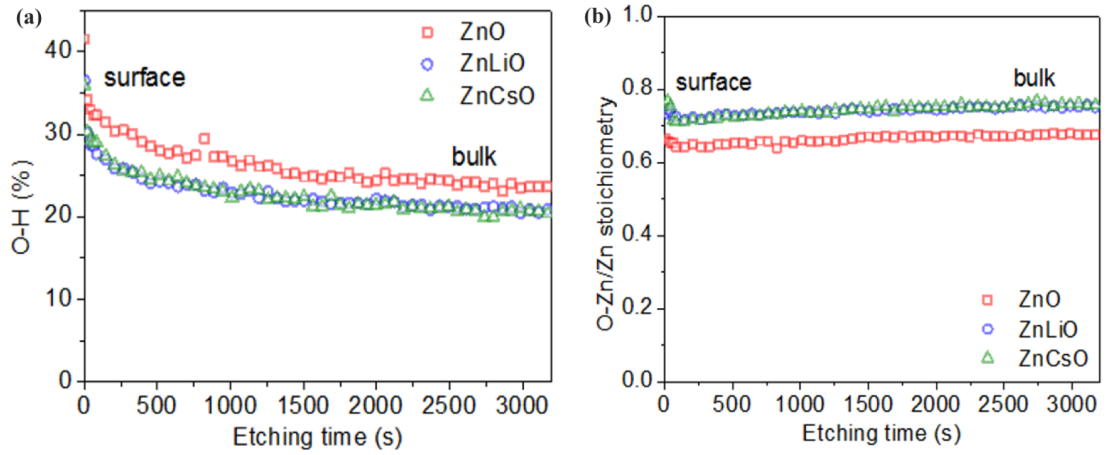

Figure 4.10: (a) The percentage of $O-H$ oxygen over total oxygen and (b) oxide stoichiometry represented by $O-Zn/Zn$ as a function of etching time.

The ratio of $O-Zn/Zn$ over etching time is shown in Figure 4.10(b), which can be used to estimate the material stoichiometry. Due to a large density of oxygen vacancies, the stoichiometry of $O-Zn/Zn$ is frequently observed as smaller than one in solution processed ZnO films.[163] Upon doping with Cs and Li, the $O-Zn/Zn$ stoichiometry in the ZnO film increases by $\sim$15%, indicating an overall improved film quality. This is in agreement with a previous report on the use of similar dopants in ZnO as an extraction layer in organic photovoltaic devices.[164, 165] Excluding

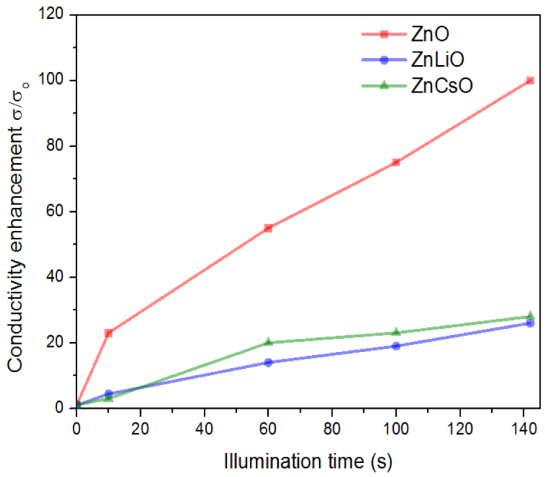

Figure 4.11: Metal oxide conductivity over time under 1 sun illumination.

the specific doping mechanism (which is out of the scope of this work), our results speculate that Cs and Li doping reduce the oxygen vacancies in the bulk of ZnO, inducing an increased conductivity of the metal oxide and a correspondingly faster charge extraction.
In addition to the decrease in the $O-H$ percentage and the increase of $O-Zn/Zn$ stoichiometry, the boost in conductivity upon illumination with UV-light also can be used as an indication for the changes in the density of traps within ZnO. Owing to the structural defects, a variety of sub-bandgap states that can trap charges are present in solution processed ZnO.[166] Considering UV light can increase the film conductivity by filling these trap states,[167, 168] a relative increase in conductivity under UV illumination can be related to the total density of traps. A significantly larger rise in the conductivity of ZnO versus that of $ZnCsO$ and $ZnLiO$ is depicted in Figure 4.11, further confirming that doped layers have a lower density of traps than the undoped ones.

4.6 Summary

In this chapter, we demonstrate that a PCBA self-assembled monolayer effectively passivate ZnO surface defects by breaking the bonds with hydroxyl groups, and that the presence of Li or Cs dopants also reduce ZnO bulk traps. As a result, a significant improvement in the performance of perovskite solar cells with ZnO ETLs can be achieved by using a com-

bination of doping and the inclusion of an SAM. Both doping and SAM modification can be easily performed in solution at low processing temperatures. We have demonstrated that ZnO can serve as an efficient electron extraction layer in perovskite photovoltaic devices after engineering its bulk and surface properties. Our approach overcomes the instability of perovskite on ZnO surfaces and makes ZnO as a competitive alternative to TiO_2, especially in applications that require low temperatures, such as printed and flexible perovskite photovoltaics.

Chapter 5

π-Extended Phosphoniumfluorene Electrolytes as Hole-Blocking Layers in Inverted-Architecture Perovskite Solar Cells

In the previous chapter, the electron transport layer (ETL)/perovskite interface was investigated in the standard, n-i-p photovoltaic structure. In this chapter we will focus on the ETL/cathode interface in the inverted, p-i-n photovoltaic structure. Eight π-extended phosphoniumfluorene electrolytes (π-PFEs) are introduced as hole-blocking layers (HBLs) in inverted architecture perovskite solar cells to engineer the interface between the ETL and metal contact for the device structure of ITO/m-PEDOT:PSS/$MAPbI_3$/HBL/Ag. The deep-lying highest occupied molecular orbital (HOMO) energy level of the π-PFEs effectively blocks holes and decreases the recombination at the contact. By experimentally studying four of the π-PFEs in detail, we find that the incorporation of the electrolytes introduces a dipole moment at the PCBM/Ag interface, resulting in a significant enhancement of the built-in potential of the device. All discussions in this chapter are based on our publication in *"Enhancing the Open-Circuit Voltage of Perovskite Solar Cells by up to 120 mV Using π-Extended Phophoniumfluorene Electrolytes as Hole Blocking Layers"* Q. An, Q. Sun, A. Weu, D. Becker-Koch, F. Paulus, S. Arndt, F. Stuck, A. S. K. Hashmi, N. Tessler, Y. Vaynzof, Adv. Energy Mater. 2019,9,1901257.

5.1 Introduction

In perovskite solar cell p-i-n structures, PCBM and other fullerenes are the most widely used ETLs due to their ability to efficiently transport and extract electrons from the perovskite active layer.[169] It has also been shown that PCBM passivates the trap states in the perovskite and eliminate photocurrent hysteresis, which further motivates researchers to use PCBM in perovskite solar cells.[160, 170] However, its low ionization potential relative to the perovskite causes a significant amount of charge recombination, resulting in low fill factor and power conversion efficiency.[72] Moreover, the energetic mismatch between the lowest unoccupied molecular orbitals (LUMO) of PCBM and the work function of cathode leads to a further reduction of the photovoltaic performance.
lt To block holes and remedy the energetic mismatch, researchers have focused on modifying the PCBM/cathode interface with a range of materials. For example, materials such as N,N'-bis(1-n-hexylpyridin-1-ium-4-ylmethyl)-1,4,5,8-naphthalenetetracarboxydiimide (PN6),[171] ethoxylated polyethylenimine (PEIE),[172] (11-mecaptoundecyl)-trimethylammonium bromide (MUTAB),[173] amino-functionalized polymer PN4N,[174] metal acetylacetonate[114] and Rhodamine[175] were reported to modify the cathode work function, resulting in good electrons extractions and a large improvement of the device efficiency. Interlayers with a deep LUMO such as ZnO nanoparticles,[176] TiO_x,[177] bathocuproine (BCP)[178] and bispyridinium salt FPyBr[179] were utilized to supplement the low ionization potential of PCBM, aiming to block holes and suppress charge losses. Among these materials, most of the improvements in device performance originate from the fill factor enhancement, especially for devices that utilize PEDOT:PSS as a HTL. In these devices, the open circuit voltage (V_{oc}) improves when compared to the reference device which is without a HBL; however, the V_{oc} still remains in the range of 0.9V to 1V,[45, 172–174, 176] lagging behind a deep HOMO HTL such as NiO_x, PTAA or poly-TPD.[77, 79, 103, 180]
In this chapter, 8 newly synthesized π-extended phosphoniumfluorene electrolytes (π-PFEs) by Dr. Sebastian Arndt are applied as HBLs in p-i-n structure perovskite solar cells with doped PEDOT:PSS as HTL

and PCBM as ETL. The high ionization potential of the synthesized electrolytes greatly prevents holes from recombining with the electrons in cathode. Most importantly, by studying four out of eight π-PFEs in detail, we find that π-PFEs not only reduce the charge recombination losses, but also form a dipole at the PCBM/cathode interface. This dipole significantly increases the built-in potential of the photovoltaic devices and leads to an enhanced V_{oc} up to 1.07 V, surpassing devices with the commonly used BCP (~0.95 V).

5.2 Photovoltaic Performance of Perovskite Solar Cells with π-PFE HBLs

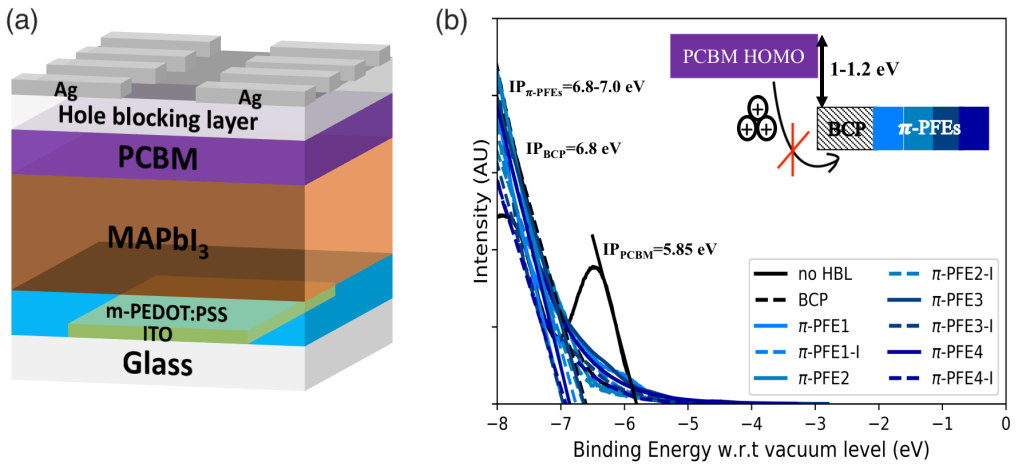

Figure 5.1: (a) Schematic illustration of photovoltaic device structure. (b) Ultraviolet photoemission spectroscopy measurements of the ionization potential of BCP and 8 different kinds of π-PFEs with PCBM spectrum as reference.

The p-i-n photovoltaic device structure used in this chapter is schematically illustrated in Figure 5.1(a). The devices with no HBLs, commonly used BCP HBLs, and newly synthesized π-PFEs HBLs were fabricated with all remaining layers unchanged. The chemical structure of π-PFEs was introduced in Section 3.1.2 Figure 3.3(b). Here, π-PFE1-4 vary only by slight changes in the side-group (the R-group) of the anion, while π-PFE1-4-I has the same side-group with π-PFE1-4 but with an additional iodine at the X-group. A deep HOMO level is a prerequisite

for a HBL; therefore to identify whether π-PFEs can serve as HBLs, the ultraviolet photoemission spectroscopy (UPS) was employed to measure their ionization potential. The sample structure used for this measurement was ITO/PCBM/π-PFEs, and the ionization potential of PCBM and PCBM/BCP were also measured as references. As shown in Figure 5.1(b), both BCP and π-PFEs exhibit a higher ionization potential (6.8-7 eV) than PCBM (5.85 eV), leading to a larger hole injection barrier than the underlying PCBM. This barrier indicates that both BCP and π-PFEs can effectively block holes which traverse through the PCBM from reaching the cathode and recombining with free electrons, while this can not be expected in the case of no HBLs due to low ionization potential of PCBM. When incorporating each of the eight π-PFEs into photovoltaic devices, we find that the devices with HBLs have a higher average fill factor (FF) than bare PCBM, demonstrating their ability to block holes. However, the lifetime of devices employing π-PFE1-4-I as the HBL is much shorter than that of sample with π-PFE1-4. In the short time-span of two continuous measurements, the edge of pixels on devices with π-PFEs-I HBLs start turning to yellow (Figure A.5). This color change is also accompanied by a drop in all the photovoltaic parameters, as shown in Figure A.6. The fast degradation of devices with π-PFEs-I HBLs can be explained by the oxidation of the silver electrode to silver iodide due to a reaction with the iodine in π-PFEs-I HBLs,[181] which shortens the device lifetime and prevents further investigation. Thus, we will only discuss π-PFE1-4 in the following study.

Because of the similar ionization potential of π-PFEs and BCP, it would be expected that incorporating π-PFEs and BCP into the solar cells will have a similar effect on the photovoltaic performance. However, the photovoltaic performance characterization reveals this is not the truth. Figure 5.2(a) shows the current density-voltage ($J-V$) curves of photovoltaic devices measured in the dark. Comparing the no-HBL device to the π-PFE4 device, the ”knee” positions of the diode characterization are significantly shifted to a higher voltage (from 0.6 V to 0.85 V). Such a shift is probably caused by an enhanced built-in potential, and may lead to an increase in device V_{oc} under illumination. As expected, the current density-voltage curves acquired under simulated AM 1.5G sunlight with

100 mW/cm^2 of the best devices with and without HBLs (Figure 5.2(b)) exhibit obvious differences in the photovoltaic performance, especially in the V_{oc} and FF. The photovoltaic parameters of these curves including both reverse and forward scans are summarized in Table 5.1.

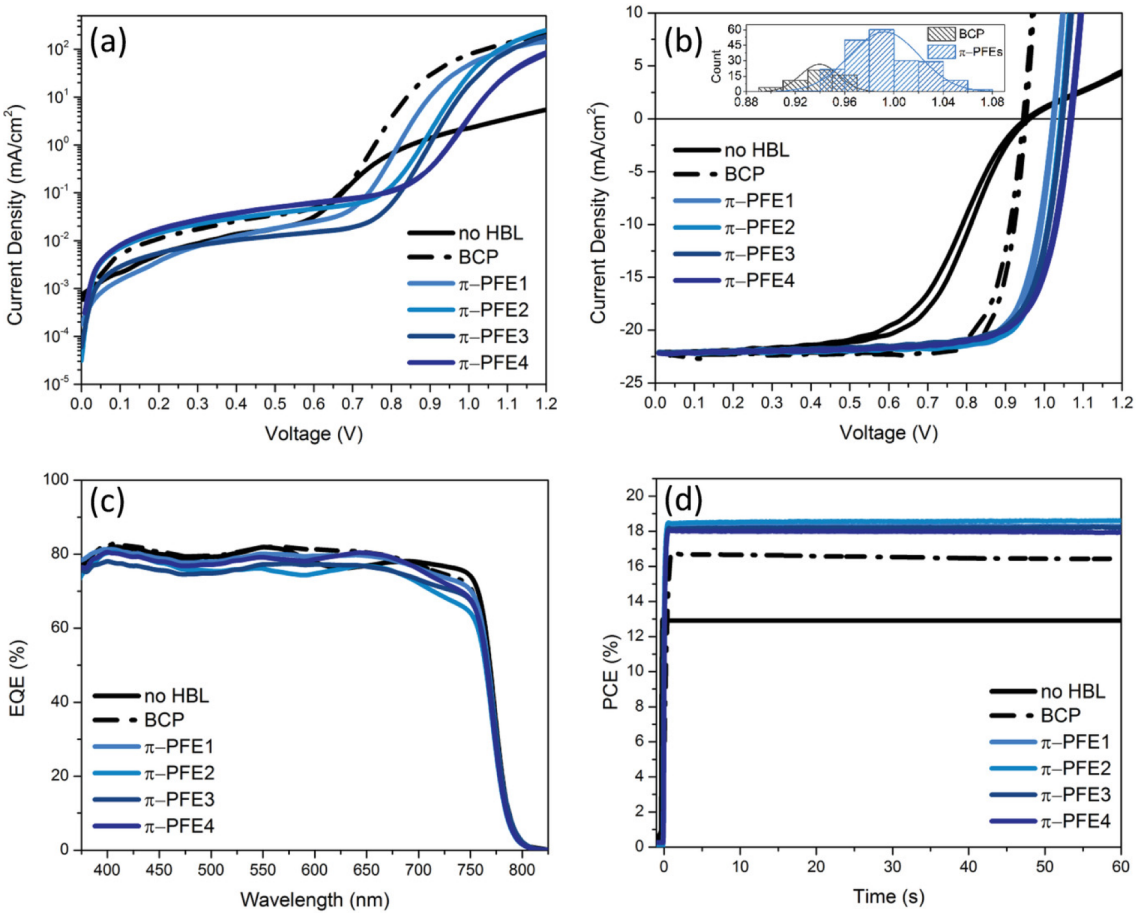

Figure 5.2: The current-voltage curves measured (a) in the dark and (b) under AM 1.5G illumination with corresponding (c) external quantum efficiency (EQE) spectra and (d) time dependence of the maximum power output efficiency of devices with bare PCBM (no HBL), BCP as HBL and π-PFEs as HBL. The inset in panel (b) is a histogram of the V_{oc} measured on 258 devices with either a no HBL and a BCP or π-PFE1-4 HBLs, the complete statistics of the photovoltaic parameters for these devices can be found in Figure A.7

The short circuit current (J_{sc}) of the devices remains unaffected by the introduction of a HBL, with a very similar results of 22 mA/cm^2 between all samples. On the other hand, the shape of the $J-V$ curve, which corre-

	RS V_{oc} (V)	FS V_{oc} (V)	RS J_{sc} (mA/cm^2)	FS J_{sc} (mA/cm^2)	RS FF (%)	FS FF (%)	RS PCE (%)	FS PCE (%)	R_s (Ω/cm^2)
PCBM	0.96	0.95	-22.22	-22.22	60.1	56.84	12.85	12.03	33.26
BCP	0.95	0.93	-22.40	-22.40	81.39	78.32	17.38	16.33	2.90
π-PFE1	1.03	1.02	-22.19	-22.19	80.55	78.23	18.34	17.74	2.33
π-PFE2	1.04	1.04	-22.11	-22.11	79.90	78.25	18.46	18.03	2.22
π-PFE3	1.05	1.05	-22.05	-22.05	78.09	76.90	18.05	17.72	2.20
π-PFE4	1.07	1.07	-22.16	-22.16	75.95	76.07	18.03	17.96	2.40

Table 5.1: Photovoltaic parameters of the $J-V$ curves shown in Figure 5.2. RS and FS represent the scanning direction from V_{oc} to J_{sc} and from J_{sc} to V_{oc}, respectively. R_s is the series resistance of the devices.

sponds to the FF, is strongly affected by incorporating a HBL. The $J-V$ curve of bare PCBM (no HBL) presents an S-shape, which originates from a high series resistance and a poor hole blocking, in agreement with the previous reports.[172, 182] As a result, this device has a low FF of 60.1% and a moderate V_{oc} of 0.96 V, yielding a PCE of only 12.85%. Introducing either BCP or π-PFEs into the devices eliminates the S-shape and effectively increase the FF by 25%-35% compared to no-HBL device. This improved FF is a consequence of the high ionization potential of the HBL, as the deep-lying HOMO level of π-PFEs and BCP effectually prevents the electron-hole recombination between PCBM and cathode.

To compare the devices with different HBLs, we first ensure that the comparison is performed with the best possible devices of BCP. To accomplish this, we optimized the thickness of the BCP layer. As illustrated in Figure A.8, the optimal thickness of the BCP layer is 5 nm, in agreement with the previous work by Chen et al.[183] Thus, all the BCP devices use this optimal layer thickness in this work. Among the devices with BCP and π-PFEs, the commonly used BCP has little to no effect on the V_{oc}, while a significant enhancement of V_{oc} as much as 120 mV presents in devices with π-PFEs.The overall improvements in FF and V_{oc} lead to a maximum power conversion efficiency (PCE) of 18.46% for a device with a π-PFE

HBL, surpassing that of the BCP (17.38%). Besides, in π-PFE1-4 devices, a similar average photovoltaic performance in a complete statistic of 258 devices (Figure A.7) suggests that there is no significant difference in the photovoltaic behavior among the choice of the side chain (1-4).
Figure 5.2(c) shows the external quantum efficiency (EQE) spectra of devices with and without HBLs. The similar EQE spectra are in agreement with the measured J_{sc} and indicate that the extraction of charge carrier remains largely unaffected at the PCBM/Ag interface with inserting π-PFE1-4 or BCP. The time dependence of the maximum power output efficiency of corresponding devices is illustrated in Figure 5.2(d). All the devices exhibit a stable output efficiency within 60s indicates a low hysteresis, which is common for devices with a PCBM electron extraction layer.[160]
It is interesting that by inserting a 10 nm thick π-PFE1-4 layer between PCBM/Ag interface not only prohibit the electron-hole recombination but also improve the V_{oc} of devices. Therefore, in the following discussion we will focus on the origin of the V_{oc} enhancement.

5.3 Non-radiative Recombination in Perovskite Solar Cells with π-PFE HBLs

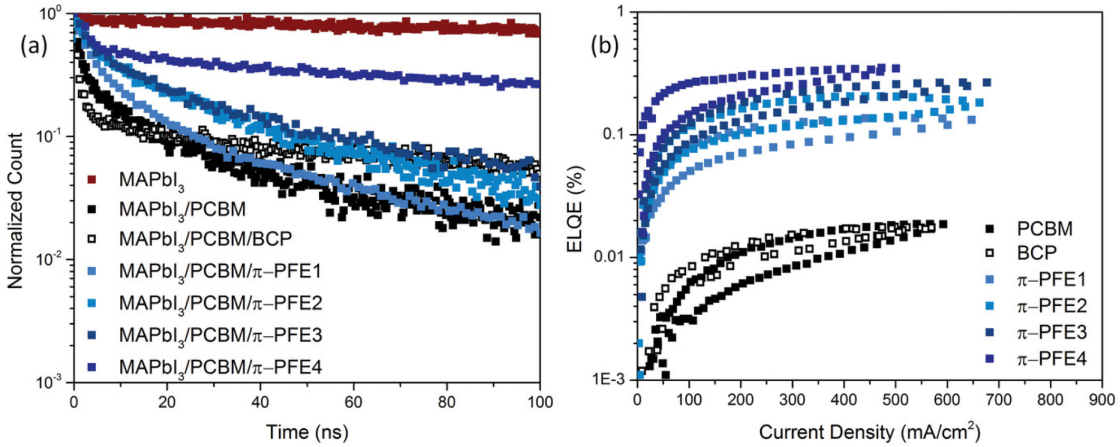

Figure 5.3: (a) Normalized time correlated single photon counting (TCSPC) photon decay for films of bare perovskite, perovskite/PCBM and perovskite/PCBM/HBLs on glass substrates. (b) Electroluminescence quantum efficiency of devices with and without different HBLs.

In Section 2.3, we have already discussed that the non-radiative recombination is one of the key factor to determine the V_{oc}. Since it is impossible to directly characterize the non-radiative recombination, we characterized the π-PFEs effects on the radiative recombination of generated charge-carriers. As shown in Figure 5.3(a), time correlated single photon counting (TCSPC) were collected on a pure $MAPbI_3$ film, a $MAPbI_3$/PCBM film as well as a $MAPbI_3$/BCP film and $MAPbI_3$/π-PFE1-4 films. The $MAPbI_3$ only reference sample exhibits an almost mono-exponential decay with a lifetime as long as 552 ns. A faster photon decay with a short lifetime of 1.23 ns appears on the sample of PCBM coated $MAPbI_3$ film, which is a result of an efficient electron extraction by PCBM. Upon coating BCP on $MAPbI_3$/PCBM films, further electron quenching with an even shorter fluorescence lifetime of 0.8 ns can be observed. On the contrary, substituting BCP by π-PFEs slows down the photon decay and slightly increases the lifetime to $\approx$3 ns. As non-radiative recombination eliminates photons, this increase indicates that by using π-PFEs instead of BCP suppresses non-radiative recombination processes, corresponding to an increase of the device V_{oc}. Besides, to demonstrate that a reduction of non-radiative recombination also happens in device with π-PFEs, we characterized the electroluminescence of the devices. Figure 5.3(b) presents the electroluminescence quantum efficiencies (ELQE) as a function of current density for perovskite solar cells with and without different HBLs. The ELQE of the reference PCBM only device and the device with BCP is very similar, while that of device with π-PFEs is increased almost by one order of magnitude. This improvement in ELQE greatly illustrates that the radiative recombination of perovskite solar cells is significantly enhanced by incorporation of π-PFEs, in other word, π-PFEs reduce the non-radiative recombination in the devices. As expected from Rau's reciprocity relation,[184] the enhancement in ELQE is also in agreement with the observed increase in the V_{oc} of the devices.

To investigate the charge recombination processes in the devices, we performed the transient photovoltage (TPV) and light intensity dependent V_{oc} measurements. In the TPV measurement (Figure 5.4(a)), devices with π-PFEs exhibit a longer charge carrier recombination lifetime than those with either bare PCBM or BCP, suggesting that incorporating π-PFEs into de-

vices can efficiently suppress the charge recombination. In the light intensity dependent V_{oc} measurement (Figure 5.4(b)), the slopes of devices with bare PCBM, BCP and π-PFEs are calculated as 1.35, 1.34 and 1.23±0.04 k_BT/q, respectively. This means that though trap-assisted recombination presents in all the devices, devices with π-PFEs have an overall lowest trap-assisted recombination.

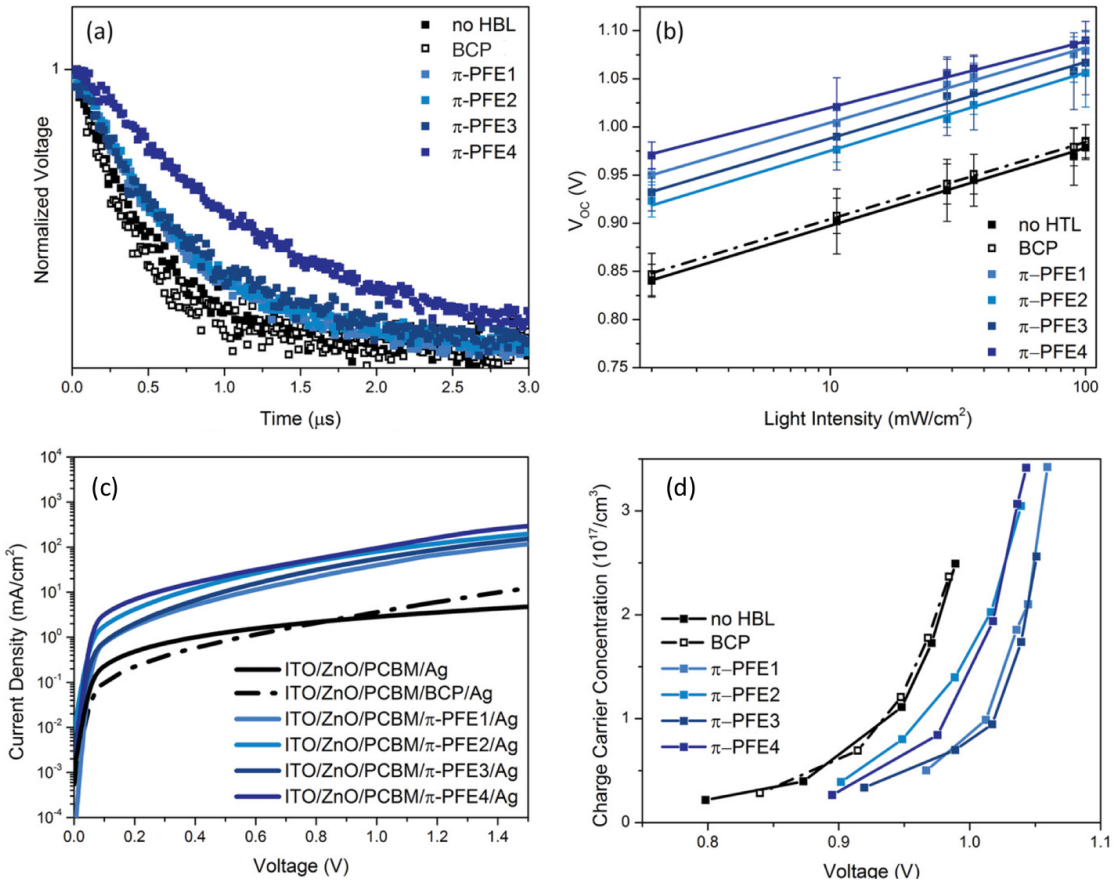

Figure 5.4: (a) Transient photovoltage measurements, (b) V_{oc} dependence upon different light intensity measurements and (c) Charge density generated measurements, measuring by transient photovoltage and transient photocurrent of perovskite photovoltaic with and without the HBLs. (d) J-V curves of unipolar electron only devices.

So far we have shown that the non-radiative recombination has been suppressed by incorporating π-PFEs in photovoltaic devices. As the recombination pathways at the perovskite/PCBM interface remain unchanged, the reduction of the trap-assisted recombination must be associated with the PCBM/π-PFEs/Ag part. It has been demonstrated that a higher V_{oc} can

be achieved by enhancing the order of the PCBM.[115] Therefore we employed the AFM, XRD and PDS measurements on PCBM layer with and without π-PFEs to investigate the crystalline and energetic order of the films. As shown in Figure A.9, Figure A.10 and Figure A.11, there are no significant differences within the samples in all measurements, indicating that the PCBM film remain unaffected by depositing the π-PFEs on top.
In addition, conductivity measurements were performed on unipolar diodes with the structure ITO/ZnO/PCBM/HBL/Ag.(Figure 5.4(c)) The overall current of devices with π-PFEs has a minor difference as compared to that of devices with BCP, resulting in a fivefold increase of electron mobility on average.(Table B.4) It has been reported that the evaporated metal can extensively penetrate through the PCBM into the bulk of the active layer.[185] Similar to PCBM, BCP-metal complex can be formed upon the evaporation of the cathode, suggesting that Ag atoms are also able to penetrate through thin BCP layers.[186] However, BCP must be kept very thin (~5 nm) to achieve optimum device performance in perovskite solar cells both in our case and others. Thus, the slight enhancement of electron mobility by π-PFEs may associate with the shield of evaporated Ag atoms, as the π-PFEs (~10 nm) prevent the penetration of Ag atoms to affect the trap density of PCBM. Moreover, an alternative explanation can be addressed to an n-doping of PCBM by the anion of π-PFEs, which induces efficient conductive pathways for electron transport.[179] We note that an average of fivefold enhancement in electron mobility could correspond to a reduction in the energetic disorder of only 0.5 k_BT (12.85 meV)[187], much smaller than what we observe in the improvement of V_{oc}.
To further understand the changes induced by π-PFEs, we performed charge extraction (CE) measurements as previously discussed in organic devices.[188] The CE measurement quantifies the density of extractable charges in the device at a given voltage, thus offering information about the available density of state that is needed to produce a given quasi-Fermi level splitting. Comparing the results shown in Figure 5.4(d), the devices with bare PCBM and BCP have lower voltage than that of devices with π-PFEs at the same charge carrier concentration (also means the same quasi-Fermi level splitting). This observation may arise from broadening in the density of states which is reduced by the energetic disorder or a decrease in

the built-in potential. As confirming by conductivity measurements, there is no significant changes in the energetic disorder among the devices, thus the increased voltage originates from the enhancement of the built-in potential across the device.

5.4 Energetic Alignment at the PCBM/π-PFE/Ag Interface

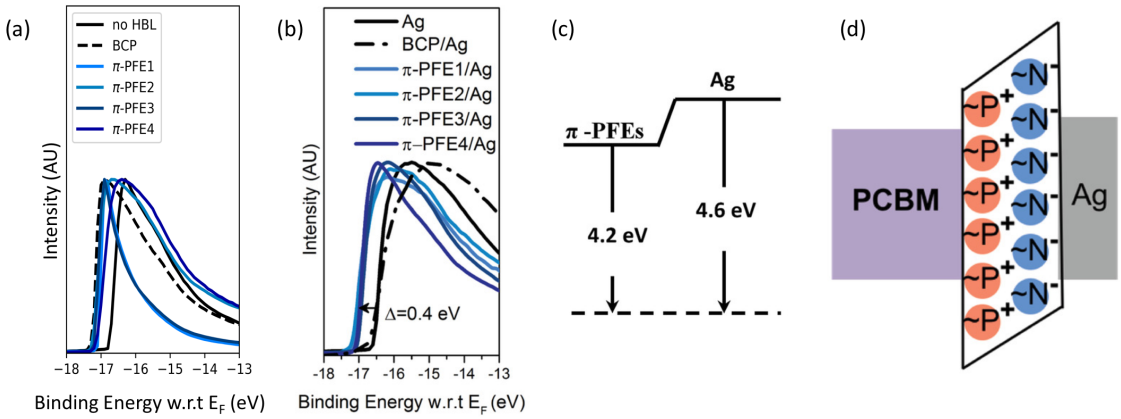

Figure 5.5: (a) UPS spectrum with secondary electron cur-off of PCBM, PCBM/BCP and PCBM/π-PFEs. (b) UPS spectrum with secondary electron cur-off of evaporated Ag, BCP/Ag and π-PFEs/Ag (detached from ITO/PCBM/HBL/Ag devices). (c) Energy level diagram obtained from (b). (d) Schematic illustration of dipole formed by π-PFEs on PCBM/Ag interface.

In the above section, we have found that the built-in potential is enlarged by using π-PFEs. In this section we will reveal the reason for the enhancement. Generally, the built-in potential is produced by the work function (WF) difference between the two electrodes. In organic photovoltaic devices, extensive researches have demonstrated that polyelectrolytes and small molecule electrolytes as interfacial modifiers are able to form electric dipole and shift up vacuum level to enhance the built-in potential at the interface of electrode and transport layer.[189, 190] Thus, it can be expected that the application of π-PFEs as HBL may introduce a electric dipole at the PCBM/Ag interface. To verify this hypothesis, we first employed the ultraviolet photoemission spectroscopy (UPS) on PCBM and PCBM/HBLs layers to evaluate the work function. However, the photoemission onset of

all the HBLs show a 0.3-0.4 eV red shift to the reference PCBM, which corresponds to a downward shift in the vacuum level and discourages the reinforce of built-in potential. (Figure 5.5(a)) Since the evaporated Ag can also interact with the thin HBLs and rearrange the dipole,[191, 192] this may not be the real direction of the dipole in PCBM/Ag interface. We then focus on investigating the interface of π-PFEs/Ag. Similar to the approach used in previous research,[112] UPS measurement was carried out on reference Ag, BCP/Ag and π-PFEs/Ag which were detached from ITO/PCBM/HBLs/Ag. Unlike Figure 5.5a, there is no photoemission onset shift in the case of BCP/Ag comparing to the reference Ag, while the onset moves to a lower binding energy by 0.4 eV in the samples with π-PFEs. (Figure 5.5(b)) This shift suggests that a upward 0.4 eV shift of vacuum level is produced at π-PFEs/Ag interface (Figure 5.5(c)) and illustrates a dipole moment which is related to the TFSI anions (N^-) being located near the Ag side and the cations (P^+) remaining in the proximity of the PCBM surface (Figure 5.5(d)). As a result, this dipole direction will enhance the built-in potential in the whole device and sequentially the V_{oc}. It has also been reported that a surface treatment by methanol may cause an increase in the work function of subsequent layer, thus leading to an enhancement in built-in potential and V_{oc} in organic solar cells.[193] As the solvent for dissolving π-PFEs is methanol, to exclude the influence of the solvent we perform a methanol treatment reference measurement shown in Figure A.12, indicating that methanol is not the case for the enhancement of V_{oc}. Moreover, the π-PFEs were also applied in other higher work function HTLs such as PTAA. As shown in Figure A.13 and Table B.5, the reference device with BCP reach a high V_{oc} ~1.1 V, in agreement with the previous reports.[103] Although the V_{oc} is still improved by incorporating π-PFEs, a less pronounced increase of 30-40 mV than in the case of m-PEDOT:PSS can be found. This is reasonable because of the higher built-in potential of PTAA. Our results that a much stronger effect of π-PFEs is observed on devices with m-PEDOT:PSS than PTAA, also illustrate that it is feasible to strategically use electrolyte HBLs for compensating the unfavorable energetic alignment at the HTL/perovskite interface.

5.5 Numerical Simulations of Perovskite Solar Cells with Different HBLs

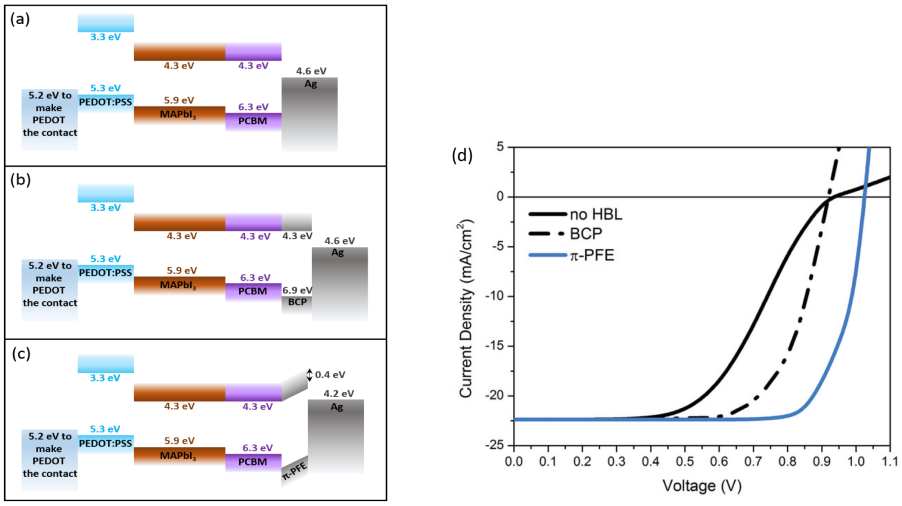

Figure 5.6: Energy level diagrams used to simulate the device (a) with no HBL, (b) with BCP as HBL and (d) with π-PFE as HBL. (d) Simulated stabilized current-voltage curves under one sun for devices with no HBL and with BCP or π-PFE as HBL.

To further confirm that it is the dipole induced by π-PFEs at the interface with Ag attributes to the enhancements in the photovoltaic performance, we implemented numerical simulations (done by Prof. Nir Tessler) of devices with no HBL, BCP and π-PFEs. In brief, the drift diffusion and Poisson equation were solved in self-consistency for electrons, holes and ions. We assume that the ions are mobile and exist only in the perovskite layer, while the electrons and holes freely move in transport and blocking layers. To produce the $J-V$ curves under one sun illumination, we achieve the steady state of both ions and electronic charges at each bias point. This procedure mimic a very slow scanning rate that cancels the small hysteresis, allowing to focus on the shape of the curves.
The material parameters used in the simulation are listed in Table B.6 and the energy levels of each layers in the device are summarized in Figure 5.6(a)-(c). In all simulations, the m-PEDOT:PSS layer was assumed to be a heavily doped semiconductor with the Fermi level at 0.1 eV above the HOMO level. As it is commonly described for devices incorporating with BCP, the LUMO of BCP is assumed to be aligned with that of PCBM to

allow the electron transporting through the BCP layer. To combine all the experimental observations with the model, the position of the cathode is chosen based on the UPS measurement as shown in Figure 5.5(b), which is 4.6 eV for device with no HBL and BCP, while 4.2 eV for device with π-PFE. The electron mobility of the PCBM layer was increased by five-fold in the case of π-PFE according to the average enhancement observed for the π-PFEs electrolyte. (Table B.4) Most importantly, a 0.4 eV dipole across the 10 nm thick π-PFE was also included.
The simulated $J-V$ curves for device with either no HBL or BCP and π-PFE HBL under one sun illumination are shown in Figure 5.6. Similar to the experimental results, a strong S-shape appears in the devices with no HBL. Incorporating BCP in the devices though eliminates the S-shape, it does not lead to an increase in the V_{oc}, in agreement with experimental results. While replacing the BCP with π-PFE, a significant enhancement of 100 mV in the V_{oc} can be achieved, which is excellently consistent with the average enhancement observed for π-PFE1-4 in the experimental part. Moreover, if we only include one of the positive effects of π-PFE such as the enhanced mobility or the interfacial dipole in the simulation, it is impossible to reach a comparable increase in the V_{oc}, suggesting that both effects contribute to the observed improvement.

5.6 Summary

In this chapter, we discussed the incorporation of four different π-PFEs as HBL into p-i-n perovskite solar cells. We demonstrate that the newly synthesized electrolytes not only can block the holes to reduce the recombination losses due to their deep HOMO level, but also significantly enhance the device V_{oc} due to their ability to suppress non-radiative recombination and form a dipole moment between electron extraction layer and cathode. Our results highlight that interfacial engineering of the ETL/contact interface by small molecule electrolytes is a promising route to suppress non-radiative recombination and improve performance in perovskite devices. ETL/contact interfacial engineering can also be used to compensate for non-ideal energetic alignment at the HTL/perovskite interface.

Chapter 6

A Systematic Study of the Bulk Grain Boundaries via Perovskite Photovoltaic Performance

In this chapter, we discuss about the influence of grain boundaries on the perovskite photovoltaic performance. Firstly, we introduce a facile and versatile approach that can control the perovskite grain size. We find that by gradually tuning the amount of HPA additive in the $MAPbI_3$ perovskite precursor solution, the grain size can be enlarged by over one order of magnitude, regardless of the underlying layers or substrates. Further increasing the HPA content leads to the formation of a high quality porous structure, which could be of great interest for application in light-emitting diodes. Secondly, using the above mentioned method we fabricate two types of perovskite solar cells. Type A cells vary the grain size of the perovskite film with the same film thickness by tuning the HPA content in the perovskite precursor solution, and type B cells that have a similar grain size with type A cells but with a thinner film thickness are established by using the optimal HPA amount in different weight ratio perovskite solution. These two type of devices allow us to systematically study the effects of grain boundaries in the perovskite solar cell. Through experimental characterizations and theoretical simulations, we demonstrate that grain boundaries are the sources of deep trap states to militate against radiative recombination.

6.1 Introduction

In device fabrication, high purity perovskite layers with a uniform morphology and no pin-holes have been shown to be particularly important to deliver better photovoltaic performance.[76, 194] It has been reported that the presence of deep energy level defects may greatly harm the photophysical properties of perovskite, resulting in lower solar cell efficiencies.[35, 195] It has also been shown that the microstructure of perovskite layers plays an important role in determining the ion migration properties and photovoltaic device stability.[40, 196–198] Therefore, significant strategies have been devoted to fabricate high electronic quality polycrystalline perovskite films.

One of the most noteworthy approaches is doping alkali cations into perovskite materials, which has been demonstrated to control bulk defects and eliminate hysteresis.[47, 199, 200] Another similar notable approach is an optimization of the deposition procedure and surface modification that can greatly improve the quality of perovskite morphology and reduce the density of trap states.[52, 53, 103, 156] Besides these, a widely used way is to introduce additives into perovskite precursor prior to the layer deposition. The additives are used to improve the perovskite polycrystalline quality, control the perovskite grain size to suppress the non-radiative recombination, and enhance the perovskite solar cell long-term stability. Additives such as hypophosphorous acid (HPA), imidazole sulfonate 4-(1H-imidazol-3-ium-3-yl) butane-1-sulfonate (IMS), ammonium hypophosphite (AHP) and methylammonium chloride (MACl) have been demonstrated to effectively improve the film quality, passivate trap states and modulate morphology of the perovskite layer.[18, 93, 201, 202] Moreover, a significant enhancement in the long-term stability of solar cells has been reported by using 1-butyl-3-methylimidazolium-tetrafluoroborate (BMIMBF4) and 1-butyl-1-methylpiperidinium-tetrafluoroborate ($[BMP]^+[BF4]^-$) as an additive.[203, 204]

In addition to solar cells, controlling the microstructure of perovskite is equally important for perovskite LEDs, as the microstructure of the perovskite active layer greatly contributes to the light outcoupling.[205, 206]

It has been reported that modifying the microstructure of methylammonium lead tribromide ($MAPbBr_3$) LEDs strongly affects all the performance parameters of LED.[207] More recently, a discontinuous submicrometric perovskite structure has been created by introducing amino-acid or amino-functionalized agents as additives into the perovskite precursor solutions, leading to efficient and high-brightness electroluminescence with passivated bulk defects.[208, 209]

As discussed above, perovskite microstructure significantly influences the performance of optoelectronic devices. It is well known that in the polycrystalline perovskite microstructure, grain boundaries exist as high dimensional defects due to the naturally varied orientation of the crystal lattices.[210] However, the precise role of grain boundaries in perovskite photovoltaics is still under debate. Previous studies have suggested that grain boundaries allow effective separation and collection of photo-generated carriers without creating any gap states, and thus are benign.[35, 211] Others have found that grain boundaries are not recombination active but rather dominate the ion migration in the film.[43, 212, 213] One study even shows controversial results where larger grains reduce the recombination but simultaneously lower the V_{oc}.[151] Still more contrasting evidence suggests that grain boundaries are in fact detrimental and act as recombination centers via Shockley-Read-Hall (SRH) recombination mechanisms.[44, 76, 202, 214]

One of the reasons for such inconclusive experimental observations is that some of the results are recorded on perovskite morphologies with uncontrollable grain boundaries in both vertical and horizontal direction, making it hard to pinpoint and separate their effects. Another possible reason is that some of the research objects are chosen to be different size of grains but on the same film, which should have a similar property of grain boundary and is far more special for comparing. Similarly, in numerical simulations about the grain boundaries, previous studies have suggested that recombination at grain boundaries rarely determines the photovoltaic performance of perovskite solar cells,[215, 216] which did not test for different grain size in a systematic model and only implemented grain boundaries in the vertical direction that is the charge transport direction while grain size determines the grain boundaries in the horizontal direction. Therefore, a sys-

tem where the grain boundary is the only controllable parameter in the horizontal direction will easily clarify their behavior.
In this chapter, we first investigate in detail the effect of HPA on the microstructure of perovskite films. We show that tuning the concentration of HPA additive in perovskite precursor is a facile way to control the grain size and porosity of the perovskite films on a wide range of substrates. Secondly, by varying the HPA concentration and the perovskite precursor weight ratio in the precursor solution, we systematically examine the impact of grain boundaries on the performance of perovskite photovoltaics by means of two designed experimental series. Both are comprised of $MAPbI_3$ planar polycrystal films, first with varying grain sizes from 0.135 μm^2 to 0.984 μm^2, and a layer thickness from 70 nm to 260 nm, by changing the perovskite precursor concentration. The other has grain sizes varying from 0.166 μm^2 to 0.998 μm^2, and a 260 nm fixed layer thickness, achieved by controlling the concentration of additive in the perovskite solution. Both series consist of grain boundaries pointing only in the horizontal direction, as the grains extend throughout the entire film thickness. We combine theoretical simulations with experimental film and device studies to interpret the impact of grain boundaries in perovskite solar cells. A variation of 200 mV in V_{oc}, which appears regardless of layer thickness, highlights that the grain boundaries strongly affect the formation of bulk trap states, underscoring the important role that grain boundaries can play in the non-radiative recombination.

6.2 HPA as an Additive to Tune the Perovskite Grain Size

6.2.1 Controlling the Microstructure of Perovskite Films

In previous work, it has been reported that the principle of including HPA in the precursor solution is to suppress the formation of metallic lead.[93] However the effect of HPA on the microstructure of perovskite films has not been investigated in detail. In this section, we gradually increase the HPA amount (based on an HPA/DMF volume ratio) in the 40% weight ratio perovskite solution to study the effect of HPA on microstructure evolution. At relatively low HPA concentration (2‰-8‰), we monitored the perovskite microstructure by atomic force microscopy (AFM). As

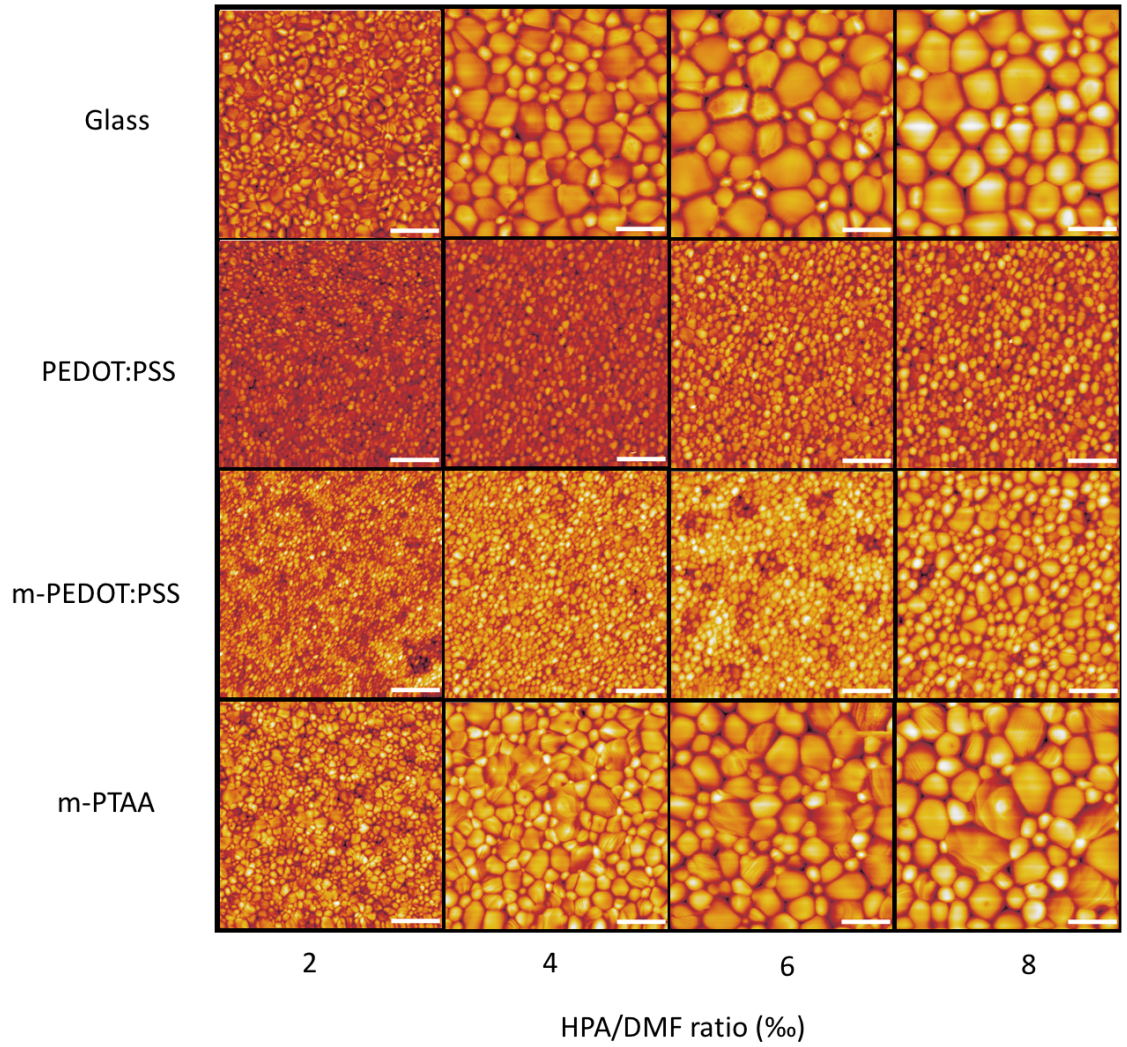

Figure 6.1: AFM micrographs matrix of perovskite with low amounts of HPA deposited on glass, PEDOT:PSS/ITO, m-PEDOT:PSS/ITO and m-PTAA/ITO, the scale bar is 2 μm.

shown in Figure 6.1, the overall films exhibit a desirable morphology for photovoltaic devices, which is smooth, uniform and pin-hole free. Regardless of the substrate, the grain size grows as a function of HPA concentration. However, the average grain size and the degree of increase varies among the different substrates. It is notable that the average grain size and the increase rate of grain size are similar for glass and m-PTAA substrates, while higher than that for PEDOT:PSS and m-PEDOT:PSS substrates.

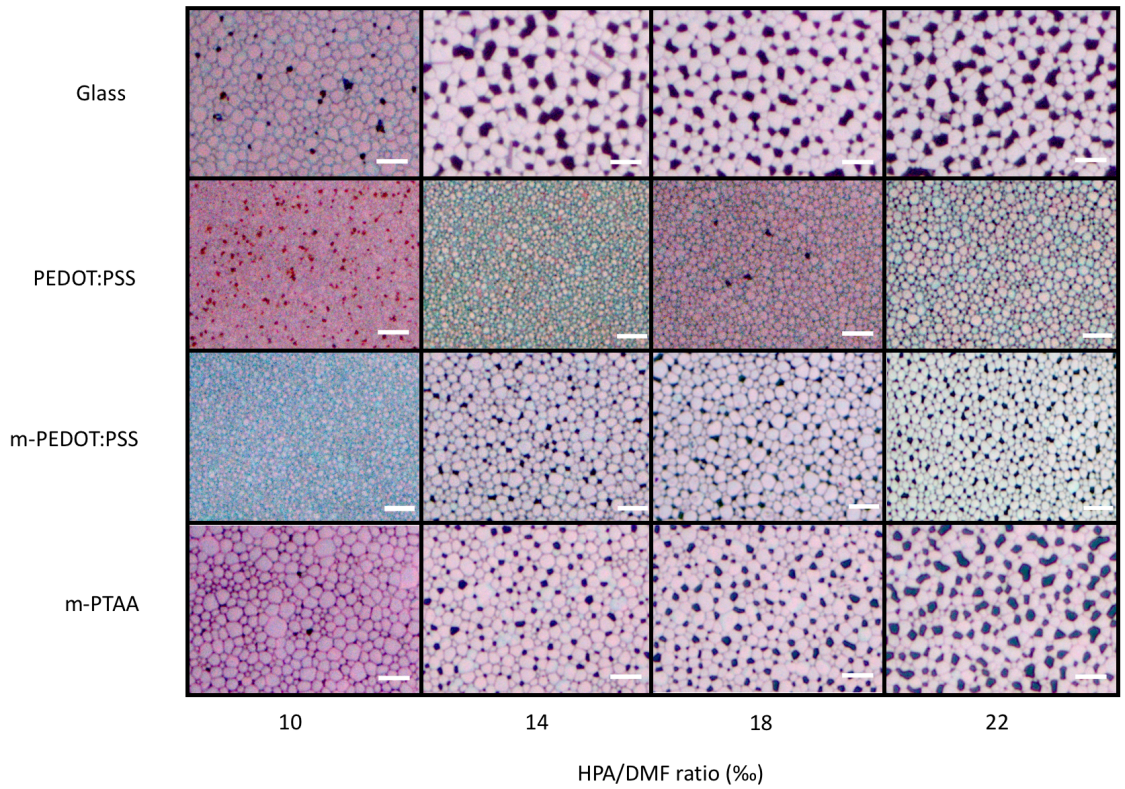

Figure 6.2: Optical microscopy images of perovskite films fabricated with high amounts of HPA deposited on glass, PEDOT:PSS/ITO, m-PEDOT:PSS/ITO and m-PTAA/ITO under brightfield mode top illumination, the scale bar is 10 μm.

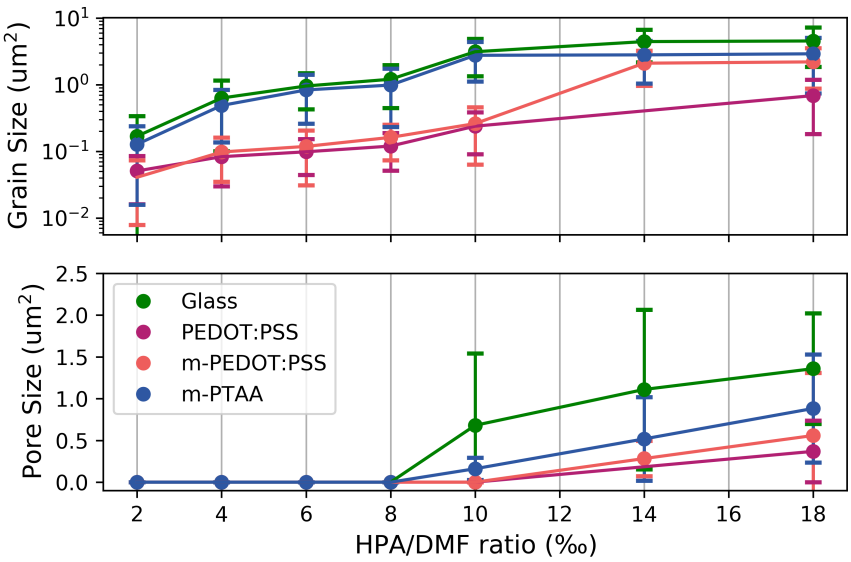

Figure 6.3: Grain size (μm^2) and pore size (μm^2) as a function of HPA/DMF ratio, calculated from Figure 6.1 and Figure 6.2.

Substrates	10‰	14‰	18‰	22‰
Glass	3.31±0.08%	13.67±0.38%	19.80±0.69%	24.20±0.59%
PEDOT:PSS	0	0.09±0.02%	0.32±0.04%	1.54±0.22%
m-PEDOT:PSS	0	4.18±0.19%	11.26±0.75%	16.60±0.95%
m-PTAA	1.54±0.31%	7.96±0.33%	13.42±0.64%	22.62±0.49%

Table 6.1: Porosity calculated based on Figure 6.3.

Since the grain size grows even larger with higher HPA concentrations, the optical microscopy is used to characterize the microstructure.(Figure 6.2) Interestingly, at very high concentrations, the increase rate of grain size slows down and begins to result in discontinuous films with the appearance of porous structures, where both the size and the quantity of pores start increasing with the HPA concentration. To precisely track the morphological evolution, we calculated the average grain size, pore size, as well as the sample porosity, which is defined as the ratio of the porous area to the total film area. These results are summarized in Figure 6.3 and Table 6.1, as well as histograms of grain sizes based on Figure 6.1 are shown in Figure A.14-A.17.

In both the compact and porous film situations, compared to the microstructure of perovskite on glass or m-PTAA, the films fabricated on PEDOT:PSS and m-PEDOT:PSS consist of relatively small grains. As a perovskite solution deposited on hydrophilic surfaces will lead to smaller grains than hydrophobic ones,[109] we employed contact angle measurements to quantify the hydrophobicity. As shown in Figure **??**, the contact angle of a water droplet is higher on glass and m-PTAA than on PEDOT:PSS, suggesting that PEDOT:PSS has a more hydrophilic surface. Thus, the smaller grains on PEDOT:PSS and m-PEDOT:PSS can be explained by their high hydrophilicity. Additionally, such hydrophilic surfaces could also correspond to the delayed appearance of the porous structure, as the pores occur at higher HPA concentration than for the hydrophobic surfaces. When comparing the perovskite microstructure on m-PEDOT:PSS and PEDOT:PSS, a much stronger increase in the average grain size, pore size and porosity can be seen on the m-PEDOT:PSS surface, which could also be associated with a subtle difference in the hydrophilicity of m-PEDOT:PSS substrates caused by inserting polymer

electrolyte PSS-Na in PEDOT:PSS.
It has been reported that a high pH value in DMF results in the formation of formic acid and dimethylamine, which promotes a dissolution of colloids concentration and a reduction of colloids size, as a result leading to larger domains upon deposition.[217] Thus, the reason for enlarging the grain size with HPA concentration is related to a change in the pH value of the perovskite precursor solution by adding addition HPA amount into the solvent N,N-dimethylformamide (DMF). Besides, a low colloids concentration can directly form porous films.[205] It is reasonable that the increase in the grain size and the formation of porous structure are both associated with the changes in the perovskite precursor colloid concentration. Therefore, the final grain size and film porosity will be determined by two factors: the wettability of the substrate surface and the pH value of the precursor solution. Beyond the substrates we have shown here, using HPA to tune the grain size can also be easily applicable to other substrates, as more examples are shown in Figure **??**.

6.2.2 The Crystallinity of Perovskite Film

So far, we have shown that by gradually increasing the HPA concentration the perovskite microstructure can be enlarged by one magnitude order, and eventually formed into a porous structure. Next, to study the influence of HPA concentration on the perovskite crystallinity, we conducted 2D-XRD measurements on the perovskite films which were fabricated by spin-coating perovskite precursor solution with 2‰, 6‰, 10‰, 14‰, 18‰ and 22‰ HPA/DMF (v/v) ratio on glass substrates. The complete, 2-dimensional XRD diffraction patterns are shown in Figure **??**. By integrating the central part of the 2D data, the 1D diffraction profiles are extracted and shown in Figure 6.4(a). The overall prepared films exhibit clear and sharp reflections which correspond to the tetragonal structure of $MAPbI_3$ and agree well with literature.[218] Moreover, the absence of phase separated lead iodide (PbI_2) highlights the high quality of the fabricated films for all different HPA concentrations. However, only at very high HPA concentrations (22‰), two additional low angle reflections at 2θ=8.31°and 2θ=11.07°are observed in the diffraction patterns. These two reflections do not align with known solvent complexes such

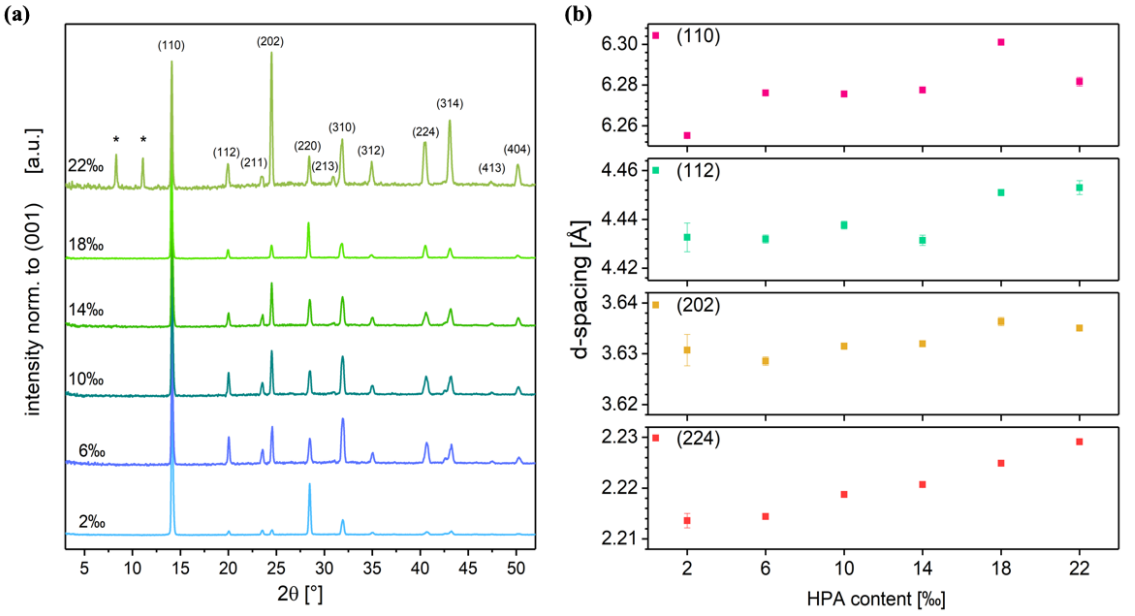

Figure 6.4: (a) XRD pattern of the fabricated $MAPbI_3$ perovskite films on glass with increasing HPA concentration in the DMF solution during fabrication. The relative intensities vary from sample to sample, indicating changes in preferred orientation. All reflections correspond to the tetragonal phase of $MAPbI_3$ and only for high HPA concentration additional reflections (*) of unknown origin are observed at short angles. (b) Extracted d-spacing value for four representative reflections in (a). The overall increase in d-spacing corresponds to a minor extension of the unit cell upon increasing the HPA amount.

as PbI_2·DMF,[219] PbI_2·MAI·DMF,[220] $MAPbI_3$·DMF,[221] or hydrates like MA_4PbI_6·H_2O[219] and $MAPbI_3$·H_2O[221]. Also they do not correspond to the lattice plate of (0,0,1) and (1,0,0) as shown in previous work[222], thus the exact source of these reflections remains unclear.
When comparing the peak intensity and peak position in Figure 6.4(a), we find that the increase of the HPA amount leads to two distinct changes in the microstructure of the films. Firstly, the differences of relative intensities between the two reflections in 1D XRD patterns (Figure 6.4(a)) and the changes in the intensity distribution along the Debye rings in the 2D XRD patterns (Figure **??**) indicate that the increase of HPA slightly changes the preferred orientation within the polycrystalline film. Secondly, the peak width becomes narrower, from 2‰to 22‰, suggesting that a slight extension of the perovskite unit cell is caused by the increasing amount of HPA concentration and the formation of pores in the film, and as a consequence

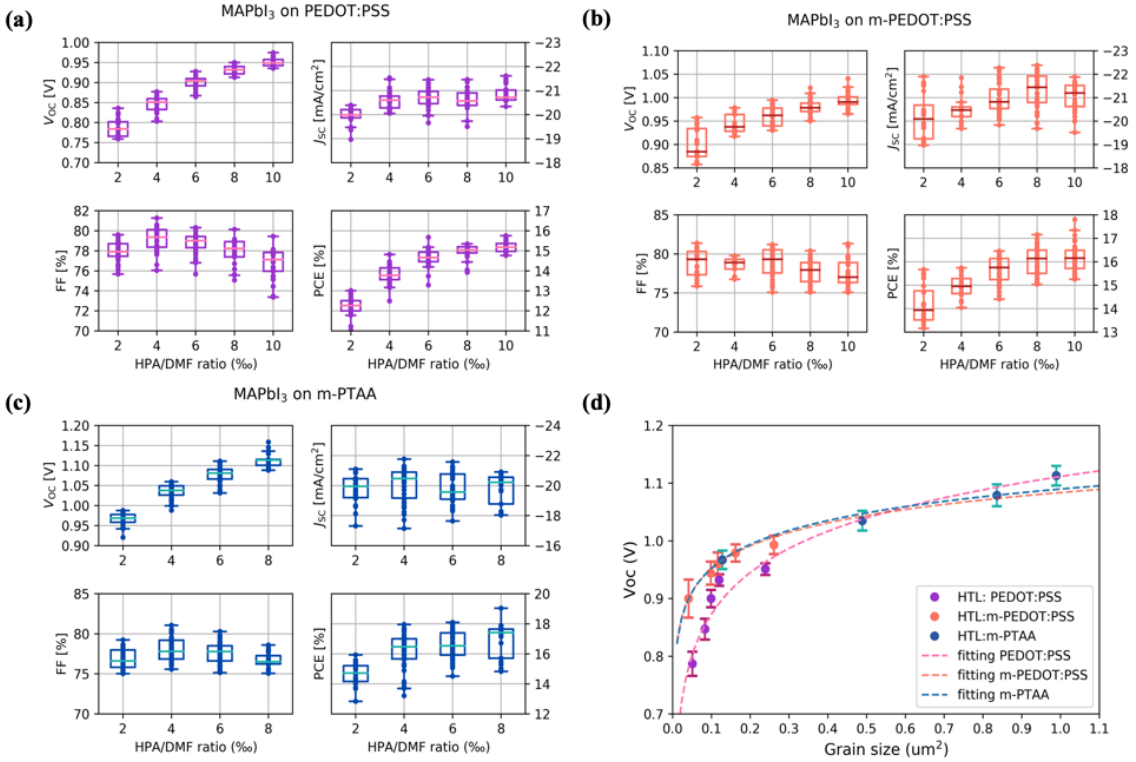

Figure 6.5: Photovoltaic performance of perovskite film containing varying amounts of HPA on commonly used hole transport layer (a) PEDOT:PSS, (b) m-PEDOT:PSS and (c) m-PTAA. (d) V_{oc} obtained from all three HTLs as a function of grain size.

larger d-spacing values for the corresponding Miller planes can be seen in Figure 6.4(b). The reason for such changes can be explained by a relaxation in the lattice strain of the film with increasing porosity. Since the lattice strain has been recently recognized as a source of non-radiative losses in perovskite materials,[223] perovskites with a higher HPA concentration could achieve better V_{oc} photovoltaic performance.

6.2.3 Photovoltaic Performance

As PEDOT:PSS, m-PEDOT:PSS and m-PTAA are three commonly used hole transport layers, to investigate the photovoltaic performance of the perovskite layers with different HPA concentrations, we can complete these films into photovoltaic devices by subsequently spin-coating PCBM as electron transport layer, BCP as hole blocking layer, and finally thermally evaporating silver as cathode. Considering that a homogeneous and

pin-hole free perovskite film is one of the key factors to achieve high photovoltaic performance, we only fabricated solar cells with HPA/DMF ratio until 8‰on m-PTAA, while the other two allow for a concentration up to 10‰. Figure 6.5(a)-(c) show the photovoltaic parameters as a function of HPA/DMF ratio.

Even with a minor change in HPA/DMF ratio, the variation of photovoltaic performance is dramatically obvious for all three hole transport layers, especially in the open circuit voltage (V_{oc}) and power conversion efficiency (PCE). The V_{oc} quasi-linearly increases by more than 100 mV with the HPA/DMF ratio. Unlike V_{oc}, the fill factor (FF) and the short circuit current (J_{sc}) remain largely unchanged, and as a result the PCE increases by over 2%.

Since the concentration of HPA effectively changes the microstructure of perovskite films - especially the grain size - the increase in V_{oc} as a function of the average perovskite grain size on each hole transport layer is analyzed in Figure 6.5(d). At similarly (small) grain sizes for devices employing PEDOT:PSS and m-PEDOT:PSS, the V_{oc} of m-PEDOT:PSS devices is higher than that of PEDOT:PSS ones, due to the 0.3 eV difference in the work functions of these HTLs. With larger grain sizes, this differences in V_{oc} becomes smaller, which is in agreement with numerical simulations which show that the effect of energetic misalignment with the HTL is less significant for perovskite layers with low recombination losses.[107] Notably, the overall V_{oc} of devices using m-PEDOT:PSS is smaller than that of m-PTAA, while the line of best fit for m-PEDOT:PSS and m-PTAA almost overlap. This overlapping can be attributed to their similar work function[77, 224] and indicates that comparing with the m-PTAA devices, the main reason for the low V_{oc} of m-PEDOT:PSS devices could result from the small grain size.

Interestingly, by solely increasing the grain size of the perovskite layer, the V_{oc} of the photovoltaic devices (regardless of HTLs) all increase by over 200 mV (up to 1.16 V), which can be associated with the relaxation of lattice strain and reduction of grain boundaries. Since the behaviors of grain boundaries are still under debate, varying the HPA concentration in the perovskite precursor solution offers a way to study the effects of grain boundary in detail. In the following section, we will discuss the behavior

of grain boundaries in perovskite solar cells through devices with controllable grain sizes.

6.3 Study the Effects of Grain Boundaries via Tuning of the Grain Size

6.3.1 Controlling the Perovskite Grain Size

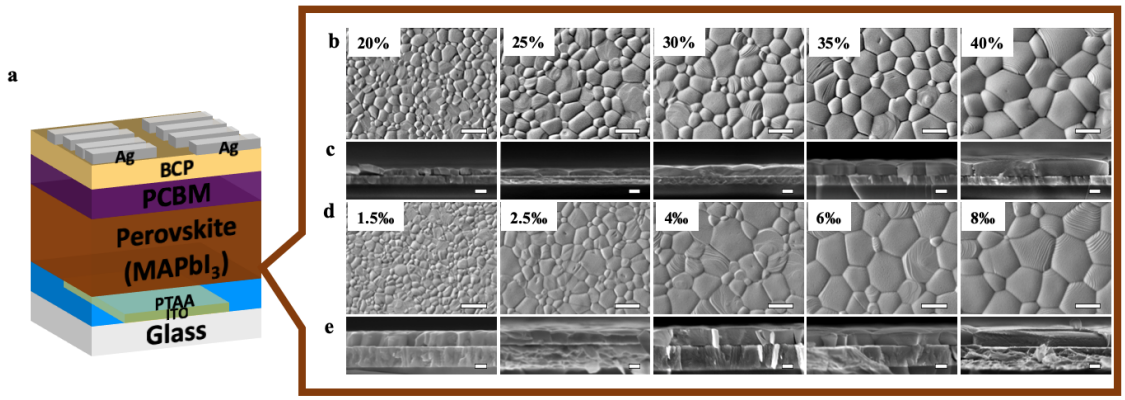

Figure 6.6: (a) Schematic photovoltaic device structure. Top view (a) and cross sectional (b) SEM images of grain size controlled by varying perovskite precursor concentration (type A). Top view (c) and cross sectional (d) SEM images of grain size controlled by 40%wt perovskite precursor with variable additive concentration (type B). The scale bar of top view and cross sectional view is 1 μm and 100 nm, respectively.

The photovoltaic device structure applied in this section is schematically illustrated in Figure 6.6(a), where we used PTAA as the HTL in the p-i-n planar heterojunction device. To pinpoint the effect of grain boundaries, devices with variable grain size were fabricated with all remaining layers unchanged.

During the investigation of the HPA effect on the microstructure of perovskite films, we also find that the weight ratio of the precursor solution could determine the maximum achievable grain size. We fabricated samples in 20%wt to 40%wt with the same HPA/DMF ratio (6‰). As shown in Figure **??**, low weight ratio samples (20%wt, 25%wt, 30%wt) exhibit porous structure with small grain sizes, while high weight ratio samples (35% and 40%) show pin-hole free microstructure with large grains. Thus, a series of devices with grain size from small to large can be fabricated

via optimizing the HPA amount for each perovskite precursor weight ratio (20%wt, 25%wt, 30%wt, 35%wt, 40%wt), details of which can be found in Table B.7. We refer to these types of devices as type A, and label as 20% to 40%. Because the weight ratio for each is different, the devices in type A not only have different grain sizes but also have different layer thicknesses. In addition to type A, devices referred to as type B (label 1.5‰to 8‰) are prepared by tuning the HPA concentration in 40%wt perovskite precursor solution (the same way described in Section 6.2). As a result, all of the devices in type B have the same layer thickness. We aim to obtain similar grain sizes in both type A and type B devices.
To assess the microstructure and crystallinity of the films in type A and type B, we performed AFM and scanning electron microscopy (SEM) in conjunction with XRD. The top view SEM images of perovskite microstructure on ITO/PTAA substrates for type A and type B are shown in Figure 6.6(b) and Figure 6.6(d), respectively. Fully compact but gradually enlarging grains appear in both figures, suggesting a successful tuning of grain size without alterations to the surface morphology, in agreement with the previous section. The SEM cross-section images (Figure 6.6(c) and Figure 6.6(e)) show highly crystalline perovskite layers with single grains which extend throughout the entire thickness of the film, confirming that the grain boundaries are created only in horizontal direction, thus the films with apparently small grains can represent films with a high density of grain boundaries.

Label	**20%**	**25%**	**30%**	**35%**	**40%**
Layer thickness (nm)	75	105	150	190	260
Grain size (μm^2)	0.14±0.08	0.20±0.15	0.47±0.27	0.58±0.35	0.98±0.46
Label	**1.5‰**	**2.5‰**	**4‰**	**6‰**	**8‰**
Layer thickness (nm)	260	260	260	260	260
Grain size (μm^2)	0.17±0.10	0.22±0.19	0.40±0.27	0.72±0.43	1.00±0.74

Table 6.2: Summary of grain size and layer thickness of type A and type B.

Based on the AFM images, we characterize the grain size (Figure **??**) and summarize the results of average grain size together with the layer thickness in Table 6.2. As expected, though the layer thicknesses of type A and type B devices are not the same, the films do have similar grain sizes, for

example 20% in type A and 1.5‰ in type B have a similar average grain size of 0.14 μm^2 and 0.17 μm^2, respectively.
To further confirm that we only varied the grain size, or alternatively the quantity of grain boundaries, without altering the overall quality of the perovskite films, XRD measurements were performed in 2D-diffraction mapping mode (Figure **??**). The 2θ diffraction profiles shown in Figure 6.7(a) and Figure 6.7(b) are obtained from a central integration of the 2D data scan mode. Notably, all the films show the typical tetragonal perovskite diffraction patterns without major impurities or phase separation, in agreement with previous section (Figure 6.4). Despite the layer thicknesses and grain sizes are varied, a similar intensity distribution along the Debye rings in the 2D patterns is observed and indicates an unchanged preferred orientation. Similar to Section 6.2.2, the full width at half maximum of the (110) peak in both kinds of samples is smaller with increasing grain size (Figure **??**). Thus, so far our results demonstrate that high quality polycrystalline perovskite films with controlled grain size are achieved in both type A and type B.

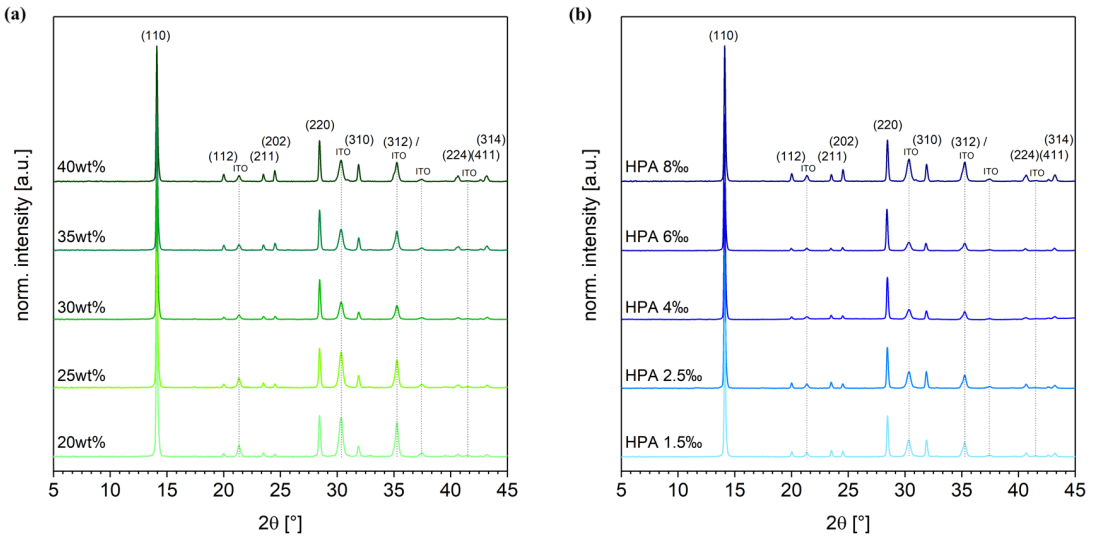

Figure 6.7: XRD profiles of perovskite films with differing grain size on PTAA/ITO substrates. Samples were fabricated by (a) varying the perovskite precursor concentration (type A) and (b) varying the additive concentration (type B).

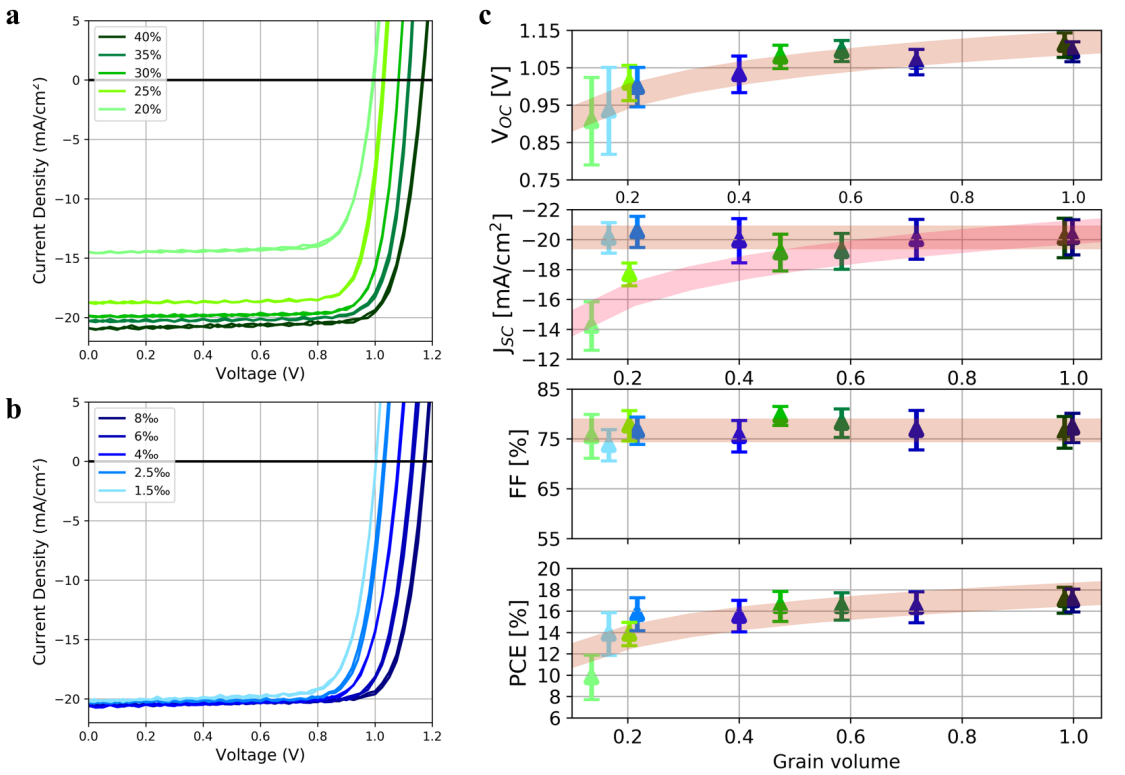

Figure 6.8: $J-V$ curves of grain size varied by (a) perovskite precursor concentration (type A) and (b) additive concentration (type B). (c) Statistics of photovoltaic performance (combining both type A and type B) as a function of the average grain size for over 580 devices.

6.3.2 Effect of Grain Size on Photovoltaic Performance

To start the device analysis, we study the current-voltage characteristics under AM 1.5G sun illumination. The current density-voltage characteristics of device type A and type B are shown in Figure 6.8(a) and Figure 6.8(b), as well as the performance parameters are summarized in Table B.8 and Table B.9, respectively. Since both the electron and hole extraction layers were kept the same in all devices, similar charge extraction can be expected in both type A and type B. However, as the perovskite layer thickness increases with the weight ratio of perovskite precursor solution, the gradual increase of the J_{sc} in type A can be associated with higher absorbance by the thicker perovskite layer. This is supported by the 20% device possessing the same external quantum efficiency (EQE) spectral shape, but with a lower onset shoulder when compared to the 40% curve

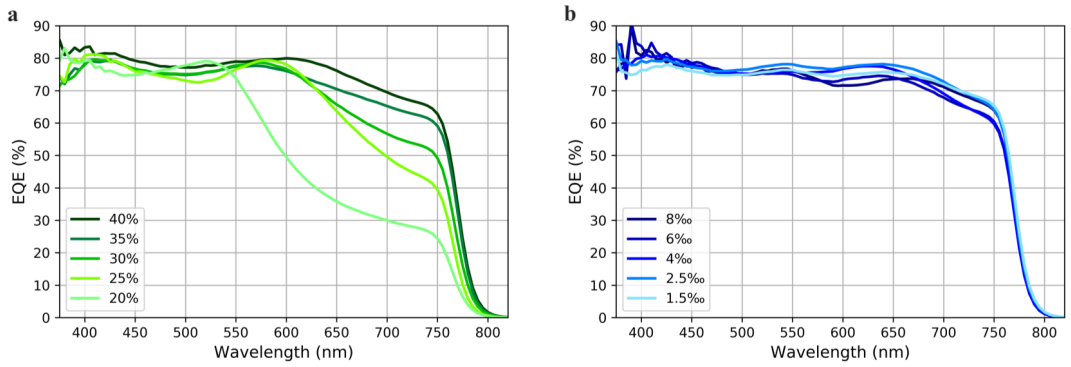

Figure 6.9: External quantum efficiency spectra of devices with different grain size fabricated by varying (a) the perovskite precursor concentration (type A) and (b) the additive concentration (type B).

(Figure 6.9(a)). The trend in the EQE shape observed in Figure 6.9(a) for the type A devices agrees with previous observations,[43] while for type B, there is no discernible trend, leading to a similar J_{sc} with equal photon absorption for all devices.

Interestingly, a more than 160 mV enhancement of V_{oc}, and a slight increase in FF, can be observed in both types. Unlike type A, type B devices only possess a gradual grain size enlargement in the perovskite layer (see Figure 6.6). This allows us to directly link the enhancement of V_{oc} with the increase in grain size. While in type A, the origins of the V_{oc} enhancement is unclear, as it may due to the change in grain size or the increased layer thickness. To further elucidate our observation, the photovoltaic parameters of both device types are summarized as a function of the average grain size and shown in Figure 6.8(c). Overall, the V_{oc} exponentially increases with the grain size, greatly impacting the performance of PCE. The only slight change in FF suggests that the perovskite/extraction layer interfaces remain largely unaffected by changing the grain size and layer thickness. Of particular note, devices with similar grain size between type A and B have almost the same V_{oc} and FF regardless of J_{sc} (the layer thickness), especially for the 25% (type A) and 2.5‰ (type B) labeled devices. This similarity indicates that, even with different absorber thickness, the variation in the V_{oc} is highly dominated by the change in the grain size, which causes a corresponding change in the number of grain boundaries, emphasizing that grain boundaries are detrimental to device performance.

6.3.3 Non-radiative Recombination in Perovskites with Variable Grain Sizes

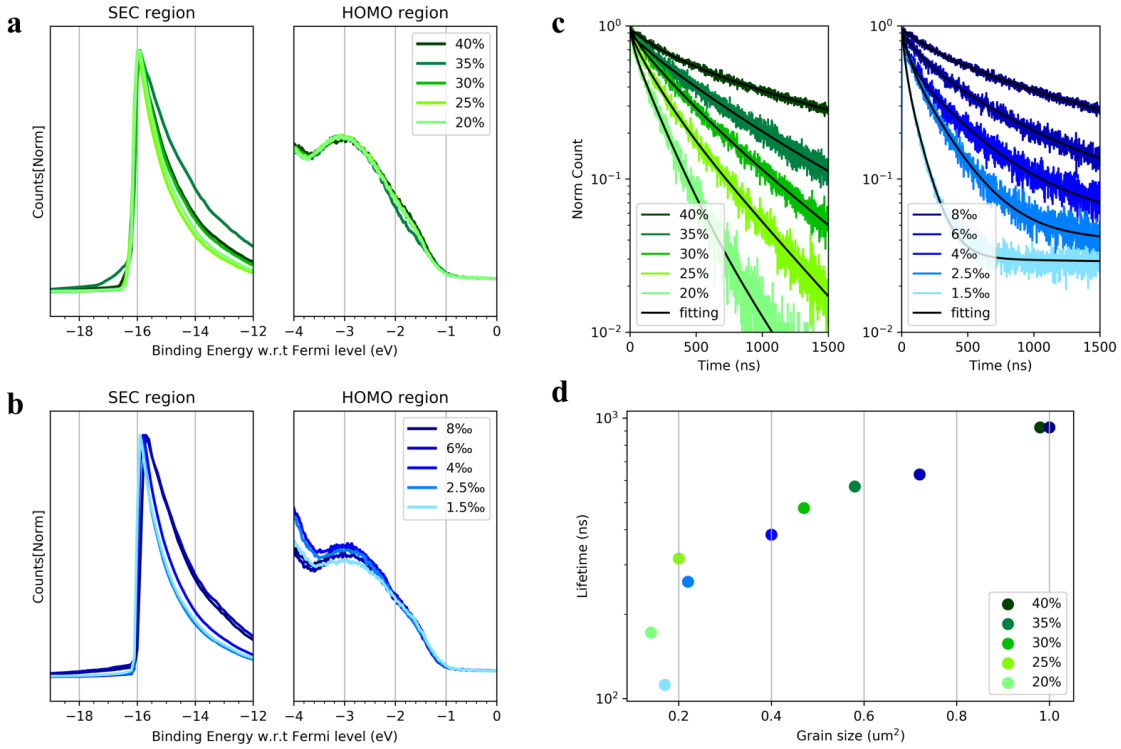

Figure 6.10: Ultraviolet photoemission spectroscopy measurements of perovskite films with different grain size on PTAA/ITO substrates, fabricating by varying (a) the perovskite precursor concentration (type A) and (b) the additive concentration (type B). (c) Normalized time correlated single photon counting (TCSPC) photo decay for the films from type A and type B on glass substrates. (d) Lifetime that is extracted from TCSPC as a function of perovskite average grain size.

An improvement in the V_{oc} may result from a variety of mechanisms, including an increase in the built-in potential or a suppression of non-radiative recombination. To identify the origin of the V_{oc} enhancement, we measured the energetic alignment, charge carrier lifetime, Urbach energy and the light-intensity dependent V_{oc} characteristics on both type A and type B devices. Firstly, we employed ultraviolet photoemission spectroscopy to explore the impact of grain sizes on perovskite energetic levels. Figure 6.10(a) and Figure 6.10(b) show the work function (WF) and ionization potential (IP) of films in type A and type B, respectively. The WF

and IP determined from the secondary electron cut-off (SEC) region and on-set (HOMO) region are largely unchanged, suggesting that the changes in perovskite microstructure do not alter the energetic levels, resulting in an unchanged the built-in potential of each device type. However, there is a small ~0.2 eV increase in WF of type A over type B, which could be caused by bottle to bottle precursor materials variation, especially the lead acetate trihydride. This could also be responsible for the overall slightly lower V_{oc} exhibited by type B.

Since the build-in potential as a reason for the V_{oc} improvement is excluded, we characterized the grain size effect on charge carrier radiative recombination processes in the device to further investigate the origin of the V_{oc} enhancement. Time correlated single photon counting (TCSPC) measurements were employed to assess the lifetime of the charge carriers (Figure 6.10(c)), and the corresponding results were plotted as a function of grain size in Figure 6.10(d). In both type series, the films that contain the smallest perovskite grain size exhibit a lifetime as short as 172 ns and 112 ns. While when the grain size increases to ~1.00 μm^2, a slower decay process appears with a long lifetime of 927 ns. This increase suggests that the reduction in the number of grain boundaries suppresses non-radiative recombination processes, corresponding to an increase in device Voc. Upon measuring the steady-state photoluminescence, we found the emission intensity increases with enlarging grain size, in agreement with the model of suppressed non-radiative recombination observed by the TCSPC measurements. (Figure **??**)

It is well known that since the trap-assisted recombination is the dominant pathway of non-radiative recombination, the light intensity dependent V_{oc} measurements can be used to provide information about the trap-assisted recombination.[127] Figure 6.11(a)(b) show a semilogarithmic plot of V_{oc} as a function of light intensity. These two parameters exhibit a linear relationship with a slope proportional to k_BT/q for all the devices. The slope of 40% (large grains) and 20% (small grains) in type A is 1.36 k_BT/q and 1.87 k_BT/q, respectively. Similar to type A, the slope of 8‰(large grains) and 1.5‰(small grains) in type B is 1.36 k_BT/q and 1.73 k_BT/q, respectively. Since a slope close to unity means a minimal non-radiative recombination, these results clearly demonstrate that even though trap-assisted recombina-

tion is present in all the devices, decreasing the number of grain boundaries reduces trap-assisted recombination of charge carriers in perovskite photovoltaic devices.

One sorce of these traps are defect states that exist within the bandgap. In order to quantify these sub-bandgap states, we performed photothermal deflection spectroscopy (PDS) to estimate the Urbach energy of the perovskite films (Figure 6.11(c)).[40] By fitting the exponential increase in the absorption of perovskite films at the band edge of 1.53 eV to 1.6 eV in the spectra,[225, 226] we found that the Urbach energy drops from 20.7 meV to 17.4 meV with an increase in grain size. (Figure 6.11(d)) This decrease in Urbach energy is more direct evidence for the suppression of energetic disorder (sub-bandgap trap like states) in perovskite films by reducing the grain boundaries, indicating a lower trap density in large grain size films.

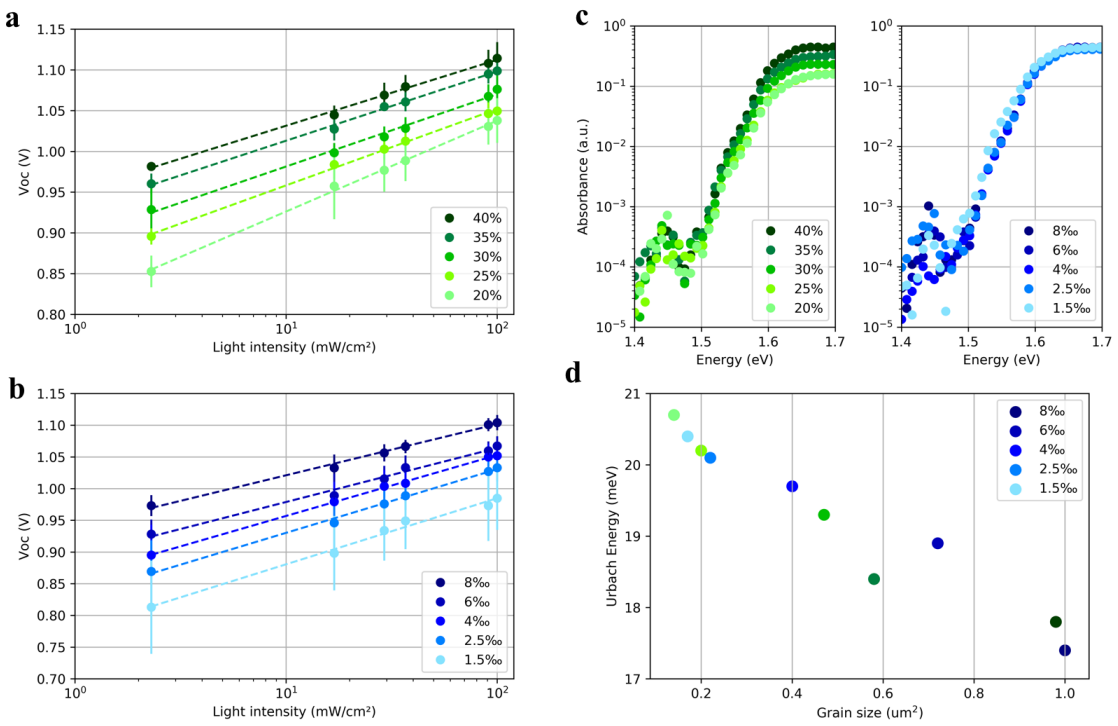

Figure 6.11: V_{oc} dependence upon light intensity of perovskite solar cells with different grain size, the samples were fabricated by varying (a) perovskite precursor concentration (type A) and (b) additive concentration in fixed precursor concentration (type B). (c) Photothermal deflection spectroscopy (PDS) for the films with variety grain size on glass substrates, left for type A and right for type B. (d) Urbach energy extracted from PDS figures as a function of the perovskite average grain size.

So far, we have shown that in films where the grains extend through the full film thickness, the grain boundaries are the dominating factor in suppressing the non-radiative recombination regardless of the layer thickness, as shown by TCSPC, light intensity dependent $J-V$, and PDS measurements, and therefore by reducing the number of grain boundaries by enlarging the grains themselves enhance the V_{oc}. Since grain boundary can serve as the recombination centers (trap centers), where greatly annihilate the free charge carriers. We attribute the suppression of non-radiative recombination to the reduction of trap density in large grain films.

6.3.4 Effects of Grain Boundaries

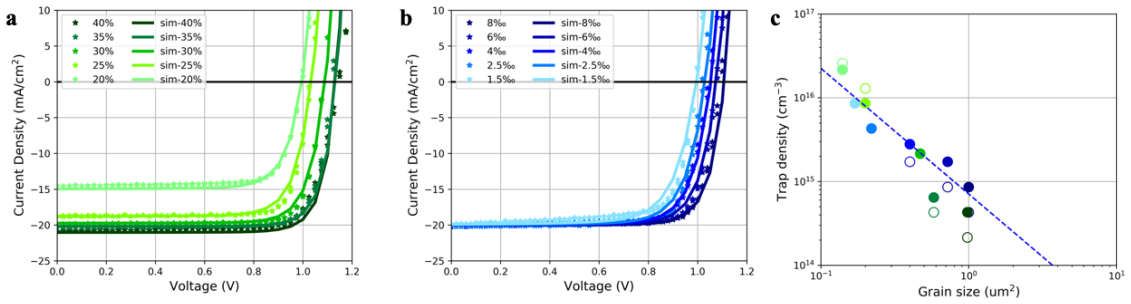

Figure 6.12: Simulated $J-V$ curves with the experimental $J-V$ curves for (a) type A with unfixed layer thickness and (b) type B with fixed layer thickness. The currents were measured or simulated under AM 1.5G illumination condition. (c) Trap density as a function of the average grain size based on the simulation results from light $J-V$ (full dot) and dark $J-V$ curves (empty dot). The dash line represents a y=c+ax^{-}1.5 function.

To support our hypothesis that the enhancements of V_{oc} originate from the reduction of trap density due to fewer the grain boundaries, and gain further insights into the relationship of defect density with grain size, we performed simulations (done by Sapir Bitton under the supervision of Prof. Nir Tessler) on $J-V$ curves under 1 sun illumination (Figure 6.12(a),(b)) and in the dark (Figure **??**) for both device type A and B, following a previously developed model[107]. The parameters used for the simulations are listed in Table B.10.
Based on the SRH theory, the recombination rate is a product of the trap density times the capture coefficient.[37] As for the same material, the

electron capture rate remains constant, which means the capture coefficient in our case is fixed. Thus the evolution of the trap density can be extracted from the simulations. Figure 6.12(c) illustrates the trap density as a function of the average grain size for each device, where the trap density grows as the grain size become smaller. Since the grain boundaries are like an aggregation of point defects and may act as deep trap states,[37, 227] such a behavior of trap density could be expected due to a higher overall quantity of grain boundaries. Based on the AFM images (Figure **??**), we estimate the total length of the grain boundaries for each sample. As revealed in Figure **??**, the total length of grain boundaries increases by approximately a factor of three from the films with the smallest to the largest grains. However, the trap density increases by two orders of magnitude (Figure 6.12(c)), which is far more than expected from the increase of grain area alone. This result suggests that the grain boundaries of small grains are more efficient as recombination centers than those of large grains.

As the grain boundaries in our case are present only in the horizontal direction and the photogenerated charges are transported in the vertical direction towards the charge extraction layers, a fundamental question is raised about how the traps which are located at the grain boundaries influence the charges is raised. To answer this question, the geometry of the grain and the charge transport must be taken into account. We represent a grain by a simplistic model, where the grain is treated as a cuboid. The distance between two vertical faces (grain boundaries) and two horizontal faces (equal to active layer thickness) are L and d, respectively. Additionally, the charge transport includes both drift and diffusion, which at the voltages close to V_{oc} (or maximum power point, MPP) where the losses are prominent, it is mainly the diffusion governing the charge transport. Therefore, in the following we consider both the geometry of the grain and the charge transport (including both drift and diffusion) in order to estimate the effective volume-density of defects as a function of grain size.

Firstly, we only consider the geometry and assume that the traps are only located at the cuboid surfaces. The total number of defects follows the formalism defined by Filippo de Angelis and coworkers[228], as $N_{defects,surface} = 4S_{gb}Ld + 2S_{int}L^2$ where S_{gb} and S_{int} are the surface de-

fect density at the grain boundaries and at the interfaces with the extraction layers, respectively. Thus, the defect volume density can be expressed as $V_g = \frac{N_{defects,surface}}{dL^2} = \frac{4S_{gb}}{L} + \frac{2S_{int}}{d}$. If $S_{int} \ll S_{gb}$ which means the interfaces are properly passivated, the defect volume density reduces to $V_g \sim \frac{4S_{gb}}{L} = \frac{4S_{gb}}{\sqrt{GrainArea}}$, the surface density is straightforward translated to volume density.

It is notable that the approach mentioned above includes the assumption that the photogenerated charges within the bulk of the grain will definitely interact with the traps at the grain boundaries. However, the interaction between traps and the charges has a finite probability. To relate this probability to the defect volume density, we need to consider the dynamics of diffusion processes which is the main transport procedure close to V_{oc} (or MPP). Assuming the diffusion coefficient of a charge carrier is D, the time it takes to diffuse between two grain boundaries (horizontal direction) and the interfaces with the charge extraction layers (vertical direction) are $\tau_{gb} = L^2/D$ and $\tau_{int} = d^2/D$, respectively. Therefore, the recombination efficiency will be proportional to the ratio as shown in Equation 6.1. Finally, effective volume density of traps can be expressed as $V_g = \frac{4d^2 S_{gb}}{(GrainArea)^{1.5}}$, which is in good agreement with the relation of the extracted density of defects to the grain size (Figure 6.12(c), dashed line).

$$Rec_{eff} = \frac{\frac{1}{\tau_g b}}{\frac{1}{\tau_{int}} + \frac{1}{\tau_{gb}}} = \frac{\tau_{int}}{\tau_{int} + \tau_{gb}} \rightarrow \tau_{gb} \gg \tau_{int} \sim \frac{\tau_{int}}{\tau_{gb}} = \frac{d^2}{L^2} = \frac{d^2}{GrainArea} \quad (6.1)$$

After deriving an expression for the effective trap density as a function of grain size, we can also discuss the effect of grain size distribution on the photovoltaic performance. To simplify the model, we assume that the grain size distribution is Gaussian with an average grain size and a distribution width σ (Figure 6.13(b)). This distribution is used to define the average effective volume trap density and σ is employed to simulate the device $J-V$ under one sun. Figure 6.13(c)-(f) illustrate the effect of the average grain size and the distribution of grain size on the photovoltaic performance. As shown in Figure 6.13(c), the V_{oc} is influenced by not only the average grain size, but also the distribution width of grain sizes. Especially for samples

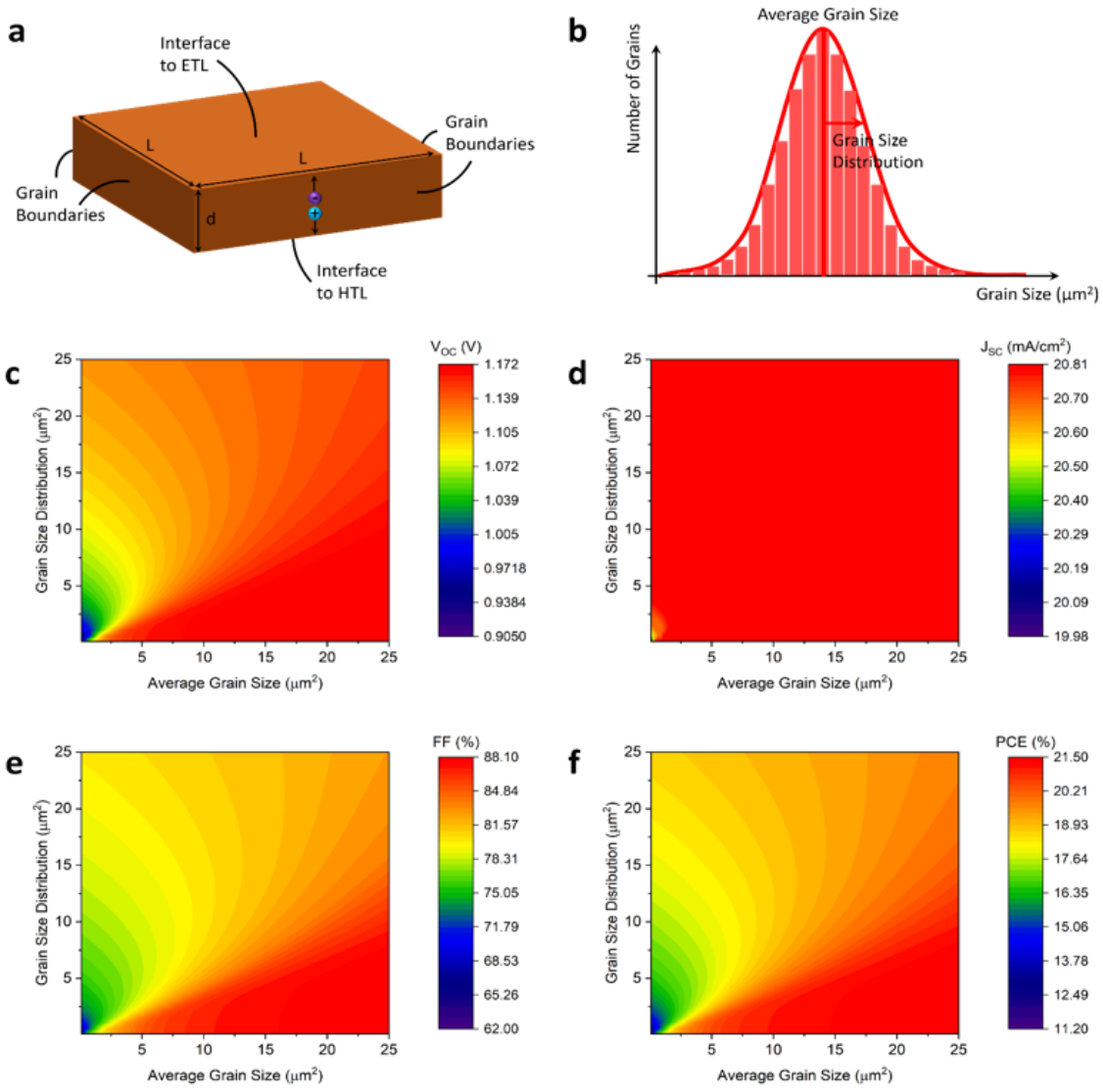

Figure 6.13: (a) Schematic of the geometry of a grain boundary. (b) Simulated histogram of grain size distribution. The evolution of (c) V_{oc}, (d) J_{sc}, (e) FF and (f) PCE as a function of the average grain size and grain size distribution.

with an average grain size below 5 μm^2, an increase of the grain size distribution width results in a significant reduction in the V_{oc}, which can be associated to the increased recombination losses caused by the presence of more small grains. A similar effect is also observed in case of the FF and PCE. While unlike the V_{oc}, FF and PCE, the impact of grain size distribution width on J_{sc} is only in a very limited range of grain size and almost can be neglected.
These results illustrate that as long as there are sufficient small grains (resulting from a wide distribution) to mask the effect of larger grains, it is possible for samples with a larger average grain size to exhibit a higher recombination rate,[202] if only considering the average grain size, not the entire distribution. Our results highlight the importance of eliminating small grains from the films' microstructure, as such grains contain high density of defects and they are responsible for the majority of non-radiative recombination losses. Experimental efforts should be devoted not only to enlarge the average grain size, but also to remove the small grains. As shown in Figure 6.13(f), the PCE of $MAPbI_3$ devices can be nearly doubled from 11.2% to 21.5% through solely varying the grain distribution within the active layer.

6.4 Summary

In this chapter, we first demonstrate that HPA is an effective additive to control over the microstructure of perovskite thin films. On a large range of underlying substrates, tuning the amount of HPA in the perovskite precursor allows us to enlarge the grain size by over one order of magnitude without altering the topology of the perovskite thin films, while further increasing the HPA content forms porous structures with controlled porosity. Moreover, a larger d-spacing values extracted from the XRD measurements also illustrate that from small grains to large grains, and from compact layer to porous layer, the changes in the film microstructure via tuning the HPA concentration are accompanied by an expansion in the perovskite unit cell. The high quality porous perovskite structure could be potentially interesting for application in other types of optoelectronic devices, such as light-emitting diodes. Besides tuning the HPA concentration, we also demonstrate that the weight ratio of the perovskite precursor can be used

to tune the grain size as evident that keeping the same amount of HPA in the solution, larger grains are achieved with higher weight ratios.
Secondly, we systematically investigated the effect of grain boundaries in perovskite solar cells via a combination of experimental studies and numerical device simulation. We show that with increasing average grain size, the V_{oc} can be significantly enhanced by over 200 mV accompanied by a minor increase in the FF. Reproducing the light and dark $J-V$ curves of the two series of devices by device simulations, we find that the changes in photovoltaic performances are well represented by changes in trap-assisted Shockley-Read-Hall recombination. Notably, the SRH recombination rate is two orders more efficient in small grains when compared to the large ones. Taking both geometry and charge transport into consideration, we reveal that the relationship between the defect density and grain area follows the rule $N_{defects} \propto (GrainArea)^{-1.5}$, in excellent agreement with experimental results. Using this relationship, we evaluate the role of grain size distribution in device performance and find that narrowing the grain size distribution is a key factor in reducing the recombination losses and improving the device photovoltaic performance. Small grains are recombination hot spots in perovskite solar cells.

Chapter 7

Conclusions and Outlook

The main purpose of this thesis is to investigate the two main subjects in perovskite photovoltaics: interfaces between two adjacent layers and 'bulk interfaces' grain boundaries. By modifying the interface of $ZnO/MAPbI_3$ and by inserting new synthesized HBLs in PCBM/Ag interface, we demonstrate that interfaces are non-negligible in improving photovoltaic performance. Combining experimental studies and numerical device simulations of perovskite with different size of grain, we reveal that the grain boundaries are the host for the traps and the small grains dominate the trap density in perovskite bulk.
In chapter 4, we focus on the n-i-p photovoltaic architecture and study the $ZnO/MAPbI_3$ interface.To solve the problem of perovskite decomposition on ZnO surface, we engineered the ZnO layer by modifying its surface via PCBA SAM and doping Cs or Li into ZnO bulk. The XPS depth profiling and conductivity upon illumination measurement demonstrate that dopants reduce the ZnO trap states both in bulk and surface. While SEM images prove that only with PCBA surface modification on ZnO stops the decomposition of perovskite, doping itself can't. This demonstrates that interface dominates the microstructure of perovskite. Moreover, characterizing the energy level of engineered ZnO by UPS measurement, we find that PCBA lower the WF of the metal oxide, helping the charge extraction from perovskite to ETL. Finally, when combine the advantage of PCBA surface modification and Li bulk modification on ZnO, the perovskite photovoltaic performance is significantly improved by twofold in average, which suggests that ZnO can serve as an efficient electron transport layer in perovskite photovoltaic devices.

In chapter 5, four newly synthesized electrolytes are applied as HBL in p-i-n perovskite architecture. By measuring the energy level of the new HBLs, the charge carrier lifetime of perovskite film, EL and TPC as well as light intensity dependent V_{oc} measurement on the photovoltaic devices, we demonstrate that the new HBLs can efficiently block holes and suppress the non-radiative radiation, leading to a higher FF and V_{oc} in the performance of devices. An enhanced electron conductivity in unipolar electron only devices with new HBLs illustrates that the new HBLs can protect the PCBM from the penetration of Ag atoms, which could reduce the trap density of PCBM and associate to the suppression of non-radiative recombination. Moreover, we also demonstrate that the new electrolytes form a dipole moment at the PCBM/Ag interface that shifts up the device build-in potential. Confirming by a numerical simulation, this dipole moment also contributes to the enhancement of V_{oc}. Our results pinpoint that modifying the interface of ETL/metal contact interface is a promising way to suppress the non-radiative recombination for achieving higher efficiency in perovskite devices and can also be used to compensate the non-ideal energetic alignment among the devices.
In chapter 6, we first report a facile approach to control the microstructure of perovskite. By changing the amount of additive HPA in the perovskite precursor solution, it is versatile to tune the perovskite grain size and the porosity of perovskite film on various substrates. By varying the perovskite solution weight ratio or the HPA amount, we can easily achieve two types of perovskite films: type A, a series of perovskite films with different grain size and fixed layer thickness and type B, a series of perovskite films with similar grain size of type A but different layer thickness. These two type of perovskite microstructures allow us to systematically study the effect of grain boundaries in the photovoltaic performance. By carefully examine the charge carrier life time, energetic alignment, energetic disorder and trap-assisted recombination of such two type devices, we demonstrate that grain boundaries nourish the non-radiative recombination, and a reduction of grain boundaries results in a higher V_{oc}. In addition to the experimental studies, our numerical simulation results demonstrate that the grain boundaries act as the host of trap states to provoke the trap density in the perovskite bulk, which is detrimental for the perovskite photovoltaic

performance. Our results also reveal the defect density is proportional to $1/GrainArea^{1.5}$ of the grain area. More importantly, through characterizing the role of grain size distribution, we point out that a narrow grain size distribution results in a reduction of recombination losses and an increase of the device performance. Our work highlights that grain boundaries play an important role in determining the non-radiative recombination losses in perovskite materials and further experimental efforts should be devoted to optimize the active layer microstructure, not only focus on enlarging the grain size, but in particular eliminating the small grains.

Nowadays, with more and more research interests drawing on the organic-inorganic halide perovskite, further study has reported that pure $MAPbI_3$ is instable against the light and heat in perovskite solar cells.[229] To obtain high quality perovskite, multi-components perovskite such as $Cs_{0.05}(FA_{0.83}MA_{0.17})_{0.95}Pb(I_{0.9}Br_{0.1})_3$ or MA-free perovskite such as $Cs_{0.1}FA_{0.9}PbI_{2.9}Br_{0.1}$ attract attentions. Since in state-of-art layer by layer photovoltaic devices, the absorber microstructure and interface play an important role on photovoltaic performance, no matter what perovskite materials will be used, the strategies discussed in this thesis can be implanted into other similar system. To further boost the photovoltaic efficiency, new materials should be synthesized and employed to modify the interfaces for compensating the energetic losses, reinforcing the perovskite microstructure and etc. Regardless of the device structures, there are at least 4 interfaces in each photovoltaic devices, all the interfaces need to be paid equal attentions. Moreover, as the grain boundaries are detrimental and act as trap centers in the perovskite bulk, it is important to reduce or eliminate the grain boundaries. Further work should contribute to reduce the grain boundaries in different perovskite materials, and even to fabricate single crystal perovskite solar cells. Besides, during the whole study of this thesis, one of the big issues is the reproducibility of the results, which consumes most of the research time. We find that the quality of perovskite precursor materials and the condition of fabrication or test environment greatly affect the final results. Therefore, to solve the reproducibility issue is also of high relevance for future research in perovskite photovoltaics.

Appendices

Appendix A

Figures

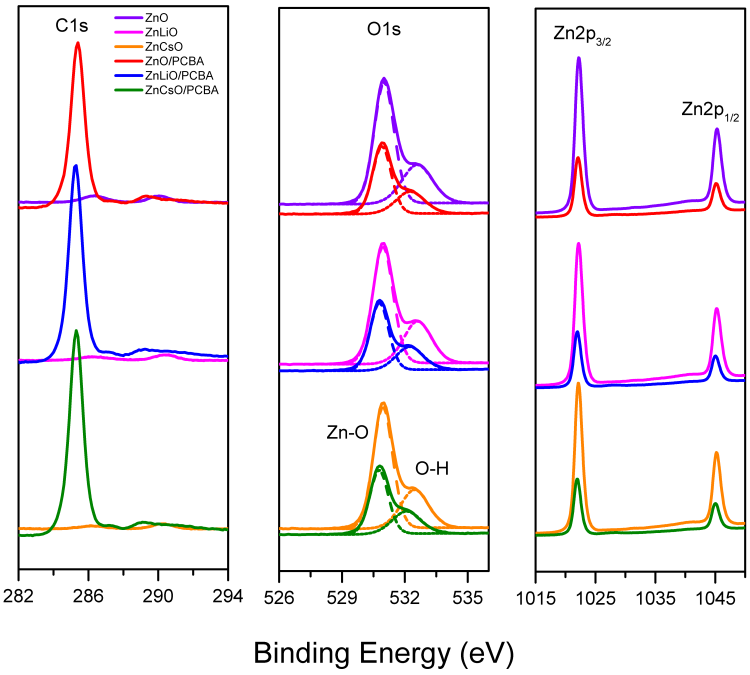

Figure A.1: *C1s*, *O1s* and *Zn2p* XPS spectra measured on *ZnO*, *ZnLiO*, *ZnCsO* and PCBA modified *ZnO*, *ZnLiO*, *ZnCsO*.

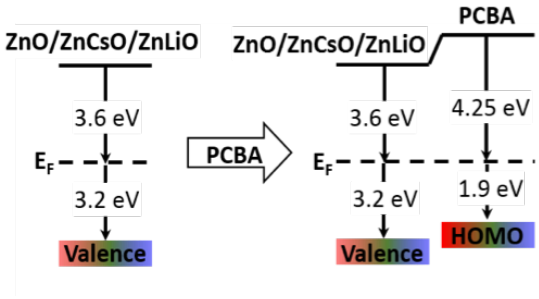

Figure A.2: Energy diagram summary of metal oxide and PCBA modified metal oxide layers.

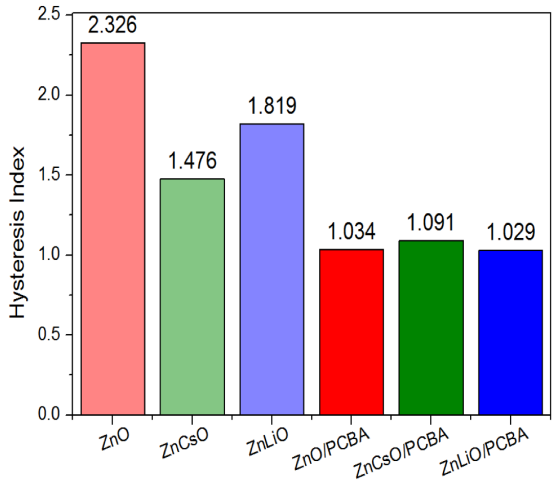

Figure A.3: Hysteresis index for devices with different ETLs based on $J-V$ results of Figure 4.7.

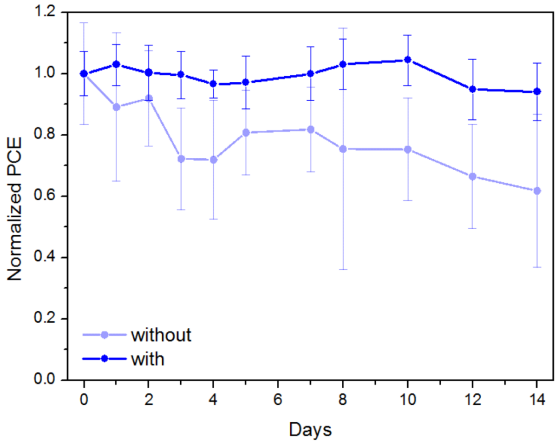

Figure A.4: *PCE* evolution of PCBA modified and bare Li doped ZnO devices. The devices were kept in air in the dark at room temperature (30% relative humidity) without encapsulation between measurements

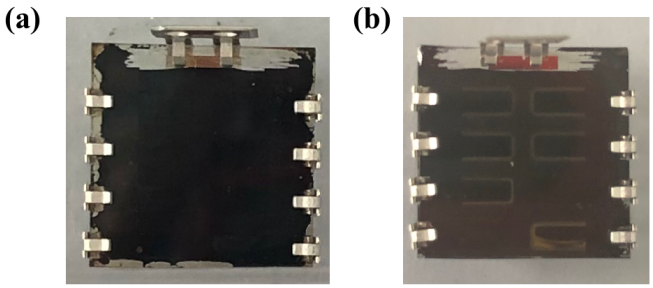

Figure A.5: Photos of photovoltaic devices (a) without iodide component and (b) with iodide component in π-PFEs as HBL after measuring under illumination.

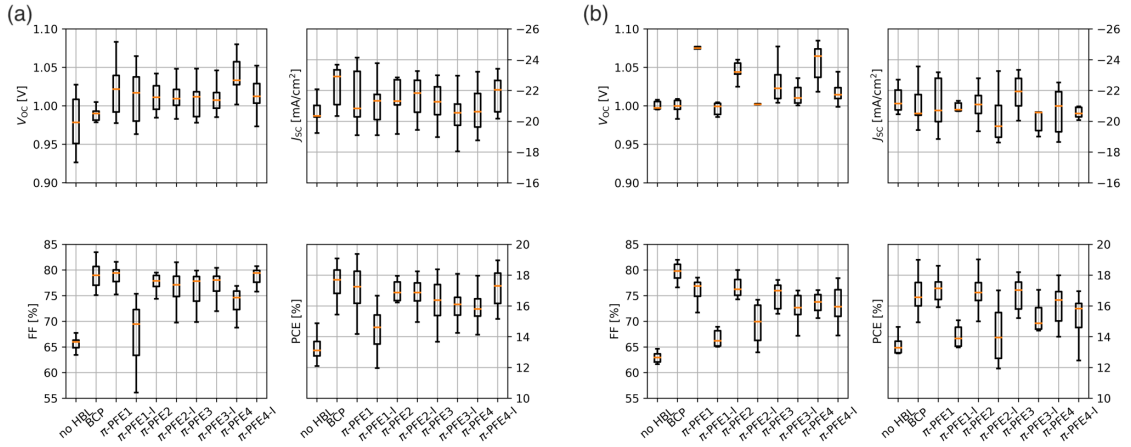

Figure A.6: Statistics of the photovoltaic performance with bare PCBM (no HBL), PCBM/BCP (BCP) and PCBM/π-PFEs for (a) the first measurement and (b) the second measurement.

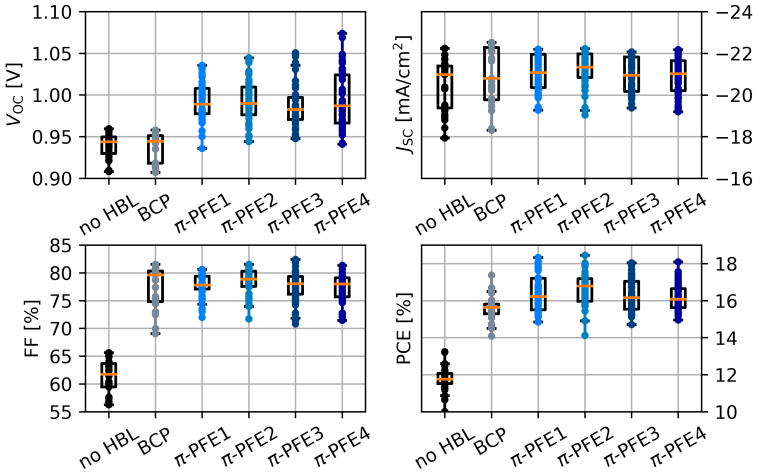

Figure A.7: Statistics of the photovoltaic performance of 258 $MAPbI_3$ devices with bare PCBM (no HBL), BCP as HBL and π-PFE1-4 as HBL.

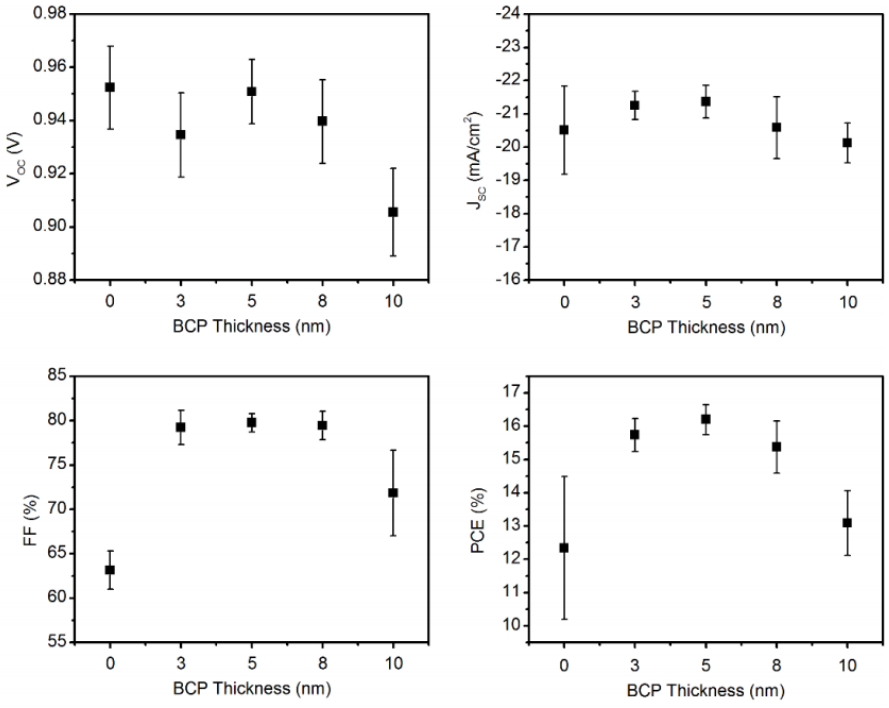

Figure A.8: Statistics of the photovoltaic performance of $MAPbI_3$ devices with different thickness of BCP.

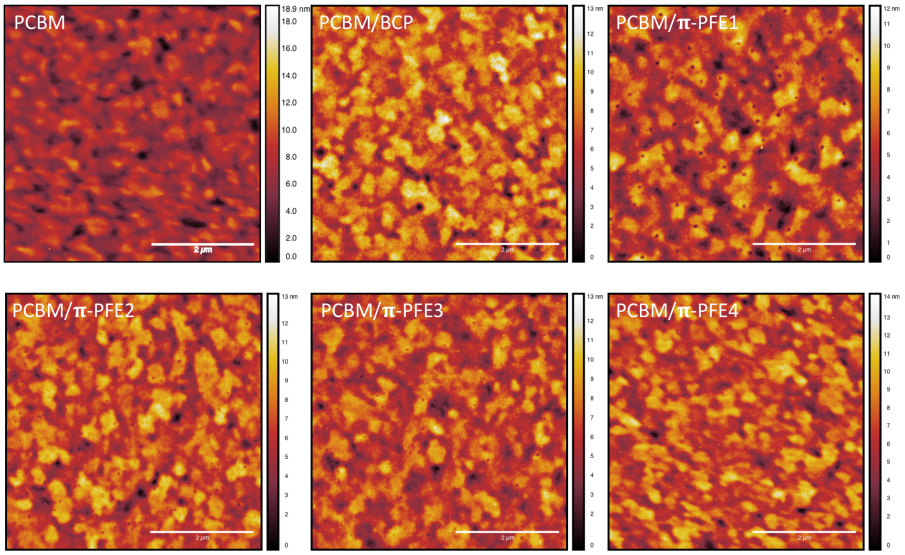

Figure A.9: AFM figures of bare PCBM, PCBM/BCP and PCBM/π-PFEs.

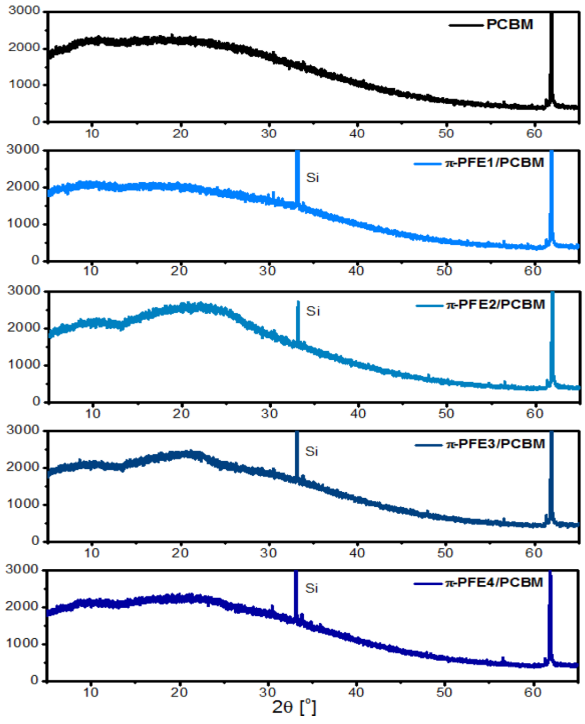

Figure A.10: The XRD measurements on PCBM and PCBM/π-PFE1-4 on silicon substrates.

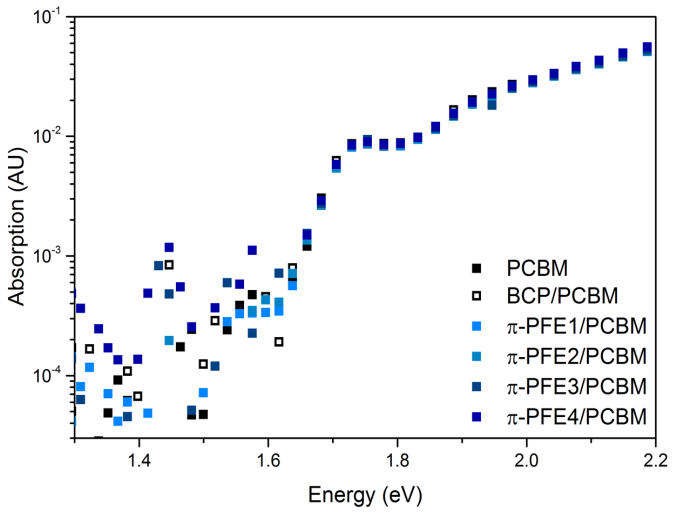

Figure A.11: Photothermal deflection spectroscopy measurements on PCBM, PCBM/BCP and PCBM/π-PFE1-4.

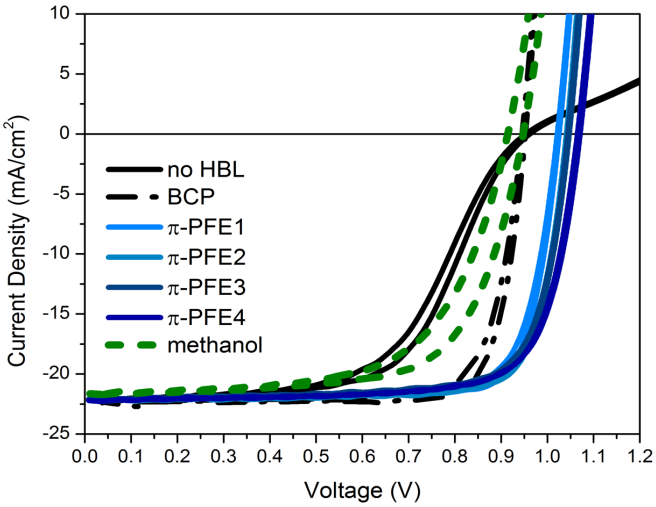

Figure A.12: J-V curves of devices with different π-PFEs as HBLs in the structure of ITO/m-PEDOT:PSS/$MAPbI_3$/PCBM/π-PFEs/Ag, where the reference devices are without a HBL, with a BCP HBL and methanol treatment.

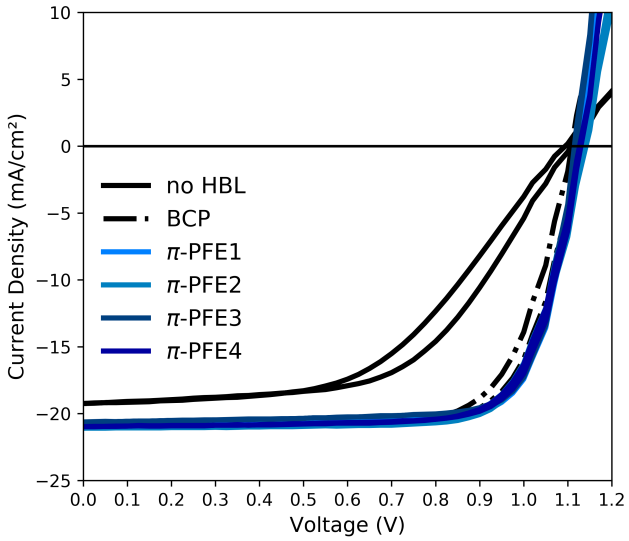

Figure A.13: J-V curves of devices with different π-PFEs as HBLs in the structure of ITO/PTAA/$MAPbI_3$/PCBM/π-PFEs/Ag, where the reference devices are without a HBL and with a BCP HBL.

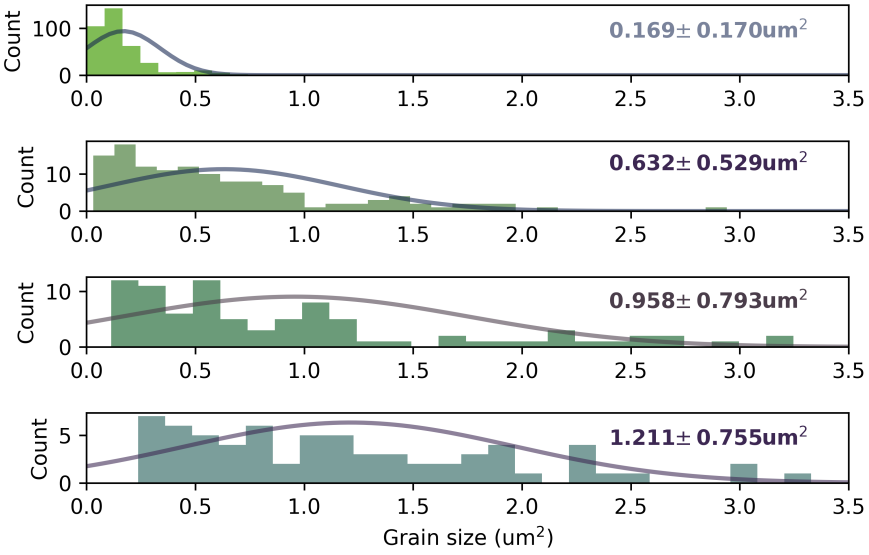

Figure A.14: Top to bottom: histograms of grain size analysis on glass with HPA/DMF ratios of 2‰, 4‰, 6‰and 8‰.

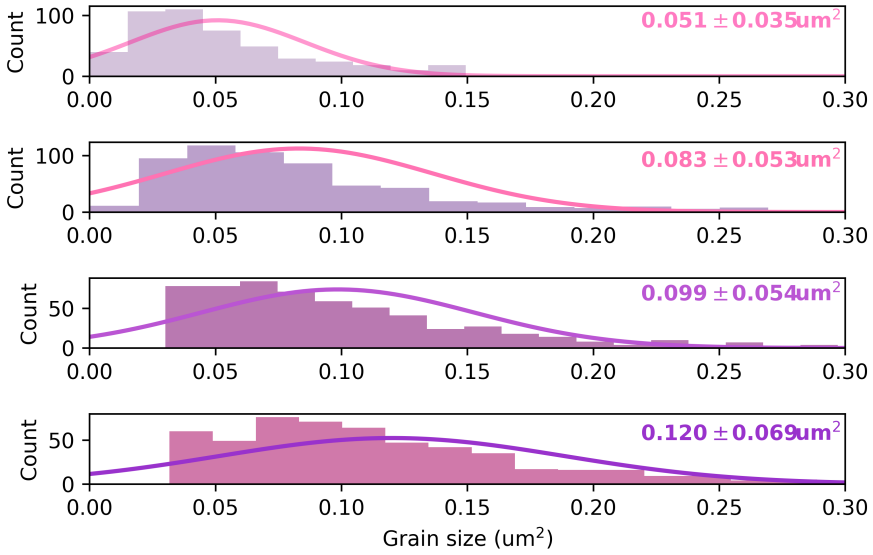

Figure A.15: Top to bottom: histograms of grain size analysis on PEDOT:PSS with HPA/DMF ratios of 2‰, 4‰, 6‰and 8‰.

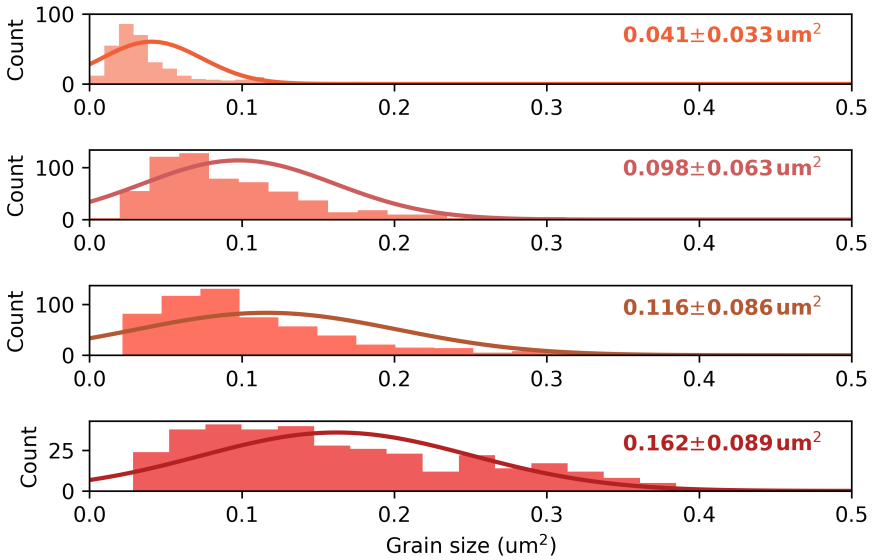

Figure A.16: Top to bottom: histograms of grain size analysis on m-PEDOT:PSS with HPA/DMF ratios of 2‰, 4‰, 6‰and 8‰.

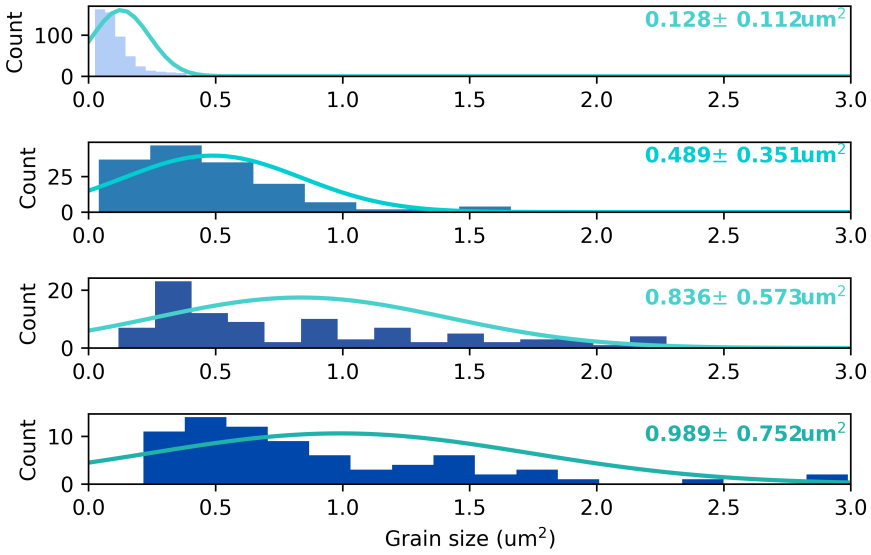

Figure A.17: Top to bottom: histograms of grain size analysis on m-PTAA with HPA/DMF ratios of 2‰, 4‰, 6‰and 8‰.

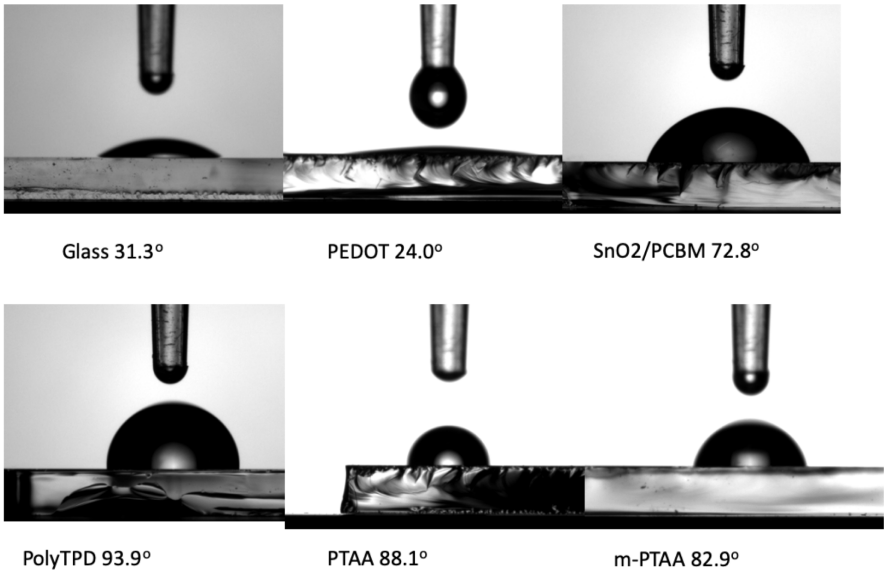

Figure A.18: contact angle measurement of water droplet on a variety of substrates.

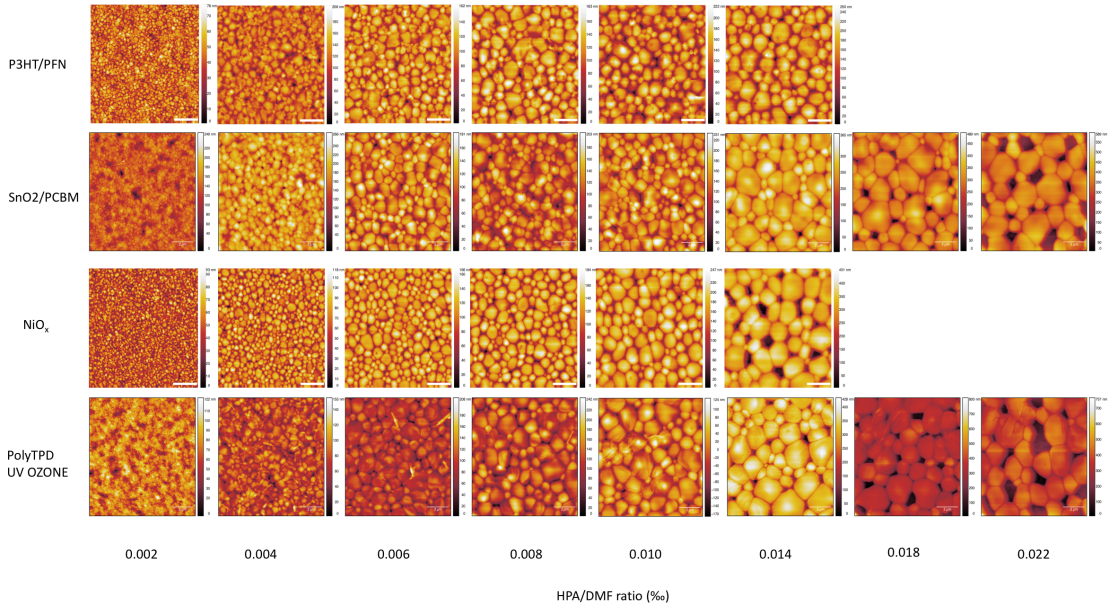

Figure A.19: AFM micrographs of perovskite formed with different amounts of HPA on diverse transport layers

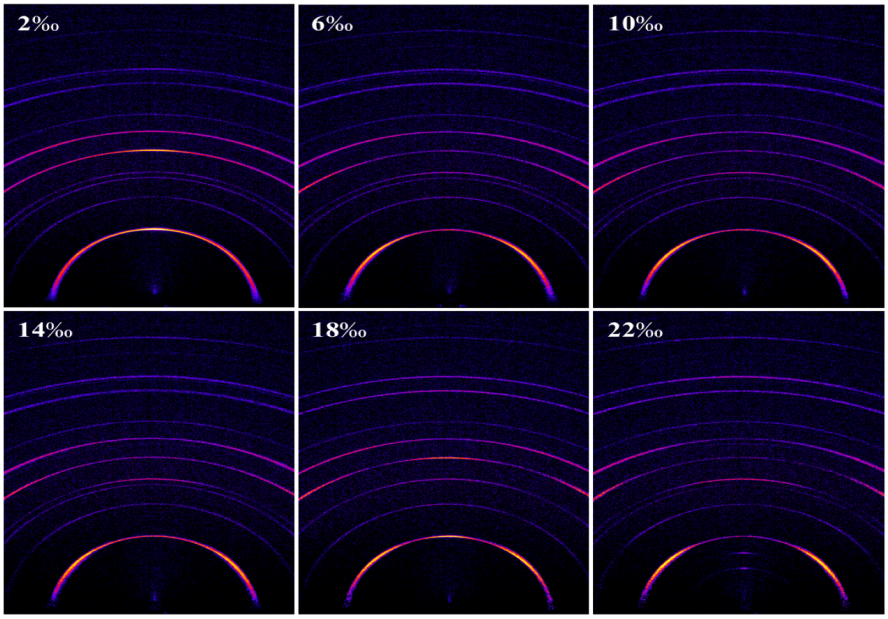

Figure A.20: 2D-diffraction maps (logarithmic intensity) for the polycrystalline $MAPbI_3$ films with increasing amounts of HPA in the precursor solution. All the films are of polycrystalline nature (Debye rings) but show variations in the preferred orientation.

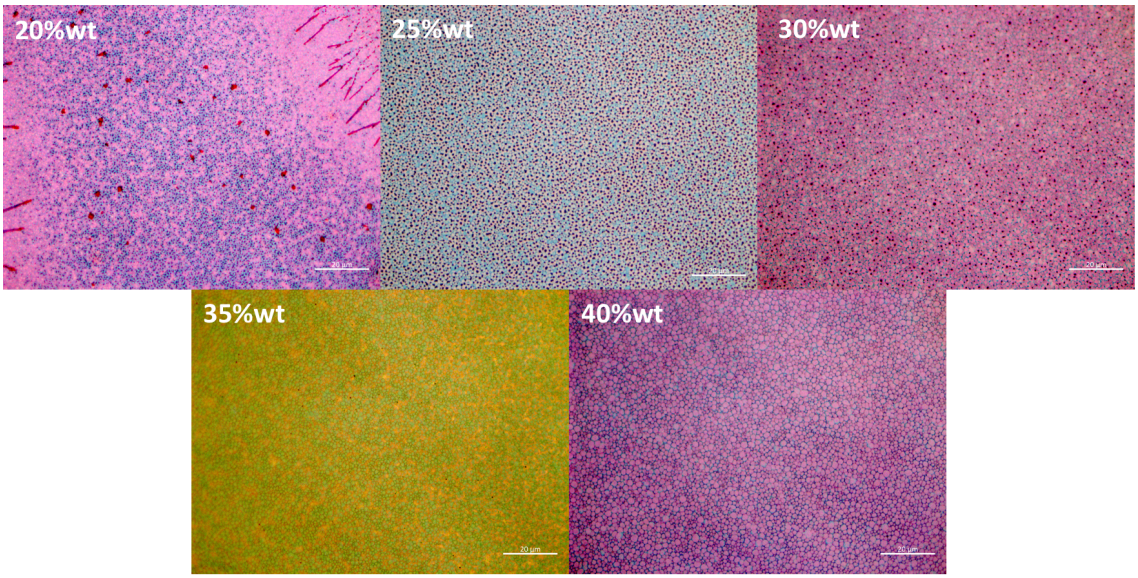

Figure A.21: Optical microscopy figures of perovskite with the same additive concentration (HPA/DMF=6‰) in 20%wt, 25%wt, 30%wt, 35%wt and 40%wt of perovskite precursor solution.

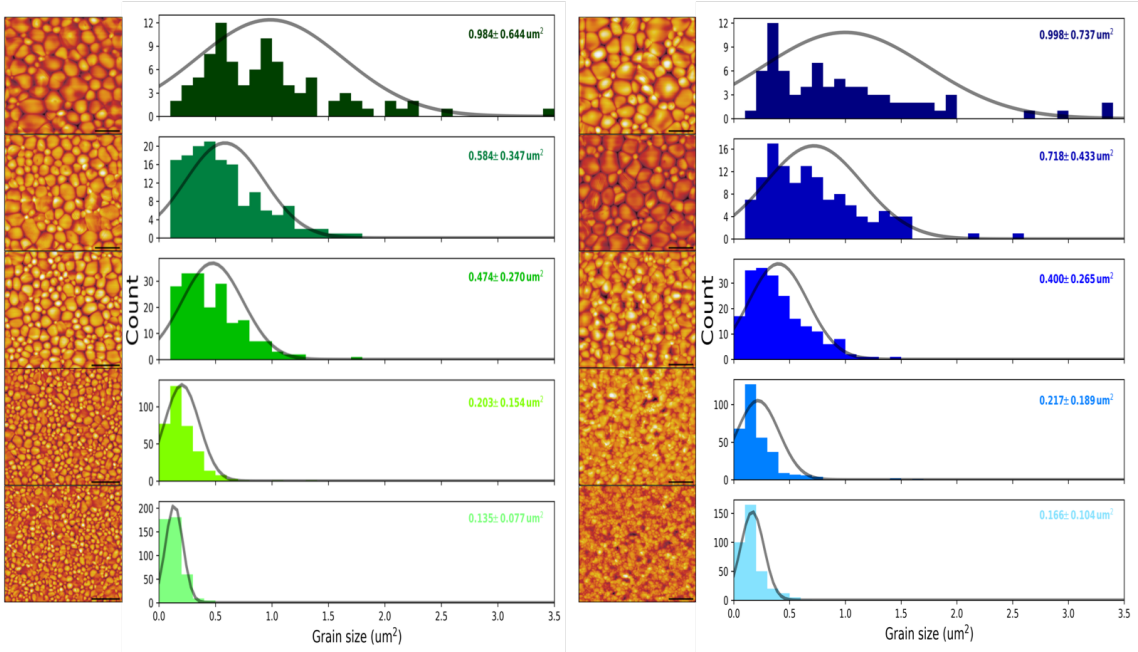

Figure A.22: AFM images and grain size distributions of grain size varying by (a) perovskite precursor concentration, from top to bottom is with precursor concentration of 40%, 35%, 30%, 25%, 20%, and (b) additive concentration, from top to bottom is the additive concentration of 8‰, 6‰, 4‰, 2.5‰, 1.5‰. The grain size was calculated by using software MIPAR.

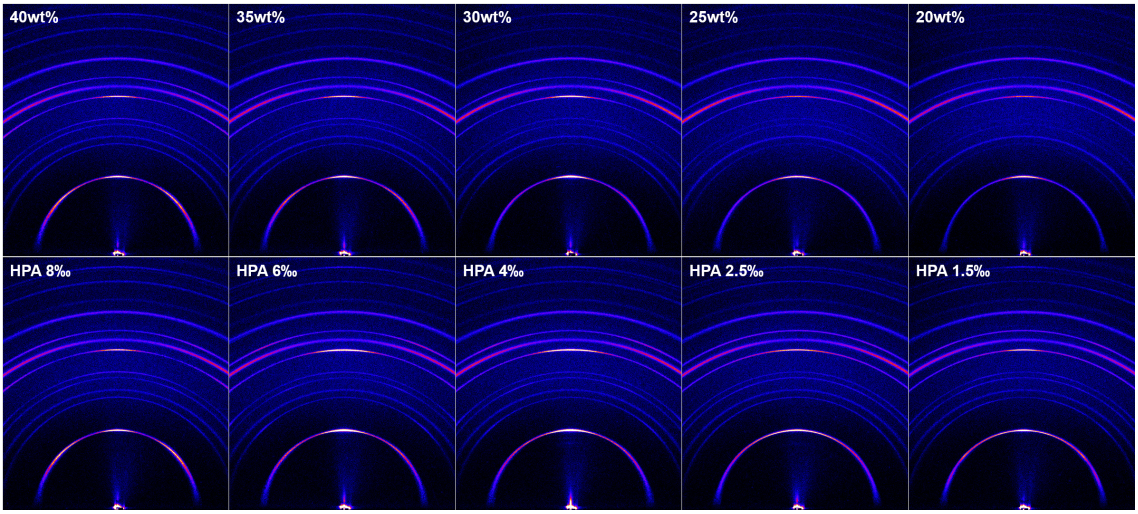

Figure A.23: 2D-diffraction maps (logarithmic intensity) of the perovskite films from type A and B on ITO/PTAA substrates.

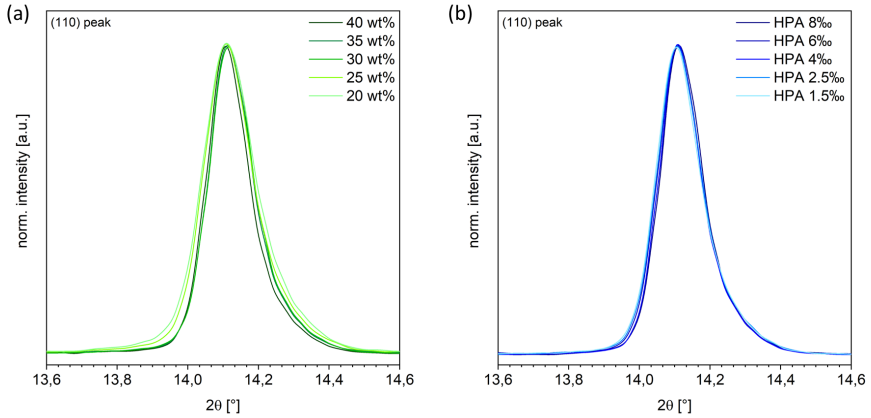

Figure A.24: XRD diffraction profile of (110) peak for type A (a) and type B (b).

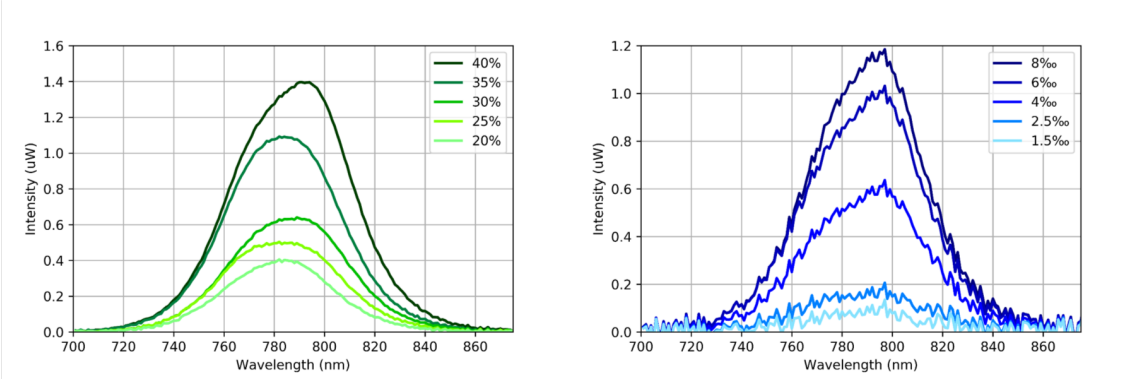

Figure A.25: Photoluminescence of perovskite with different grain size, the samples were fabricated by different methods, (a) varying perovskite concentration and (b) varying the additive concentration in a fixed perovskite concentration precursor.

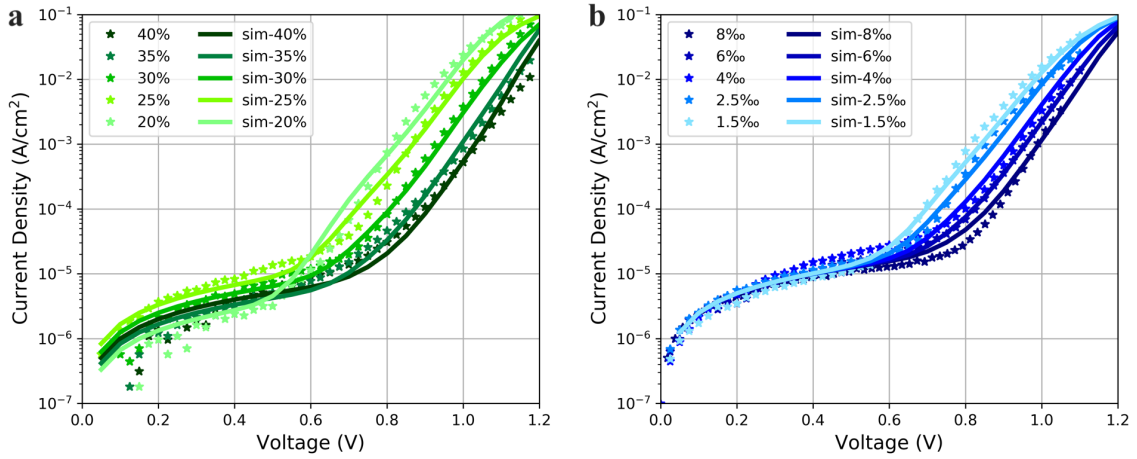

Figure A.26: Simulated dark $J-V$ curves with the experimental dark $J-V$ curves of perovskite films with different grain size, for (a) type A with unfixed layer thickness and (b) type B with fixed layer thickness.

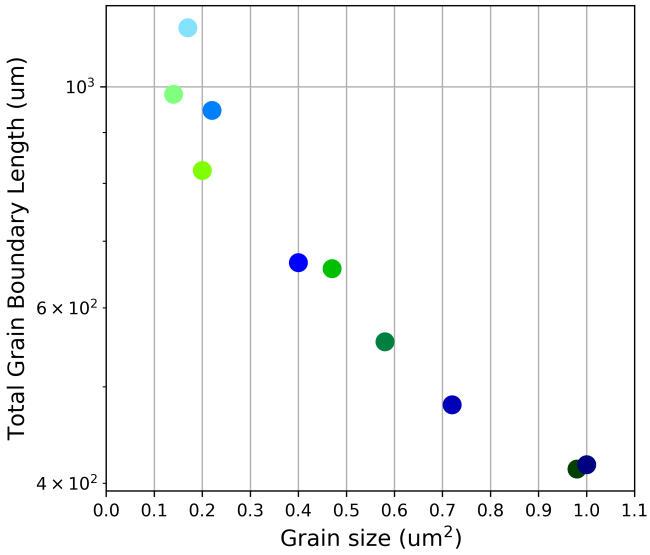

Figure A.27: The total length of the grain boundaries for each samples vs. the grain size. The length was estimated from Figure **??**.

Appendix B

Tables

ND number	Light intensity (mW/cm^2)
0.1	90
0.5	36.5
0.6	28.7
1	16.9
1.1	10.6
2	2

Table B.1: The filter OD number and its relative light intensity.

	RS V_{oc} (V)	FS V_{oc} (V)	RS J_{sc} (mA/cm^2)	FS J_{sc} (mA/cm^2)	RS FF (%)	FS FF (%)	RS PCE (%)	FS PCE (%)	R_s (Ω/cm^2)
ZnO/PCBA	1.04	1.04	-16.3	-16.3	78.8	73.9	13.4	12.6	3.5
ZnCsO/PCBA	1.05	1.06	-18.4	-18.4	77.2	77.2	14.9	14.0	2.9
ZnLiO/PCBA	1.03	1.02	-19.2	-19.2	82.1	79.1	16.2	15.5	2.6
ZnO	0.98	0.99	-4.80	-4.80	66.4	28.3	3.14	1.35	41
ZnCsO	1.00	1.00	-7.03	-7.03	57.8	39	4.06	2.75	23.5
ZnLiO	1.00	1.00	-6.77	-6.77	57.1	31.7	3.91	2.15	37.5

Table B.2: Photovoltaic parameters of the $J-V$ curves shown in Figure 4.7. RS and FS represent the scanning direction from V_{oc} to J_{sc} and from J_{sc} to V_{oc}, respectively. R_s is the series resistance of the devices.

	PLQE (%)	Transit time (μs)
ZnO/PCBA	0.77	0.95
ZnCsO/PCBA	0.53	0.54
ZnLiO/PCBA	0.46	0.79
ZnO	1.86	1.90
ZnCsO	1.29	1.57
ZnLiO	1.23	1.86

Table B.3: A summary of photoluminescence quantum efficiency of perovskite films deposited on doped and undoped *ZnO* with and without PCBA modification, as well as the transit time extracted from transient photocurrent measurements based on Figure 4.8

	Electron mobility (m^2/Vs)
PCBM	$5.2x10^{-4}$
PCBM/BCP	$1.0x10^{-3}$
PCBM/π-PFE1	$3.7x10^{-3}$
PCBM/π-PFE2	$4.9x10^{-3}$
PCBM/π-PFE3	$4.2x10^{-3}$
PCBM/π-PFE4	$9.0x10^{-3}$

Table B.4: Electron mobility values calculated from the $J-V$ curves in Figure 5.4(c)

	RS V_{oc} (V)	FS V_{oc} (V)	RS J_{sc} (mA/cm^2)	FS J_{sc} (mA/cm^2)	RS *FF* (%)	FS *FF* (%)	RS *PCE* (%)	FS *PCE* (%)
PCBM	1.11	1.10	-19.24	-19.24	56.11	51.58	11.98	10.87
BCP	1.13	1.11	-20.86	-20.86	74.96	73.14	17.62	16.96
π-PFE1	1.13	1.12	-20.93	-20.93	77.14	76.21	18.20	17.90
π-PFE2	1.14	1.14	-21.09	-21.09	75.54	74.02	18.21	17.78
π-PFE3	1.12	1.12	-20.62	-20.62	77.92	77.29	18.04	17.83
π-PFE4	1.13	1.13	-20.98	-20.98	75.73	75.03	18.00	17.80

Table B.5: Photovoltaic parameters of the $J-V$ curves shown in Figure A.13. RS and FS represent the scanning direction from V_{oc} to J_{sc} and from J_{sc} to V_{oc}, respectively.

	Perovskite	PCBM	PCBM/BCP	PCBM/π-PFE
μ_e=μ_h (cm^2/Vs)	2	10^{-3}	10^{-3}	$5x10^{-3}$
LUMO Effective DOS (cm^{-3})	$7x10^{18}$	10^{21}	10^{21}	10^{21}
HOMO Effective DOS ($cm^{-}3$)	$2.5x10^{18}$	10^{21}	10^{21}	10^{21}
Bimolicular coefficient (cm^3/s)	10^{-10}	Langevin	Langevin	Langevin
ϵ	50	3	3	3
Length (nm)	250	50	50	50
Mobile ions	positive only			
Ions density (cm^{-3})	$5x10^{17}$			

Table B.6: Material parameters used for the device simulation.

Label	40%	35%	30%	25%	20%
Concentration (%wt)	40	35	30	25	20
HPA/DMF (μl/μl)	0.0080	0.0055	0.0045	0.0030	0.0024

Table B.7: List of perovskite precursor concentration and the optimal HPA/DMF volume ratio in type A.

Label	**RS** V_{oc} **(V)**	**FS** V_{oc} **(V)**	**RS** J_{sc} **(mA/cm^2)**	**FS** J_{sc} **(mA/cm^2)**	**RS** *FF* **(%)**	**FS** *FF* **(%)**	**RS** *PCE* **(%)**	**FS** *PCE* **(%)**
20%	0.99	1.00	-14.49	-14.49	79.15	78.21	11.38	11.29
25%	1.03	1.03	-18.75	-18.75	81.83	81.76	15.76	15.82
30%	1.08	1.08	-19.85	-19.85	81.63	81.78	17.53	17.57
35%	1.12	1.12	-20.29	-20.29	80.93	81.41	18.33	18.49
40%	1.16	1.17	-20.90	-20.90	79.62	80.12	19.38	19.55

Table B.8: Photovoltaic parameters of the $J-V$ curves shown in Figure 6.5(a) (type A). RS and FS represent the scanning direction from V_{oc} to J_{sc} and from J_{sc} to V_{oc}, respectively.

Label	**RS** V_{oc} **(V)**	**FS** V_{oc} **(V)**	**RS** J_{sc} **(mA/cm^2)**	**FS** J_{sc} **(mA/cm^2)**	**RS** *FF* **(%)**	**FS** *FF* **(%)**	**RS** *PCE* **(%)**	**FS** *PCE* **(%)**
1.5‰	0.99	0.99	-19.91	-19.91	74.17	75.84	14.67	14.99
2.5‰	1.03	1.04	-20.34	-20.34	79.40	80.04	16.63	16.85
4‰	1.08	1.08	-20.56	-20.56	78.72	78.27	17.49	17.44
6‰	1.13	1.13	-20.49	-20.49	80.32	80.68	18.55	18.75
8‰	1.17	1.18	-20.59	-20.59	80.32	80.97	19.37	19.61

Table B.9: Photovoltaic parameters of the $J-V$ curves shown in Figure 6.5(b) (type B). RS and FS represent the scanning direction from V_{oc} to J_{sc} and from J_{sc} to V_{oc}, respectively.

	Perovskite (Type A)	Perovskite (Type B)	Extraction Layers
μ_e=μ_h (cm^2/Vs)	5	5	10^{-3}
LUMO Effective DOS (cm^{-3})	7x10^{18}	7^{18}	10^{21}
HOMO Effective DOS (cm$^-$3)	2.5x10^{18}	2.5x10^{18}	10^{21}
Bimolicular coefficient (cm^3/s)	10^{-10}	10^{-10}	Langevin
ϵ	30	30	3
Thickness (nm)	260	75,105,150,190,260	50
Mobile ions	-	-	-
Ions density (cm^{-3})	0	0	0

Table B.10: Material parameters used for the device simulation.

References

1. BP. Statistical Review of World Energy globally consistent data on world energy markets (2020).
2. National Renewable Energy Laboratory: Best Research-Cell Efficiency Chart (2020).
3. Kim, H.-S., Lee, C.-R., Im, J.-H., Lee, K.-B., Moehl, T., Marchioro, A., Moon, S.-J., Humphry-Baker, R., Yum, J.-H., Moser, J. E., Grätzel, M. & Park, N.-G. Lead Iodide Perovskite Sensitized All-Solid-State Submicron Thin Film Mesoscopic Solar Cell with Efficiency Exceeding 9%. *Scientific Reports* **2,** 591 (2012).
4. Lee, M. M., Teuscher, J., Miyasaka, T., Murakami, T. N. & Snaith, H. J. Efficient Hybrid Solar Cells Based on Meso-Superstructured Organometal Halide Perovskites. *Science* **338,** 643 (2012).
5. Tan, H., Jain, A., Voznyy, O., Lan, X., García de Arquer, F. P., Fan, J. Z., Quintero-Bermudez, R., Yuan, M., Zhang, B., Zhao, Y., Fan, F., Li, P., Quan, L. N., Zhao, Y., Lu, Z.-H., Yang, Z., Hoogland, S. & Sargent, E. H. Efficient and stable solution-processed planar perovskite solar cells via contact passivation. *Science* **355,** 722 (2017).
6. Shao, S. & Loi, M. A. The Role of the Interfaces in Perovskite Solar Cells. *Advanced Materials Interfaces* **7,** 1901469 (2020).
7. Lee, J.-W., Bae, S.-H., De Marco, N., Hsieh, Y.-T., Dai, Z. & Yang, Y. The role of grain boundaries in perovskite solar cells. *Materials Today Energy* **7,** 149–160 (2018).
8. Castro-Méndez, A.-F., Hidalgo, J. & Correa-Baena, J.-P. The Role of Grain Boundaries in Perovskite Solar Cells. *Advanced Energy Materials* **9,** 1901489 (2019).
9. Goldschmidt, V. M. Die Gesetze der Krystallochemie. *Naturwissenschaften* **14,** 477–485 (1926).
10. Glazer, A. M. The classification of tilted octahedra in perovskites. *Acta Crystallographica Section B* **28,** 3384–3392 (1972).
11. Stoumpos, C. C. & Kanatzidis, M. G. The Renaissance of Halide Perovskites and Their Evolution as Emerging Semiconductors. *Accounts of Chemical Research* **48,** 2791–2802 (2015).

12. Poglitsch, A. & Weber, D. Dynamic disorder in methylammoniumtrihalogenoplumbates (II) observed by millimeter-wave spectroscopy. *The Journal of Chemical Physics* **87,** 6373–6378 (1987).

13. Quarti, C., Mosconi, E., Ball, J. M., D'Innocenzo, V., Tao, C., Pathak, S., Snaith, H. J., Petrozza, A. & De Angelis, F. Structural and optical properties of methylammonium lead iodide across the tetragonal to cubic phase transition: Implications for perovskite solar cells. *Energy & Environmental Science* **9,** 155–163 (2016).

14. Dar, M. I., Jacopin, G., Meloni, S., Mattoni, A., Arora, N., Boziki, A., Zakeeruddin, S. M., Rothlisberger, U. & Grätzel, M. Origin of unusual bandgap shift and dual emission in organic-inorganic lead halide perovskites. *Science Advances* **2,** 1601156 (2016).

15. Zhang, H., Qiao, X., Shen, Y., Moehl, T., Zakeeruddin, S. M., Grätzel, M. & Wang, M. Photovoltaic behaviour of lead methylammonium triiodide perovskite solar cells down to 80 K. *Journal of Materials Chemistry A* **3,** 11762–11767 (2015).

16. Pellet, N., Gao, P., Gregori, G., Yang, T.-Y., Nazeeruddin, M. K., Maier, J. & Grätzel, M. Mixed-Organic-Cation Perovskite Photovoltaics for Enhanced Solar-Light Harvesting. *Angewandte Chemie International Edition* **53,** 3151–3157 (2014).

17. Li, Z., Yang, M., Park, J. S., Wei, S. H., Berry, J. J. & Zhu, K. Stabilizing Perovskite Structures by Tuning Tolerance Factor: Formation of Formamidinium and Cesium Lead Iodide Solid-State Alloys. *Chemistry of Materials* **28,** 284–292 (2016).

18. Kim, M., Kim, G.-H., Lee, T. K., Choi, I. W., Choi, H. W., Jo, Y., Yoon, Y. J., Kim, J. W., Lee, J., Huh, D., Lee, H., Kwak, S. K., Kim, J. Y. & Kim, D. S. Methylammonium Chloride Induces Intermediate Phase Stabilization for Efficient Perovskite Solar Cells. *Joule* **3,** 2179–2192 (2019).

19. Smith, I. C., Hoke, E. T., Solis-Ibarra, D., McGehee, M. D. & Karunadasa, H. I. A Layered Hybrid Perovskite Solar-Cell Absorber with Enhanced Moisture Stability. *Angewandte Chemie International Edition* **53,** 11232–11235 (2014).

20. Chen, Y., Sun, Y., Peng, J., Tang, J., Zheng, K. & Liang, Z. 2D Ruddlesden–Popper Perovskites for Optoelectronics. *Advanced Materials* **30,** 1703487 (2018).

21. Lan, C., Zhou, Z., Wei, R. & Ho, J. C. Two-dimensional perovskite materials: From synthesis to energy-related applications. *Materials Today Energy* **11,** 61–82 (2019).

22. Ren, H., Yu, S., Chao, L., Xia, Y., Sun, Y., Zuo, S., Li, F., Niu, T., Yang, Y., Ju, H., Li, B., Du, H., Gao, X., Zhang, J., Wang, J., Zhang, L., Chen, Y. & Huang, W. Efficient and stable Ruddlesden–Popper perovskite solar cell with tailored interlayer molecular interaction. *Nature Photonics* **14,** 154–163 (2020).

23. Atourki, L., Vega, E., Marí, B., Mollar, M., Ait Ahsaine, H., Bouabid, K. & Ihlal, A. Role of the chemical substitution on the structural and luminescence properties of the mixed halide perovskite thin MAPbI3xBrx (0x1) films. *Applied Surface Science* **371,** 112–117 (2016).

24. Eperon, G. E., Stranks, S. D., Menelaou, C., Johnston, M. B., Herz, L. M. & Snaith, H. J. Formamidinium lead trihalide: a broadly tunable perovskite for efficient planar heterojunction solar cells. *Energy & Environmental Science* **7,** 982–988 (2014).

25. Saliba, M., Correa-Baena, J.-P., Grätzel, M., Hagfeldt, A. & Abate, A. Perovskite Solar Cells: From the Atomic Level to Film Quality and Device Performance. *Angewandte Chemie International Edition* **57,** 2554–2569 (2018).

26. Sun, J., Wu, J., Tong, X., Lin, F., Wang, Y. & Wang, Z. M. Organic/Inorganic Metal Halide Perovskite Optoelectronic Devices beyond Solar Cells. *Advanced Science* **5,** 1700780 (2018).

27. Shockley, W. The theory of p-n junctions in semiconductors and p-n junction transistors. *The Bell System Technical Journal* **28,** 435–489 (1949).

28. Jena, A. K., Kulkarni, A. & Miyasaka, T. Halide Perovskite Photovoltaics: Background, Status, and Future Prospects. *Chemical Reviews* **119,** 3036–3103 (2019).

29. Miyata, A., Mitioglu, A., Plochocka, P., Portugall, O., Wang, J. T. W., Stranks, S. D., Snaith, H. J. & Nicholas, R. J. Direct measurement of the exciton binding energy and effective masses for charge carriers in organic-inorganic tri-halide perovskites. *Nature Physics* **11,** 582–587 (2015).

30. Giorgi, G., Fujisawa, J.-I., Segawa, H. & Yamashita, K. Small Photocarrier Effective Masses Featuring Ambipolar Transport in Methylammonium Lead Iodide Perovskite: A Density Functional Analysis. *The Journal of Physical Chemistry Letters* **4,** 4213–4216 (2013).

31. Xing, G., Mathews, N., Sun, S., Lim, S. S., Lam, Y. M., Grätzel, M., Mhaisalkar, S. & Sum, T. C. Long-Range Balanced Electron- and Hole-Transport Lengths in Organic-Inorganic CH3NH3PbI3. *Science* **342,** 344–347 (2013).

32. Stranks, S. D., Eperon, G. E., Grancini, G., Menelaou, C., Alcocer, M. J. P., Leijtens, T., Herz, L. M., Petrozza, A. & Snaith, H. J. Electron-Hole Diffusion Lengths Exceeding 1 Micrometer in an Organometal Trihalide Perovskite Absorber. *Science* **342,** 341–344 (2013).

33. Dong, Q., Fang, Y., Shao, Y., Mulligan, P., Qiu, J., Cao, L. & Huang, J. Electron-hole diffusion lengths > 175 μm in solution-grown CH3NH3PbI3 single crystals. *Science* **347,** 967–970 (2015).

34. Wehrenfennig, C., Eperon, G. E., Johnston, M. B., Snaith, H. J. & Herz, L. M. High charge carrier mobilities and lifetimes in organolead trihalide perovskites. *Advanced Materials* **26,** 1584–1589 (2014).

35. Yin, W.-J., Shi, T. & Yan, Y. Unusual defect physics in CH3NH3PbI3 perovskite solar cell absorber. *Applied Physics Letters* **104,** 063903 (2014).

36. Ran, C., Xu, J., Gao, W., Huang, C. & Dou, S. Defects in metal triiodide perovskite materials towards high-performance solar cells: origin, impact, characterization, and engineering. *Chemistry Society Review* **47,** 4581–4610 (2018).

37. Shockley, W. & Read, W. T. Statistics of the Recombinations of Holes and Electrons. *Physical Review* **87,** 835–842 (1952).

38. Tress, W. Perovskite Solar Cells on the Way to Their Radiative Efficiency Limit - Insights Into a Success Story of High Open-Circuit Voltage and Low Recombination. *Advanced Energy Materials* **7,** 1602358 (2017).

39. Dunfield, S. P., Bliss, L., Zhang, F., Luther, J. M., Zhu, K., Hest, M. F. A. M., Reese, M. O. & Berry, J. J. From Defects to Degradation: A Mechanistic Understanding of Degradation in Perovskite Solar Cell Devices and Modules. *Advanced Energy Materials,* 1904054 (2020).

40. Sun, Q., Fassl, P., Becker-Koch, D., Bausch, A., Rivkin, B., Bai, S., Hopkinson, P. E., Snaith, H. J. & Vaynzof, Y. Role of Microstructure in Oxygen Induced Photodegradation of Methylammonium Lead Triiodide Perovskite Films. *Advanced Energy Materials* **7,** 1700977 (2017).

41. Eames, C., Frost, J. M., Barnes, P. R., O'Regan, B. C., Walsh, A. & Islam, M. S. Ionic transport in hybrid lead iodide perovskite solar cells. *Nature Communications* **6,** 1–8 (2015).

42. Mizusaki, J., Arai, K. & Fueki, K. Ionic conduction of the perovskite-type halides. *Solid State Ionics* **11,** 203–211 (1983).

43. Correa-Baena, J.-P., Anaya, M., Lozano, G., Tress, W., Domanski, K., Saliba, M., Matsui, T., Jacobsson, T. J., Calvo, M. E., Abate, A., Grätzel, M., Míguez, H. & Hagfeldt, A. Unbroken Perovskite: Interplay of Morphology, Electro-optical Properties, and Ionic Movement. *Advanced Materials* **28,** 5031–5037 (2016).

44. Adhyaksa, G. W. P., Brittman, S., Āboliņš, H., Lof, A., Li, X., Keelor, J. D., Luo, Y., Duevski, T., Heeren, R. M. A., Ellis, S. R., Fenning, D. P. & Garnett, E. C. Understanding Detrimental and Beneficial Grain Boundary Effects in Halide Perovskites. *Advanced Materials* **30,** 1804792 (2018).

45. Fassl, P., Lami, V., Bausch, A., Wang, Z., Klug, M. T., Snaith, H. J. & Vaynzof, Y. Fractional deviations in precursor stoichiometry dictate the properties, performance and stability of perovskite photovoltaic devices. *Energy & Environmental Science* **11,** 3380–3391 (2018).

46. Wu, T., Wang, Y., Li, X., Wu, Y., Meng, X., Cui, D., Yang, X. & Han, L. Efficient Defect Passivation for Perovskite Solar Cells by Controlling the Electron Density Distribution of Donor-π-Acceptor Molecules. *Advanced Energy Materials* **9,** 1803766 (2019).

47. Saliba, M., Matsui, T., Seo, J.-Y., Domanski, K., Correa-Baena, J.-P., Nazeeruddin, M. K., Zakeeruddin, S. M., Tress, W., Abate, A., Hagfeldt, A. & Grätzel, M. Cesium-containing triple cation perovskite solar cells: improved stability, reproducibility and high efficiency. *Energy & Environmental Science* **9,** 1989–1997 (2016).

48. Hadadian, M., Correa-Baena, J. P., Goharshadi, E. K., Ummadisingu, A., Seo, J. Y., Luo, J., Gholipour, S., Zakeeruddin, S. M., Saliba, M., Abate, A., Gr??tzel, M. & Hagfeldt, A. Enhancing Efficiency of Perovskite Solar Cells via N-doped Graphene: Crystal Modification and Surface Passivation. *Advanced Materials* **28,** 8681–8686 (2016).

49. Liang, P.-W., Liao, C.-Y., Chueh, C.-C., Zuo, F., Williams, S. T., Xin, X.-K., Lin, J. & Jen, A. K.-Y. Additive Enhanced Crystallization of Solution-Processed Perovskite for Highly Efficient Planar-Heterojunction Solar Cells. *Advanced Materials* **26,** 3748–3754 (2014).

50. Tavakoli, M. M., Yadav, P., Prochowicz, D., Sponseller, M., Osherov, A., Bulović, V. & Kong, J. Controllable Perovskite Crystallization via Antisolvent Technique Using Chloride Additives for Highly Efficient Planar Perovskite Solar Cells. *Advanced Energy Materials* **9,** 1803587 (2019).

51. Huang, F., Dkhissi, Y., Huang, W., Xiao, M., Benesperi, I., Rubanov, S., Zhu, Y., Lin, X., Jiang, L., Zhou, Y., Gray-Weale, A., Etheridge, J., McNeill, C. R., Caruso, R. A., Bach, U., Spiccia, L. & Cheng, Y. B. Gas-assisted preparation of lead iodide perovskite films consisting of a monolayer of single crystalline grains for high efficiency planar solar cells. *Nano Energy* **10,** 10–18 (2014).

52. Chen, Q., Zhou, H., Hong, Z., Luo, S., Duan, H.-S., Wang, H.-H., Liu, Y., Li, G. & Yang, Y. Planar Heterojunction Perovskite Solar Cells via Vapor-Assisted Solution Process. *Journal of the American Chemical Society* **136,** 622–625 (2014).

53. Jiang, Q., Zhao, Y., Zhang, X., Yang, X., Chen, Y., Chu, Z., Ye, Q., Li, X., Yin, Z. & You, J. Surface passivation of perovskite film for efficient solar cells. *Nature Photonics* **13,** 460–466 (2019).

54. Wang, R., Xue, J., Wang, K. L., Wang, Z. K., Luo, Y., Fenning, D., Xu, G., Nuryyeva, S., Huang, T., Zhao, Y., Yang, J. L., Zhu, J., Wang, M., Tan, S., Yavuz, I., Houk, K. N. & Yang, Y. Constructive molecular configurations for surface-defect passivation of perovskite photovoltaics. *Science* **366,** 1509–1513 (2019).

55. Edri, E., Kirmayer, S., Mukhopadhyay, S., Gartsman, K., Hodes, G. & Cahen, D. Elucidating the charge carrier separation and working mechanism of CH 3 NH 3 PbI 3-x Cl x perovskite solar cells. *Nature Communications* **5,** 1–8 (2014).

56. Manser, J. S. & Kamat, P. V. Band filling with free charge carriers in organometal halide perovskites. *Nature Photonics* **8,** 737–743 (2014).

57. Snaith, H. J., Abate, A., Ball, J. M., Eperon, G. E., Leijtens, T., Noel, N. K., Stranks, S. D., Wang, J. T.-W., Wojciechowski, K. & Zhang, W. Anomalous Hysteresis in Perovskite Solar Cells. *The Journal of Physical Chemistry Letters* **5,** 1511–1515 (2014).

58. Yang, T.-Y., Gregori, G., Pellet, N., Grätzel, M. & Maier, J. The Significance of Ion Conduction in a Hybrid Organic–Inorganic Lead-Iodide-Based Perovskite Photosensitizer. *Angewandte Chemie International Edition* **54,** 7905–7910 (2015).

59. Li, C., Guerrero, A., Zhong, Y., Gräser, A., Luna, C. A. M., Köhler, J., Bisquert, J., Hildner, R. & Huettner, S. Real-Time Observation of Iodide Ion Migration in Methylammonium Lead Halide Perovskites. *Small* **13,** 1701711 (2017).

60. Li, C., Guerrero, A., Huettner, S. & Bisquert, J. Unravelling the role of vacancies in lead halide perovskite through electrical switching of photoluminescence. *Nature Communications* **9,** 1–8 (2018).

61. Li, C., Tscheuschner, S., Paulus, F., Hopkinson, P. E., Kießling, J., Köhler, A., Vaynzof, Y. & Huettner, S. Iodine Migration and its Effect on Hysteresis in Perovskite Solar Cells. *Advanced Materials* **28,** 2446–2454 (2016).

62. Park, N.-G., Grätzel, M., Miyasaka, T., Zhu, K. & Emery, K. Towards stable and commercially available perovskite solar cells. *Nature Energy* **1,** 16152 (2016).

63. Kang, D. & Park, N. On the Current–Voltage Hysteresis in Perovskite Solar Cells: Dependence on Perovskite Composition and Methods to Remove Hysteresis. *Advanced Materials* **31,** 1805214 (2019).

64. Chen, R., Cao, J., Duan, Y., Hui, Y., Chuong, T. T., Ou, D., Han, F., Cheng, F., Huang, X., Wu, B. & Zheng, N. High-Efficiency, Hysteresis-Less, UV-Stable Perovskite Solar Cells with Cascade ZnO–ZnS Electron Transport Layer. *Journal of the American Chemical Society* **141,** 541–547 (2019).

65. Lei, Y., Gu, L., He, W., Jia, Z., Yang, X., Jia, H. & Zheng, Z. Intrinsic charge carrier dynamics and device stability of perovskite/ZnO mesostructured solar cells in moisture. *Journal of Materials Chemistry A* **4,** 5474–5481 (2016).

66. Jiang, Q., Zhang, L., Wang, H., Yang, X., Meng, J., Liu, H., Yin, Z., Wu, J., Zhang, X. & You, J. Enhanced electron extraction using SnO2 for high-efficiency planar-structure HC(NH2)2PbI3-based perovskite solar cells. *Nature Energy* **2,** 16177 (2016).

67. Wang, J. T. W., Ball, J. M., Barea, E. M., Abate, A., Alexander-Webber, J. A., Huang, J., Saliba, M., Mora-Sero, I., Bisquert, J., Snaith, H. J. & Nicholas, R. J. Low-temperature processed electron collection layers of graphene/TiO 2 nanocomposites in thin film perovskite solar cells. *Nano Letters* **14,** 724–730 (2014).

68. Ganose, A. M. & Scanlon, D. O. Band gap and work function tailoring of SnO2 for improved transparent conducting ability in photovoltaics. *Journal of Materials Chemistry C* **4,** 1467–1475 (2016).

69. Jiang, Q., Zhang, L., Wang, H., Yang, X., Meng, J., Liu, H., Yin, Z., Wu, J., Zhang, X. & You, J. Enhanced electron extraction using SnO2 for high-efficiency planar-structure HC(NH2)2 PbI3-based perovskite solar cells. *Nature Energy* **2,** 1–7 (2017).

70. Dixon, S. C., Scanlon, D. O., Carmalt, C. J. & Parkin, I. P. n-Type doped transparent conducting binary oxides: an overview. *Journal of Materials Chemistry C* **4,** 6946–6961 (2016).

71. Zhang, P., Wu, J., Zhang, T., Wang, Y., Liu, D., Chen, H., Ji, L., Liu, C., Ahmad, W., Chen, Z. D. & Li, S. Perovskite Solar Cells with ZnO Electron-Transporting Materials. *Advanced Materials* **30,** 1703737 (2018).

72. Vogel, M., Doka, S., Breyer, C., Lux-Steiner, M. C. & Fostiropoulos, K. On the function of a bathocuproine buffer layer in organic photovoltaic cells. *Applied Physics Letters* **89,** 163501 (2006).

73. Yuan, D.-X., Yuan, X.-D., Xu, Q.-Y., Xu, M.-F., Shi, X.-B., Wang, Z.-K. & Liao, L.-S. A solution-processed bathocuproine cathode interfacial layer for high-performance bromine–iodine perovskite solar cells. *Physical Chemistry Chemical Physics* **17,** 26653–26658 (2015).

74. Carter, S. A., Angelopoulos, M., Karg, S., Brock, P. J. & Scott, J. C. Polymeric anodes for improved polymer light-emitting diode performance. *Applied Physics Letters* **70,** 2067–2069 (1997).

75. Yan, W., Li, Y., Li, Y., Ye, S., Liu, Z., Wang, S., Bian, Z. & Huang, C. High-performance hybrid perovskite solar cells with open circuit voltage dependence on hole-transporting materials. *Nano Energy* **16,** 428 –437 (2015).

76. Nie, W., Tsai, H., Asadpour, R., Blancon, J.-C., Neukirch, A. J., Gupta, G., Crochet, J. J., Chhowalla, M., Tretiak, S., Alam, M. A., Wang, H.-L. & Mohite, A. D. High-efficiency solution-processed perovskite solar cells with millimeter-scale grains. *Science* **347,** 522 (2015).

77. Zuo, C. & Ding, L. Modified PEDOT Layer Makes a 1.52 V Voc for Perovskite/PCBM Solar Cells. *Advanced Energy Materials* **7,** 1601193 (2017).

78. Xue, Q., Liu, M., Li, Z., Yan, L., Hu, Z., Zhou, J., Li, W., Jiang, X.-F., Xu, B., Huang, F., Li, Y., Yip, H.-L. & Cao, Y. Efficient and Stable Perovskite Solar Cells via Dual Functionalization of Dopamine Semiquinone Radical with Improved Trap Passivation Capabilities. *Advanced Functional Materials* **28,** 1707444 (2018).

79. Zhao, D., Sexton, M., Park, H.-Y., Baure, G., Nino, J. C. & So, F. High-Efficiency Solution-Processed Planar Perovskite Solar Cells with a Polymer Hole Transport Layer. *Advanced Energy Materials* **5,** 1401855 (2015).

80. Wang, Q., Bi, C. & Huang, J. Doped hole transport layer for efficiency enhancement in planar heterojunction organolead trihalide perovskite solar cells. *Nano Energy* **15,** 275–280 (2015).

81. Ye, S., Sun, W., Li, Y., Yan, W., Peng, H., Bian, Z., Liu, Z. & Huang, C. CuSCN-Based Inverted Planar Perovskite Solar Cell with an Average PCE of 15.6%. *Nano Letters* **15,** 3723–3728 (2015).

82. Chen, W., Wu, Y., Yue, Y., Liu, J., Zhang, W., Yang, X., Chen, H., Bi, E., Ashraful, I., Grätzel, M. & Han, L. Efficient and stable large-area perovskite solar cells with inorganic charge extraction layers. *Science* **350,** 944–948 (2015).

83. Ryu, S., Noh, J. H., Jeon, N. J., Chan Kim, Y., Yang, W. S., Seo, J. & Seok, S. I. Voltage output of efficient perovskite solar cells with high open-circuit voltage and fill factor. *Energy & Environmental Science* **7,** 2614–2618 (2014).

84. Liu, Z., Krückemeier, L., Krogmeier, B., Klingebiel, B., Márquez, J. A., Levcenko, S., Öz, S., Mathur, S., Rau, U., Unold, T. & Kirchartz, T. Open-Circuit Voltages Exceeding 1.26 v in Planar Methylammonium Lead Iodide Perovskite Solar Cells. *ACS Energy Letters* **4,** 110–117 (2019).

85. NREL. *ASTM G-173, Reference Air Mass 1.5 Spectra*

86. Hirst, L. C. & Ekins-Daukes, N. J. Fundamental losses in solar cells. *Progress in Photovoltaics: Research and Applications* **19,** 286–293 (2011).

87. Sha, W. E. I., Zhang, H., Wang, Z. S., Zhu, H. L., Ren, X., Lin, F., Jen, A. K. Y. & Choy, W. C. H. Quantifying Efficiency Loss of Perovskite Solar Cells by a Modified Detailed Balance Model. *Advanced Energy Materials* **8,** 1701586 (2018).

88. Pazos-Outón, L. M., Xiao, T. P. & Yablonovitch, E. Fundamental Efficiency Limit of Lead Iodide Perovskite Solar Cells. *The Journal of Physical Chemistry Letters* **9,** 1703–1711 (2018).

89. Burschka, J., Pellet, N., Moon, S.-J., Humphry-Baker, R., Gao, P., Nazeeruddin, M. K. & Grätzel, M. Sequential deposition as a route to high-performance perovskite-sensitized solar cells. *Nature* **499,** 316–319 (2013).

90. Liu, M., Johnston, M. B. & Snaith, H. J. Efficient planar heterojunction perovskite solar cells by vapour deposition. *Nature* **501,** 395–398 (2013).

91. Xiao, M., Huang, F., Huang, W., Dkhissi, Y., Zhu, Y., Etheridge, J., Gray-Weale, A., Bach, U., Cheng, Y.-B. & Spiccia, L. A Fast Deposition-Crystallization Procedure for Highly Efficient Lead Iodide Perovskite Thin-Film Solar Cells. *Angewandte Chemie International Edition* **53,** 9898–9903 (2014).

92. Jeon, N. J., Noh, J. H., Kim, Y. C., Yang, W. S., Ryu, S. & Seok, S. I. Solvent engineering for high-performance inorganic–organic hybrid perovskite solar cells. *Nature Materials* **13,** 897–903 (2014).

93. Zhang, W., Pathak, S., Sakai, N., Stergiopoulos, T., Nayak, P. K., Noel, N. K., Haghighirad, A. A., Burlakov, V. M., Dequilettes, D. W., Sadhanala, A., Li, W., Wang, L., Ginger, D. S., Friend, R. H. & Snaith, H. J. Enhanced optoelectronic quality of perovskite thin films with hypophosphorous acid for planar heterojunction solar cells. *Nature Communications* **6,** 10030 (2015).

94. Son, D.-Y., Lee, J.-W., Choi, Y. J., Jang, I.-H., Lee, S., Yoo, P. J., Shin, H., Ahn, N., Choi, M., Kim, D. & Park, N.-G. Self-formed grain boundary healing layer for highly efficient CH3NH3PbI3 perovskite solar cells. *Nature Energy* **1,** 16081 (2016).

95. Jacobsson, T. J., Correa-Baena, J.-P., Halvani Anaraki, E., Philippe, B., Stranks, S. D., Bouduban, M. E. F., Tress, W., Schenk, K., Teuscher, J., Moser, J.-E., Rensmo, H. & Hagfeldt, A. Unreacted PbI2 as a Double-Edged Sword for Enhancing the Performance of Perovskite Solar Cells. *Journal of the American Chemical Society* **138,** 10331–10343 (2016).

96. Liu, S., Guan, Y., Sheng, Y., Hu, Y., Rong, Y., Mei, A. & Han, H. A Review on Additives for Halide Perovskite Solar Cells. *Advanced Energy Materials* **10,** 1902492 (2020).

97. Jeon, N. J., Noh, J. H., Yang, W. S., Kim, Y. C., Ryu, S., Seo, J. & Seok, S. I. Compositional engineering of perovskite materials for high-performance solar cells. *Nature* **517,** 476–480 (2015).

98. Wang, Q., Dong, Q., Li, T., Gruverman, A. & Huang, J. Thin Insulating Tunneling Contacts for Efficient and Water-Resistant Perovskite Solar Cells. *Advanced Materials* **28,** 6734–6739 (2016).

99. Wolff, C. M., Zu, F., Paulke, A., Toro, L. P., Koch, N. & Neher, D. Reduced Interface-Mediated Recombination for High Open-Circuit Voltages in CH3NH3PbI3 Solar Cells. *Advanced Materials* **29,** 1700159 (2017).

100. Turren-Cruz, S.-H., Hagfeldt, A. & Saliba, M. Methylammonium-free, high-performance, and stable perovskite solar cells on a planar architecture. *Science* **362,** 449 (2018).

101. Peng, J., Khan, J. I., Liu, W., Ugur, E., Duong, T., Wu, Y., Shen, H., Wang, K., Dang, H., Aydin, E., Yang, X., Wan, Y., Weber, K. J., Catchpole, K. R., Laquai, F., De Wolf, S. & White, T. P. A Universal Double-Side Passivation for High Open-Circuit Voltage in Perovskite Solar Cells: Role of Carbonyl Groups in Poly(methyl methacrylate). *Advanced Energy Materials* **8,** 1801208 (2018).

102. Zheng, X., Chen, B., Dai, J., Fang, Y., Bai, Y., Lin, Y., Wei, H., Zeng, X. C. & Huang, J. Defect passivation in hybrid perovskite solar cells using quaternary ammonium halide anions and cations. *Nature Energy* **2,** 17102 (2017).

103. Luo, D., Yang, W., Wang, Z., Sadhanala, A., Hu, Q., Su, R., Shivanna, R., Trindade, G. F., Watts, J. F., Xu, Z., Liu, T., Chen, K., Ye, F., Wu, P., Zhao, L., Wu, J., Tu, Y., Zhang, Y., Yang, X., Zhang, W., Friend, R. H., Gong, Q., Snaith, H. J. & Zhu, R. Enhanced photovoltage for inverted planar heterojunction perovskite solar cells. *Science* **360,** 1442–1446 (2018).

104. Koh, T. M., Shanmugam, V., Guo, X., Lim, S. S., Filonik, O., Herzig, E. M., Müller-Buschbaum, P., Swamy, V., Chien, S. T., Mhaisalkar, S. G. & Mathews, N. Enhancing moisture tolerance in efficient hybrid 3D/2D perovskite photovoltaics. *Journal of Materials Chemistry A* **6,** 2122–2128 (2018).

105. Braly, I. L., deQuilettes, D. W., Pazos-Outón, L. M., Burke, S., Ziffer, M. E., Ginger, D. S. & Hillhouse, H. W. Hybrid perovskite films approaching the radiative limit with over 90% photoluminescence quantum efficiency. *Nature Photonics* **12,** 355–361 (2018).

106. Stolterfoht, M., Wolff, C. M., Márquez, J., Zhang, S., Hages, C. J., Rothhardt, D., Albrecht, S., Burn, P. L., Meredith, P., Unold, T. & Neher, D. Visualization and suppression of interfacial recombination for high-efficiency large-area pin perovskite solar cells. *Nature Energy* **3,** 847–854 (2018).

107. Tessler, N. & Vaynzof, Y. Insights from Device Modeling of Perovskite Solar Cells. *ACS Energy Letters* **5,** 1260–1270 (2020).

108. Stolterfoht, M., Caprioglio, P., Wolff, C. M., Márquez, J., Nordmann, J., Zhang, S., Rothhardt, D., Hörmann, U., Amir, Y., Redinger, A., Kegelmann, L., Zu, F., Albrecht, S., Koch, N., Kirchartz, T., Saliba, M., Unold, T. & Neher, D. The impact of energy alignment and interfacial recombination on the internal and external open-circuit voltage of perovskite solar cells. *Energy & Environmental Science* **12,** 2778–2788 (2019).

109. Bi, C., Wang, Q., Shao, Y., Yuan, Y., Xiao, Z. & Huang, J. Non-wetting surface-driven high-aspect-ratio crystalline grain growth for efficient hybrid perovskite solar cells. *Nature Communications* **6,** 7747 (2015).

110. Yang, D., Sano, T., Yaguchi, Y., Sun, H., Sasabe, H. & Kido, J. Achieving 20% Efficiency for Low-Temperature-Processed Inverted Perovskite Solar Cells. *Advanced Functional Materials* **29,** 1807556 (2019).

111. Lim, K.-G., Ahn, S., Kim, Y.-H., Qi, Y. & Lee, T.-W. Universal energy level tailoring of self-organized hole extraction layers in organic solar cells and organic–inorganic hybrid perovskite solar cells. *Energy & Environmental Science* **9,** 932–939 (2016).

112. Lee, J.-H., Kim, J., Kim, G., Shin, D., Jeong, S. Y., Lee, J., Hong, S., Choi, J. W., Lee, C.-L., Kim, H., Yi, Y. & Lee, K. Introducing paired electric dipole layers for efficient and reproducible perovskite solar cells. *Energy & Environmental Science* **11,** 1742–1751 (2018).

113. Butscher, J. F., Intorp, S., Kress, J., An, Q., Hofstetter, Y. J., Hippchen, N., Paulus, F., Bunz, U. H. F., Tessler, N. & Vaynzof, Y. Enhancing the Open-Circuit Voltage of Perovskite Solar Cells by Embedding Molecular Dipoles within Their Hole-Blocking Layer. *ACS Applied Materials & Interfaces* **12,** 3572–3579 (2020).

114. Chen, W., Xu, L., Feng, X., Jie, J. & He, Z. Metal Acetylacetonate Series in Interface Engineering for Full Low-Temperature-Processed, High-Performance, and Stable Planar Perovskite Solar Cells with Conversion Efficiency over 16% on 1 cm2 Scale. *Advanced Materials* **29,** 1603923 (2017).

115. Shao, Y., Yuan, Y. & Huang, J. Correlation of energy disorder and open-circuit voltage in hybrid perovskite solar cells. *Nature Energy* **1,** 15001 (2016).

116. Chen, W., Liu, F.-Z., Feng, X.-Y., Djurišić, A. B., Chan, W. K. & He, Z.-B. Cesium Doped NiOx as an Efficient Hole Extraction Layer for Inverted Planar Perovskite Solar Cells. *Advanced Energy Materials* **7,** 1700722 (2017).

117. Zhang, W., Saliba, M., Moore, D. T., Pathak, S. K., Hörantner, M. T., Stergiopoulos, T., Stranks, S. D., Eperon, G. E., Alexander-Webber, J. A., Abate, A., Sadhanala, A., Yao, S., Chen, Y., Friend, R. H., Estroff, L. A., Wiesner, U. & Snaith, H. J. Ultrasmooth organic–inorganic perovskite thin-film formation and crystallization for efficient planar heterojunction solar cells. *Nature Communications* **6,** 6142 (2015).

118. An, Q. *Master Thesis: Magnesium, Zirconium and Lithium Doping of ZnO Layer and Its Effect on the Performance of Hybrid Solar Cell* (Ruperto-Carola-University of Heidelberg, 2016).

119. Vaynzof, Y., Kabra, D., Zhao, L., Ho, P. K. H., Wee, A. T.-S. & Friend, R. H. Improved photoinduced charge carriers separation in organic-inorganic hybrid photovoltaic devices. *Applied Physics Letters* **97,** 033309 (2010).

120. Arndt, S., Borstelmann, J., EshaghSaatlo, R., Antoni, P. W., Rominger, F., Rudolph, M., An, Q., Vaynzof, Y. & Hashmi, A. S. K. The Gold(I)-Mediated Domino Reaction to Fused Diphenyl Phosphoniumfluorenes: Mechanistic Consequences for Gold-Catalyzed Hydroarylations and Application in Solar Cells. *Chemistry – A European Journal* **24,** 7882–7889 (2018).

121. De Mello, J. C., Wittmann, H. F. & Friend, R. H. An improved experimental determination of external photoluminescence quantum efficiency. *Advanced Materials* **9,** 230–232 (1997).

122. Shuttle, C. G., O'Regan, B., Ballantyne, A. M., Nelson, J., Bradley, D. D. C., de Mello, J. & Durrant, J. R. Experimental determination of the rate law for charge carrier decay in a polythiophene: Fullerene solar cell. *Applied Physics Letters* **92,** 093311 (2008).

123. Schilinsky, P., Waldauf, C. & Brabec, C. J. Recombination and loss analysis in polythiophene based bulk heterojunction photodetectors. *Applied Physics Letters* **81,** 3885–3887 (2002).

124. Cowan, S. R., Roy, A. & Heeger, A. J. Recombination in polymer-fullerene bulk heterojunction solar cells. *Physical Review B* **82,** 245207 (2010).

125. Koster, L. J. A., Mihailetchi, V. D., Ramaker, R. & Blom, P. W. M. Light intensity dependence of open-circuit voltage of polymer:fullerene solar cells. *Applied Physics Letters* **86,** 123509 (2005).

126. Tress, W., Correa Baena, J. P., Saliba, M., Abate, A. & Graetzel, M. Inverted Current–Voltage Hysteresis in Mixed Perovskite Solar Cells: Polarization, Energy Barriers, and Defect Recombination. *Advanced Energy Materials* **6,** 1600396 (2016).

127. Wetzelaer, G.-J. A. H., Scheepers, M., Sempere, A. M., Momblona, C., Ávila, J. & Bolink, H. J. Trap-Assisted Non-Radiative Recombination in Organic–Inorganic Perovskite Solar Cells. *Advanced Materials* **27,** 1837–1841 (2015).

128. Leijtens, T., Eperon, G. E., Barker, A. J., Grancini, G., Zhang, W., Ball, J. M., Kandada, A. R. S., Snaith, H. J. & Petrozza, A. Carrier trapping and recombination: the role of defect physics in enhancing the open circuit voltage of metal halide perovskite solar cells. *Energy & Environmental Science* **9,** 3472–3481 (2016).

129. Liu, D. & Kelly, T. L. Perovskite solar cells with a planar heterojunction structure prepared using room-temperature solution processing techniques. *Nature Photonics* **8,** 133–138 (2014).

130. Cheng, Y., Yang, Q. D., Xiao, J., Xue, Q., Li, H. W., Guan, Z., Yip, H. L. & Tsang, S. W. Decomposition of organometal halide perovskite films on zinc oxide nanoparticles. *ACS Applied Materials & Interfaces* **7,** 19986–19993 (2015).

131. Dkhissi, Y., Meyer, S., Chen, D., Weerasinghe, H. C., Spiccia, L., Cheng, Y.-B. & Caruso, R. A. Stability Comparison of Perovskite Solar Cells Based on Zinc Oxide and Titania on Polymer Substrates. *ChemSusChem* **9,** 687–695 (2016).

132. Yang, J., Siempelkamp, B. D., Mosconi, E., De Angelis, F. & Kelly, T. L. Origin of the Thermal Instability in CH3NH3PbI3 Thin Films Deposited on ZnO. *Chemistry of Materials* **27,** 4229–4236 (2015).

133. Özgür, Ü., Alivov, Y. I., Liu, C., Teke, A., Reshchikov, M. A., Doğan, S., Avrutin, V., Cho, S.-J. & Morkoç, H. A comprehensive review of ZnO materials and devices. *Journal of Applied Physics* **98,** 041301 (2005).

134. Zhao, X., Shen, H., Zhang, Y., Li, X., Zhao, X., Tai, M., Li, J., Li, J., Li, X. & Lin, H. Aluminum-Doped Zinc Oxide as Highly Stable Electron Collection Layer for Perovskite Solar Cells. *ACS Applied Materials & Interfaces* **8,** 7826–7833 (2016).

135. Kim, J., Kim, G., Kim, T. K., Kwon, S., Back, H., Lee, J., Lee, S. H., Kang, H. & Lee, K. Efficient planar-heterojunction perovskite solar cells achieved via interfacial modification of a sol–gel ZnO electron collection layer. *Journal of Materials Chemistry A* **2,** 17291–17296 (2014).

136. Dong, X., Hu, H., Lin, B., Ding, J. & Yuan, N. The effect of ALD-Zno layers on the formation of CH3NH3PbI3 with different perovskite precursors and sintering temperatures. *Chemical Communications* **50,** 14405–14408 (2014).

137. Zhang, J. & Pauporté, T. Effects of Oxide Contact Layer on the Preparation and Properties of CH3NH3PbI3 for Perovskite Solar Cell Application. *The Journal of Physical Chemistry C* **119,** 14919–14928 (2015).

138. Tseng, Z. L., Chiang, C. H. & Wu, C. G. Surface Engineering of ZnO Thin Film for High Efficiency Planar Perovskite Solar Cells. *Scientific Reports* **5,** 1–10 (2015).

139. Zuo, L., Gu, Z., Ye, T., Fu, W., Wu, G., Li, H. & Chen, H. Enhanced Photovoltaic Performance of CH3NH3PbI3 Perovskite Solar Cells through Interfacial Engineering Using Self-Assembling Monolayer. *Journal of the American Chemical Society* **137,** 2674–2679 (2015).

140. Cao, J., Wu, B., Chen, R., Wu, Y., Hui, Y., Mao, B.-W. & Zheng, N. Efficient, Hysteresis-Free, and Stable Perovskite Solar Cells with ZnO as Electron-Transport Layer: Effect of Surface Passivation. *Advanced Materials* **30,** 1705596 (2018).

141. Tavakoli, M. M., Tavakoli, R., Yadav, P. & Kong, J. A graphene/ZnO electron transfer layer together with perovskite passivation enables highly efficient and stable perovskite solar cells. *Journal of Materials Chemistry A* **7,** 679–686 (2019).

142. Schutt, K., Nayak, P. K., Ramadan, A. J., Wenger, B., Lin, Y.-H. & Snaith, H. J. Overcoming Zinc Oxide Interface Instability with a Methylammonium-Free Perovskite for High-Performance Solar Cells. *Advanced Functional Materials* **29,** 1900466 (2019).

143. Kim, E., Vaynzof, Y., Sepe, A., Guldin, S., Scherer, M., Cunha, P., Roth, S. V. & Steiner, U. Gyroid-Structured 3D ZnO Networks Made by Atomic Layer Deposition. *Advanced Functional Materials* **24,** 863–872 (2014).

144. Guérin, D., Lenfant, S., Godey, S. & Vuillaume, D. Synthesis and electrical properties of fullerene-based molecular junctions on silicon substrate. *Journal of Materials Chemistry* **20,** 2680–2690 (2010).

145. Pachoumi, O., Bakulin, A. A., Sadhanala, A., Sirringhaus, H., Friend, R. H. & Vaynzof, Y. Improved Performance of ZnO/Polymer Hybrid Photovoltaic Devices by Combining Metal Oxide Doping and Interfacial Modification. *The Journal of Physical Chemistry C* **118,** 18945–18950 (2014).

146. Sevinchan, Y., Hopkinson, P. E., Bakulin, A. A., Herz, J., Motzkus, M. & Vaynzof, Y. Improving Charge Separation across a Hybrid Oxide/Polymer Interface by Cs Doping of the Metal Oxide. *Advanced Materials Interfaces* **3,** 1500616 (2016).

147. Hinzmann, C., Magen, O., Hofstetter, Y. J., Hopkinson, P. E., Tessler, N. & Vaynzof, Y. Effect of Injection Layer Sub-Bandgap States on Electron Injection in Organic Light-Emitting Diodes. *ACS Applied Materials & Interfaces* **9,** 6220–6227 (2017).

148. Patel, J. B., Milot, R. L., Wright, A. D., Herz, L. M. & Johnston, M. B. Formation Dynamics of CH3NH3PbI3 Perovskite Following Two-Step Layer Deposition. *The Journal of Physical Chemistry Letters* **7,** 96–102 (2016).

149. Bi, C., Shao, Y., Yuan, Y., Xiao, Z., Wang, C., Gao, Y. & Huang, J. Understanding the formation and evolution of interdiffusion grown organolead halide perovskite thin films by thermal annealing. *Journal of Materials Chemistry A* **2,** 18508–18514 (2014).

150. Bai, S., Sakai, N., Zhang, W., Wang, Z., Wang, J. T.-W., Gao, F. & Snaith, H. J. Reproducible Planar Heterojunction Solar Cells Based on One-Step Solution-Processed Methylammonium Lead Halide Perovskites. *Chemistry of Materials* **29,** 462–473 (2017).

151. Xiao, Z., Dong, Q., Bi, C., Shao, Y., Yuan, Y. & Huang, J. Solvent Annealing of Perovskite-Induced Crystal Growth for Photovoltaic-Device Efficiency Enhancement. *Advanced Materials* **26,** 6503–6509 (2014).

152. Zhang, F., Song, J., Zhang, L., Niu, F., Hao, Y., Zeng, P., Niu, H., Huang, J. & Lian, J. Film-through large perovskite grains formation via a combination of sequential thermal and solvent treatment. *Journal of Materials Chemistry A* **4,** 8554–8561 (2016).

153. Fu, F., Feurer, T., Jäger, T., Avancini, E., Bissig, B., Yoon, S., Buecheler, S. & Tiwari, A. N. Low-temperature-processed efficient semi-transparent planar perovskite solar cells for bifacial and tandem applications. *Nature Communications* **6,** 8932 (2015).

154. Qiu, W., Bastos, J. P., Dasgupta, S., Merckx, T., Cardinaletti, I., Jenart, M. V. C., Nielsen, C. B., Gehlhaar, R., Poortmans, J., Heremans, P., McCulloch, I. & Cheyns, D. Highly efficient perovskite solar cells with crosslinked PCBM interlayers. *Journal of Materials Chemistry A* **5,** 2466–2472 (2017).

155. Ryu, S., Seo, J., Shin, S. S., Kim, Y. C., Jeon, N. J., Noh, J. H. & Seok, S. I. Fabrication of metal-oxide-free CH3NH3PbI3 perovskite solar cells processed at low temperature. *Journal of Materials Chemistry A* **3,** 3271–3275 (2015).

156. Dong, Y., Li, W., Zhang, X., Xu, Q., Liu, Q., Li, C. & Bo, Z. Highly Efficient Planar Perovskite Solar Cells Via Interfacial Modification with Fullerene Derivatives. *Small* **12,** 1098–1104 (2016).

157. Ma, T., Tadaki, D., Sakuraba, M., Sato, S., Hirano-Iwata, A. & Niwano, M. Effects of interfacial chemical states on the performance of perovskite solar cells. *Journal of Materials Chemistry A* **4,** 4392–4397 (2016).

158. Mahmud, M. A., Elumalai, N. K., Upama, M. B., Wang, D., Wright, M., Sun, T., Xu, C., Haque, F. & Uddin, A. Simultaneous enhancement in stability and efficiency of low-temperature processed perovskite solar cells. *RSC Advances* **6,** 86108–86125 (2016).

159. Stranks, S. D. & Snaith, H. J. Metal-halide perovskites for photovoltaic and light-emitting devices. *Nature Nanotechnology* **10,** 391–402 (2015).

160. Shao, Y., Xiao, Z., Bi, C., Yuan, Y. & Huang, J. Origin and elimination of photocurrent hysteresis by fullerene passivation in CH3NH3PbI3 planar heterojunction solar cells. *Nature Communications* **5,** 1–7 (2014).

161. Heo, J. H., Han, H. J., Kim, D., Ahn, T. K. & Im, S. H. Hysteresis-less inverted CH3NH3PbI3 planar perovskite hybrid solar cells with 18.1% power conversion efficiency. *Energy & Environmental Science* **8,** 1602–1608 (2015).

162. Zhang, X., Qin, J., Xue, Y., Yu, P., Zhang, B., Wang, L. & Liu, R. Effect of aspect ratio and surface defects on the photocatalytic activity of ZnO nanorods. *Scientific Reports* **4,** 4596 (2014).

163. Krzywiecki, M., Grządziel, L., Sarfraz, A., Iqbal, D., Szwajca, A. & Erbe, A. Zinc oxide as a defect-dominated material in thin films for photovoltaic applications – experimental determination of defect levels, quantification of composition, and construction of band diagram. *Phys. Chem. Chem. Phys.* **17,** 10004–10013 (15 2015).

164. Peng, H., Xu, W., Zhou, F., Zhang, J. & Li, C. Enhanced efficiency of inverted polymer solar cells using surface modified Cs-doped ZnO as electron transporting layer. *Synthetic Metals* **205,** 164–168 (2015).

165. Zuo, L., Zhang, S., Dai, S. & Chen, H. Versatility and robustness of ZnO:Cs electron transporting layer for printable organic solar cells. *RSC Advances* **5,** 49369–49375 (2015).

166. Ischenko, V., Polarz, S., Grote, D., Stavarache, V., Fink, K. & Driess, M. Zinc Oxide Nanoparticles with Defects. *Advanced Functional Materials* **15,** 1945–1954 (2005).

167. Pachoumi, O., Li, C., Vaynzof, Y., Banger, K. K. & Sirringhaus, H. Improved Performance and Stability of Inverted Organic Solar Cells with Sol–Gel Processed, Amorphous Mixed Metal Oxide Electron Extraction Layers Comprising Alkaline Earth Metals. *Advanced Energy Materials* **3,** 1428–1436 (2013).

168. Wang, C., Li, C., Wen, S., Ma, P., Liu, Y., MacKenzie, R. C. I., Tian, W. & Ruan, S. Combining plasmonic trap filling and optical backscattering for highly efficient third generation solar cells. *Journal of Materials Chemistry A* **5,** 3995–4002 (2017).

169. Wu, C. G., Chiang, C. H. & Chang, S. H. A perovskite cell with a record-high-Voc of 1.61 v based on solvent annealed CH3NH3PbBr3/ICBA active layer. *Nanoscale* **8,** 4077–4085 (2016).

170. Zhong, Y., Hufnagel, M., Thelakkat, M., Li, C. & Huettner, S. Role of PCBM in the Suppression of Hysteresis in Perovskite Solar Cells. *Advanced Functional Materials* **30,** 1908920 (2020).

171. Peng, S., Miao, J., Murtaza, I., Zhao, L., Hu, Z., Liu, M., Yang, T., Liang, Y., Meng, H. & Huang, W. An efficient and thickness insensitive cathode interface material for high performance inverted perovskite solar cells with 17.27% efficiency. *Journal of Materials Chemistry C* **5,** 5949–5955 (2017).

172. Zhang, H., Azimi, H., Hou, Y., Ameri, T., Przybilla, T., Spiecker, E., Kraft, M., Scherf, U. & Brabec, C. J. Improved High-Efficiency Perovskite Planar Heterojunction Solar Cells via Incorporation of a Polyelectrolyte Interlayer. *Chemistry of Materials* **26,** 5190–5193 (2014).

173. Chang, C.-Y., Chang, Y.-C., Huang, W.-K., Lee, K.-T., Cho, A.-C. & Hsu, C.-C. Enhanced Performance and Stability of Semitransparent Perovskite Solar Cells Using Solution-Processed Thiol-Functionalized Cationic Surfactant as Cathode Buffer Layer. *Chemistry of Materials* **27,** 7119–7127 (2015).

174. Xue, Q., Hu, Z., Liu, J., Lin, J., Sun, C., Chen, Z., Duan, C., Wang, J., Liao, C., Lau, W. M., Huang, F., Yip, H.-L. & Cao, Y. Highly efficient fullerene/perovskite planar heterojunction solar cells via cathode modification with an amino-functionalized polymer interlayer. *Journal of Materials Chemistry A* **2,** 19598–19603 (2014).

175. Ciro, J., Mesa, S., Uribe, J. I., Mejía-Escobar, M. A., Ramirez, D., Montoya, J. F., Betancur, R., Yoo, H.-S., Park, N.-G. & Jaramillo, F. Optimization of the Ag/PCBM interface by a rhodamine interlayer to enhance the efficiency and stability of perovskite solar cells. *Nanoscale* **9,** 9440–9446 (2017).

176. Rivkin, B., Fassl, P., Sun, Q., Taylor, A. D., Chen, Z. & Vaynzof, Y. Effect of Ion Migration-Induced Electrode Degradation on the Operational Stability of Perovskite Solar Cells. *ACS Omega* **3,** 10042–10047 (2018).

177. Docampo, P., Ball, J. M., Darwich, M., Eperon, G. E. & Snaith, H. J. Efficient organometal trihalide perovskite planar-heterojunction solar cells on flexible polymer substrates. *Nature Communications* **4,** 2761 (2013).

178. Wang, Q., Shao, Y., Dong, Q., Xiao, Z., Yuan, Y. & Huang, J. Large fill-factor bilayer iodine perovskite solar cells fabricated by a low-temperature solution-process. *Energy Environ. Sci.* **7,** 2359–2365 (2014).

179. Chen, G., Zhang, F., Liu, M., Song, J., Lian, J., Zeng, P., Yip, H.-L., Yang, W., Zhang, B. & Cao, Y. Fabrication of high-performance and low-hysteresis lead halide perovskite solar cells by utilizing a versatile alcohol-soluble bispyridinium salt as an efficient cathode modifier. *Journal of Materials Chemistry A* **5,** 17943–17953 (2017).

180. Yin, X., Que, M., Xing, Y. & Que, W. High efficiency hysteresis-less inverted planar heterojunction perovskite solar cells with a solution-derived NiOx hole contact layer. *Journal of Materials Chemistry A* **3,** 24495–24503 (2015).

181. Kato, Y., Ono, L. K., Lee, M. V., Wang, S., Raga, S. R. & Qi, Y. Silver Iodide Formation in Methyl Ammonium Lead Iodide Perovskite Solar Cells with Silver Top Electrodes. *Advanced Materials Interfaces* **2,** 1500195 (2015).

182. Fang, R., Wu, S., Chen, W., Liu, Z., Zhang, S., Chen, R., Yue, Y., Deng, L., Cheng, Y.-B., Han, L. & Chen, W. [6,6]-Phenyl-C61-Butyric Acid Methyl Ester/Cerium Oxide Bilayer Structure as Efficient and Stable Electron Transport Layer for Inverted Perovskite Solar Cells. *ACS Nano* **12,** 2403–2414 (2018).

183. Chen, C., Zhang, S., Wu, S., Zhang, W., Zhu, H., Xiong, Z., Zhang, Y. & Chen, W. Effect of BCP buffer layer on eliminating charge accumulation for high performance of inverted perovskite solar cells. *RSC Advances* **7,** 35819–35826 (2017).

184. Rau, U. Reciprocity relation between photovoltaic quantum efficiency and electroluminescent emission of solar cells. *Physical Review B* **76,** 085303 (2007).

185. Zhang, G., Hawks, S. A., Ngo, C., Schelhas, L. T., Scholes, D. T., Kang, H., Aguirre, J. C., Tolbert, S. H. & Schwartz, B. J. Extensive Penetration of Evaporated Electrode Metals into Fullerene Films: Intercalated Metal Nanostructures and Influence on Device Architecture. *ACS Applied Materials & Interfaces* **7,** 25247–25258 (2015).

186. Patil, B. R., Ahmadpour, M., Sherafatipour, G., Qamar, T., Fernández, A. F., Zojer, K., Rubahn, H.-G. & Madsen, M. Area dependent behavior of bathocuproine (BCP) as cathode interfacial layers in organic photovoltaic cells. *Scientific Reports* **8,** 12608 (2018).

187. Roichman, Y., Preezant, Y. & Tessler, N. Analysis and modeling of organic devices (Chap 12). *Physics of Organic Semiconductors* **201,** 1246–1262 (2004).

188. Heumueller, T., Burke, T. M., Mateker, W. R., Sachs-Quintana, I. T., Vandewal, K., Brabec, C. J. & McGehee, M. D. Disorder-Induced Open-Circuit Voltage Losses in Organic Solar Cells During Photoinduced Burn-In. *Advanced Energy Materials* **5,** 1500111 (2015).

189. Hoven, C. V., Garcia, A., Bazan, G. C. & Nguyen, T.-Q. Recent Applications of Conjugated Polyelectrolytes in Optoelectronic Devices. *Advanced Materials* **20,** 3793–3810 (2008).

190. Chueh, C.-C., Li, C.-Z. & Jen, A. K.-Y. Recent progress and perspective in solution-processed Interfacial materials for efficient and stable polymer and organometal perovskite solar cells. *Energy Environ. Sci.* **8,** 1160–1189 (2015).

191. Vilan, A., Ghabboun, J. & Cahen, D. MoleculeMetal Polarization at Rectifying GaAs Interfaces. *The Journal of Physical Chemistry B* **107,** 6360–6376 (2003).

192. Lee, J., Park, S., Lee, Y., Kim, H., Shin, D., Jeong, J., Jeong, K., Cho, S. W., Lee, H. & Yi, Y. Electron transport mechanism of bathocuproine exciton blocking layer in organic photovoltaics. *Phys. Chem. Chem. Phys.* **18,** 5444–5452 (7 2016).

193. Tan, Z.-K., Vaynzof, Y., Credgington, D., Li, C., Casford, M. T. L., Sepe, A., Huettner, S., Nikolka, M., Paulus, F., Yang, L., Sirringhaus, H., Greenham, N. C. & Friend, R. H. In-Situ Switching from Barrier-Limited to Ohmic Anodes for Efficient Organic Optoelectronics. *Advanced Functional Materials* **24,** 3051–3058 (2014).

194. An, Q., Fassl, P., Hofstetter, Y. J., Becker-Koch, D., Bausch, A., Hopkinson, P. E. & Vaynzof, Y. High performance planar perovskite solar cells by ZnO electron transport layer engineering. *Nano Energy* **39,** 400 –408 (2017).

195. Buin, A., Comin, R., Xu, J., Ip, A. H. & Sargent, E. H. Halide-Dependent Electronic Structure of Organolead Perovskite Materials. *Chemistry of Materials* **27,** 4405–4412 (2015).

196. Phung, N., Al-Ashouri, A., Meloni, S., Mattoni, A., Albrecht, S., Unger, E. L., Merdasa, A. & Abate, A. The Role of Grain Boundaries on Ionic Defect Migration in Metal Halide Perovskites. *Advanced Energy Materials* **10,** 1903735 (2020).

197. Fassl, P., Ternes, S., Lami, V., Zakharko, Y., Heimfarth, D., Hopkinson, P. E., Paulus, F., Taylor, A. D., Zaumseil, J. & Vaynzof, Y. Effect of Crystal Grain Orientation on the Rate of Ionic Transport in Perovskite Polycrystalline Thin Films. *ACS Applied Materials & Interfaces* **11,** 2490–2499 (2019).

198. Wang, Q., Chen, B., Liu, Y., Deng, Y., Bai, Y., Dong, Q. & Huang, J. Scaling behavior of moisture-induced grain degradation in polycrystalline hybrid perovskite thin films. *Energy Environ. Sci.* **10,** 516–522 (2017).

199. Saliba, M., Matsui, T., Domanski, K., Seo, J.-Y., Ummadisingu, A., Zakeeruddin, S. M., Correa-Baena, J.-P., Tress, W. R., Abate, A., Hagfeldt, A. & Grätzel, M. Incorporation of rubidium cations into perovskite solar cells improves photovoltaic performance. *Science* **354,** 206–209 (2016).

200. Son, D.-Y., Kim, S.-G., Seo, J.-Y., Lee, S.-H., Shin, H., Lee, D. & Park, N.-G. Universal Approach toward Hysteresis-Free Perovskite Solar Cell via Defect Engineering. *Journal of the American Chemical Society* **140,** 1358–1364 (2018).

201. Zhou, W., Li, D., Xiao, Z., Wen, Z., Zhang, M., Hu, W., Wu, X., Wang, M., Zhang, W.-H., Lu, Y., Yang, S. & Yang, S. Zwitterion Coordination Induced Highly Orientational Order of CH3NH3PbI3 Perovskite Film Delivers a High Open Circuit Voltage Exceeding 1.2 V. *Advanced Functional Materials* **29,** 1901026 (2019).

202. Xu, W., Lei, G., Tao, C., Zhang, J., Liu, X., Xu, X., Lai, W.-Y., Gao, F. & Huang, W. Precisely Controlling the Grain Sizes with an Ammonium Hypophosphite Additive for High-Performance Perovskite Solar Cells. *Advanced Functional Materials* **28,** 1802320 (2018).

203. Bai, S., Da, P., Li, C., Wang, Z., Yuan, Z., Fu, F., Kawecki, M., Liu, X., Sakai, N., Wang, J. T.-W., Huettner, S., Buecheler, S., Fahlman, M., Gao, F. & Snaith, H. J. Planar perovskite solar cells with long-term stability using ionic liquid additives. *Nature* **571,** 245–250 (2019).

204. Lin, Y.-H., Sakai, N., Da, P., Wu, J., Sansom, H. C., Ramadan, A. J., Mahesh, S., Liu, J., Oliver, R. D. J., Lim, J., Aspitarte, L., Sharma, K., Madhu, P. K., Morales-Vilches, A. B., Nayak, P. K., Bai, S., Gao, F., Grovenor, C. R. M., Johnston, M. B., Labram, J. G., Durrant, J. R., Ball, J. M., Wenger, B., Stannowski, B. & Snaith, H. J. A piperidinium salt stabilizes efficient metal-halide perovskite solar cells. *Science* **369,** 96–102 (2020).

205. Shi, Y., Wu, W., Dong, H., Li, G., Xi, K., Divitini, G., Ran, C., Yuan, F., Zhang, M., Jiao, B., Hou, X. & Wu, Z. A Strategy for Architecture Design of Crystalline Perovskite Light-Emitting Diodes with High Performance. *Advanced Materials* **30,** 1800251 (2018).

206. Miao, Y., Ke, Y., Wang, N., Zou, W., Xu, M., Cao, Y., Sun, Y., Yang, R., Wang, Y., Tong, Y., Xu, W., Zhang, L., Li, R., Li, J., He, H., Jin, Y., Gao, F., Huang, W. & Wang, J. Stable and bright formamidinium-based perovskite light-emitting diodes with high energy conversion efficiency. *Nature Communications* **10,** 3624 (2019).

207. Kumawat, N. K., Jain, N., Dey, A., Narasimhan, K. L. & Kabra, D. Quantitative Correlation of Perovskite Film Morphology to Light Emitting Diodes Efficiency Parameters. *Advanced Functional Materials* **27,** 1603219 (2017).

208. Cao, Y., Wang, N., Tian, H., Guo, J., Wei, Y., Chen, H., Miao, Y., Zou, W., Pan, K., He, Y., Cao, H., Ke, Y., Xu, M., Wang, Y., Yang, M., Du, K., Fu, Z., Kong, D., Dai, D., Jin, Y., Li, G., Li, H., Peng, Q., Wang, J. & Huang, W. Perovskite light-emitting diodes based on spontaneously formed submicrometre-scale structures. *Nature* **562,** 249–253 (2018).

209. Xu, W., Hu, Q., Bai, S., Bao, C., Miao, Y., Yuan, Z., Borzda, T., Barker, A. J., Tyukalova, E., Hu, Z., Kawecki, M., Wang, H., Yan, Z., Liu, X., Shi, X., Uvdal, K., Fahlman, M., Zhang, W., Duchamp, M., Liu, J.-M., Petrozza, A., Wang, J., Liu, L.-M., Huang, W. & Gao, F. Rational molecular passivation for high-performance perovskite light-emitting diodes. *Nature Photonics* **13,** 418–424 (2019).

210. Seager, C. H. Grain Boundaries in Polycrystalline Silicon. *Annual Review of Materials Science* **15,** 271–302 (1985).

211. Yun, J. S., Ho-Baillie, A., Huang, S., Woo, S. H., Heo, Y., Seidel, J., Huang, F., Cheng, Y.-B. & Green, M. A. Benefit of Grain Boundaries in Organic–Inorganic Halide Planar Perovskite Solar Cells. *The Journal of Physical Chemistry Letters* **6,** 875–880 (2015).

212. Yang, M., Zeng, Y., Li, Z., Kim, D. H., Jiang, C.-S., van de Lagemaat, J. & Zhu, K. Do grain boundaries dominate non-radiative recombination in CH3NH3PbI3 perovskite thin films? *Phys. Chem. Chem. Phys.* **19,** 5043–5050 (7 2017).

213. Shao, Y., Fang, Y., Li, T., Wang, Q., Dong, Q., Deng, Y., Yuan, Y., Wei, H., Wang, M., Gruverman, A., Shield, J. & Huang, J. Grain boundary dominated ion migration in polycrystalline organic–inorganic halide perovskite films. *Energy Environ. Sci.* **9,** 1752–1759 (2016).

214. Ren, X., Yang, Z., Yang, D., Zhang, X., Cui, D., Liu, Y., Wei, Q., Fan, H. & Liu, S. F. Modulating crystal grain size and optoelectronic properties of perovskite films for solar cells by reaction temperature. *Nanoscale* **8,** 3816–3822 (2016).

215. Sherkar, T. S., Momblona, C., Gil-Escrig, L., Bolink, H. J. & Koster, L. J. A. Improving Perovskite Solar Cells: Insights From a Validated Device Model. *Advanced Energy Materials* **7,** 1602432 (2017).

216. Sherkar, T. S., Momblona, C., Gil-Escrig, L., Ávila, J., Sessolo, M., Bolink, H. J. & Koster, L. J. A. Recombination in Perovskite Solar Cells: Significance of Grain Boundaries, Interface Traps, and Defect Ions. *ACS Energy Letters* **2,** 1214–1222 (2017).

217. Noel, N. K., Congiu, M., Ramadan, A. J., Fearn, S., McMeekin, D. P., Patel, J. B., Johnston, M. B., Wenger, B. & Snaith, H. J. Unveiling the Influence of pH on the Crystallization of Hybrid Perovskites, Delivering Low Voltage Loss Photovoltaics. *Joule* **1,** 328–343 (2017).

218. Stoumpos, C. C., Malliakas, C. D. & Kanatzidis, M. G. Semiconducting Tin and Lead Iodide Perovskites with Organic Cations: Phase Transitions, High Mobilities, and Near-Infrared Photoluminescent Properties. *Inorganic Chemistry* **52,** 9019–9038 (2013).

219. Wakamiya, A., Endo, M., Sasamori, T., Tokitoh, N., Ogomi, Y., Hayase, S. & Murata, Y. Reproducible Fabrication of Efficient Perovskite-based Solar Cells: X-ray Crystallographic Studies on the Formation of CH3NH3PbI3 Layers. *Chemistry Letters* **43,** 711–713 (2014).

220. Bae, S., Han, S. J., Shin, T. J. & Jo, W. H. Two different mechanisms of CH3NH3PbI3 film formation in one-step deposition and its effect on photovoltaic properties of OPV-type perovskite solar cells. *Journal of Materials Chemistry A* **3,** 23964–23972 (2015).

221. Hao, F., Stoumpos, C. C., Liu, Z., Chang, R. P. H. & Kanatzidis, M. G. Controllable Perovskite Crystallization at a Gas–Solid Interface for Hole Conductor-Free Solar Cells with Steady Power Conversion Efficiency over 10%. *Journal of the American Chemical Society* **136,** 16411–16419 (2014).

222. Mei, A., Li, X., Liu, L., Ku, Z., Liu, T., Rong, Y., Xu, M., Hu, M., Chen, J., Yang, Y., Grätzel, M. & Han, H. A hole-conductor–free, fully printable mesoscopic perovskite solar cell with high stability. *Science* **345,** 295 (2014).

223. Jones, T. W., Osherov, A., Alsari, M., Sponseller, M., Duck, B. C., Jung, Y.-K., Settens, C., Niroui, F., Brenes, R., Stan, C. V., Li, Y., Abdi-Jalebi, M., Tamura, N., Macdonald, J. E., Burghammer, M., Friend, R. H., Bulović, V., Walsh, A., Wilson, G. J., Lilliu, S. & Stranks, S. D. Lattice strain causes non-radiative losses in halide perovskites. *Energy Environ. Sci.* **12,** 596–606 (2019).

224. Salim, T., Sun, S., Abe, Y., Krishna, A., Grimsdale, A. C. & Lam, Y. M. Perovskite-based solar cells: impact of morphology and device architecture on device performance. *Journal of Materials Chemistry A* **3,** 8943–8969 (2015).

225. Urbach, F. The Long-Wavelength Edge of Photographic Sensitivity and of the Electronic Absorption of Solids. *Physical Review* **92,** 1324–1324 (1953).

226. Urbach Rule in Solid State Physics. *International Journal of Optics and Applications* **4,** 76–83 (2014).

227. Park, J.-S., Calbo, J., Jung, Y.-K., Whalley, L. D. & Walsh, A. Accumulation of Deep Traps at Grain Boundaries in Halide Perovskites. *ACS Energy Letters* **4,** 1321–1327 (2019).

228. Meggiolaro, D., Mosconi, E. & De Angelis, F. Formation of Surface Defects Dominates Ion Migration in Lead-Halide Perovskites. *ACS Energy Letters* **4,** 779–785 (2019).

229. Conings, B., Drijkoningen, J., Gauquelin, N., Babayigit, A., D'Haen, J., D'Olieslaeger, L., Ethirajan, A., Verbeeck, J., Manca, J., Mosconi, E., Angelis, F. D. & Boyen, H.-G. Intrinsic Thermal Instability of Methylammonium Lead Trihalide Perovskite. *Advanced Energy Materials* **5,** 1500477 (2015).

List of Publications

Main Publications

1. **Qingzhi An**, Paul Fassl, Yvonne Jasmine Hofstetter, David Becker-Koch, Alexandra Bausch, Paul E. Hopkinson and Yana Vaynzof*, High performance planar perovskite solar cells by ZnO electron transport layer engineering, *Nano Energy,* ***39****, 400-408 (2017)*.

2. **Qingzhi An**, Qing Sun, Andreas Weu, David Becker-Koch, Fabian Paulus, Sebastian Arndt, Fabian Stuck, A. Stephen K. Hashmi, Nir Tessler and Yana Vaynzof*, Enhancing the Open-Circuit Voltage of Perovskite Solar Cells by up to 120 mV Using π-Extended Phosphoniumfluorene Electrolytes as Hole Blocking Layers, *Advanced Energy Materials,* ***9****, 1901257 (2019)*.

3. **Qingzhi An**, Fabian Paulus and Yana Vaynzof*, Controlling the Microstructure and Porosity of Perovskite Films by Additive Engineering, *under review*.

4. **Qingzhi An**, Fabian Paulus, David Becker-Koch, Qing Sun, Andreas Weu, Spir Bitton, Nir Tessler and Yana Vaynzof*, Small Grains as Recombination Hot Spots in Perovskite Solar Cells, *under review*.

Cooperated Publications

1. S. Arndt, J. Borstelmann, R. E. Saatlo, P. W. Antoni, F.Rominger, M. Rudolph, **Q. An**, Y. Vaynzof, A. S. K. Hashmi, *Chem. Eur. J.* ***24****, 7882-7889 (2018)*.

2. S. Hahn, J. F. Butscher, **Q. An**, A. Jocic, O. Tverskoy, M. Richter, X. Feng, F. Rominger, Y. Vaynzof, U. H. F. Bunz, *Chem. Eur. J.* ***25****, 7285-7291 (2019)*.

3. J. F. Butscher, S. Intorp, J. Kress, **Q. An**, Y. J. Hofstetter, N. Hippchen, F. Paulus, U. H.F. Bunz, N. Tessler, Y. Vaynzof, *ACS Appl. Mater. Interfaces,* ***12****, 3, 3572-3579 (2020)*.

4. M. L. Falk, K. P. Goetz, V. Lami, **Q. An**, P. Fassl, J. Herkel, F. Thome, A. D. Taylor, F. Paulus, Y. Vaynzof, *Energy Technol,* ***8****, 1900737 (2020)*.

5. R. Ji, Z. Zhang, C. Cho, **Q. An**, F. Paulus, M. Kroll, M. Löffler, F. Nehm, B. Rellinghaus, K. Leo, Y. Vaynzof, *J. Mater. Chem. C,* ***8****, 7725-7733 (2020)*.

6. S. Reichert, J. Flemming, **Q. An**, Y. Vaynzof, J. F. Pietschmann, C. Deibel, *Phys. Rev. Applied,* ***13****, 034018 (2020)*.

7. S. Reichert, **Q. An**, Y. Vaynzof, Y. W. Woo, A. Walsh , C. Deibel, *under review*.

8. A. D. Taylor, Q. Sun,F. Paulus, K. P. Goetz, **Q, An**, T. Schramm, Y. J. Hofstetter, M. Litterst, Y. Vaynzof, *under review*.

9. A. Killigaridis, P. Frantsuzov, A. Yangui, S. Seth, J. Li, **Q. An**, Y. Vaynzof, I. D. Scheblykin, *under review*.

Acknowledgement

First, I would like to thank my supervisor, Prof. Dr. Yana Vaynzof. Thank you for offering me such a great opportunity to further study on solution-based high efficient solar cells within a liberating working group. Thank you for your invaluable supervisions, fruitful advices and financial supports.
Secondly, I would like to thank Prof. Dr. Karl Leo to be my second referee and Prof. Dr. Björn Malte Schäfer, Prof. Dr. Markus Oberthaler to be my examiners. I am grateful to Prof. Dr. Annemarie Pucci, Prof. Dr. Uwe Bunz and Prof. Dr. Marcus Motzkus for providing the access to the AFM, the device fabrication facilities and TCSPC, respectively. Also to Prof. Dr. Jana Zaumseil and Prof. Dr. Rasmus Schröder for the access to the SEM. I thank Dr. Paul Fassl for the SEM measurements and research advices. I thank Dr. Qing Sun and Yvonne Jasmin Hofstetter for the XPS/UPS measurement. I thank Dr. Andreas Weu and David Becker-Koch for the TCSPC and PDS measurements, respectively. I would show my particular thanks to Dr. Fabian Paulus. Thank you for measuring the SEM and XRD, though it always takes you such a long time to show me the results.
Thirdly, I am grateful to Dr. Katelyn P. Goertz, Dr. Alexander D. Taylor, Dr. Fabian Paulus and Elizabeth C. Baird for proof reading my thesis. Many thanks to the postdoc couple for organizing after work events. I would also thank David Becker-Koch to translate the abstract of my thesis into Deutsch. I am glad to share the office with David, Miguel Siguan Albaladejo and Dr. Katelyn P. Goertz in CAM Heidelberg. It is pleasant to work together and have food tour with my colleagues in the group, you are all nice persons. I am glad to work with you both in Heidelberg and Dresden.
I would also thank my friends both in Germany, China and United States,

thank you for sharing me your work experience and life tips. Thank you for accompanying with me when I am under pressure and feel dispirited. No matter where we are, we are always there to support each others.
Last but not least, the way to achieve a PhD is full of physical and mental challenges. I thank myself to overcome all the failure results, always keep positive and finally complete the PhD.
最后，感谢父母的支持与鼓励，让我能够顺利完成博士学习。这些年我不在身边，很多事力所不能及，你们辛苦了，爱你们哟！